博士論文

Effects of Si substitution and uniaxial pressure on the unusual antiferromagnetic order in the Kondo semiconductors CeT_2Al$_{10}$ (T = Ru and Os)

（近藤半導体 CeT_2Al$_{10}$ (T = Ru, Os)の特異な反強磁性秩序に対する Si 置換と一軸圧力の効果）

林　慶介

広島大学大学院先端物質科学研究科

2018年3月

目次

１．主論文

Effects of Si substitution and uniaxial pressure on the unusual antiferromagnetic order in the Kondo semiconductors CeT_2Al_{10} (T = Ru and Os)

（近藤半導体 CeT_2Al_{10} (T = Ru, Os)の特異な反強磁性秩序に対する Si 置換と一軸圧力の効果）

林　慶介

２．公表論文

(1) Anisotropic dependence of the magnetic transition on uniaxial pressure in the Kondo semiconductors CeT_2Al_{10} (T = Ru and Os)
K. Hayashi, K. Umeo, T. Takeuchi, J. Kawabata, Y. Muro, and T. Takabatake, Physical Review B **96**, 245130 /1-6 (2017).

(2) Uniaxial pressure effects on the unusual antifettomagnetic transition in the Kondo semiconductor $CeOs_2Al_{10}$
K. Hayashi, K. Umeo, Y. Yamada, J. Kawabata, Y. Muro, and T. Takabatake,
Journal of Physics: Conference Series **607**, 022002 /1-6 (2017).

(3) Effect of Si substitution on the antiferromagnetic ordering in the Kondo semiconductor $CeRu_2Al_{10}$
K. Hayashi, Y. Muro, T. Fukuhara, J. Kawabata, T. Kuwai, and T. Takabatake,
Journal of the Physical Society of Japan **85**, 034714 /1-4 (2016).

(4) Anisotropic chemical pressure effect on the antiferromagnetic Kondo semiconductor $Ce(Ru_{1-x}Fe_x)_2Al_{10}$
K. Hayashi, Y. Muro, T. Fukuhara, T. Kuwai, J. Kawabara, T. Takabatake, M. Hagihala, and K. Motoya,
Physics Procedia **75**, 121-126 (2015).

主論文

Effects of uniaxial pressure and Si substitution on the unusual antiferromagnetic order in the Kondo semiconductors CeT_2Al$_{10}$ (T = Ru and Os)

（近藤半導体 CeT_2Al$_{10}$ (T = Ru, Os)の特異な反強磁性秩序に対する一軸圧力と Si 置換の効果）

Kyosuke Hayashi

Department of Quantum Matter
Graduate School of Advanced Sciences of Matter
Hiroshima University

March, 2018

Abstract

Most cerium-based compounds have metallic ground states in which the effective mass of quasiparticles is largely enhanced by the hybridization of localized 4*f* electrons with conduction electrons, known as *c*-*f* hybridization. In a few Ce-based compounds, however, the *c*-*f* hybridization gives rise to a narrow gap at the Fermi level E_F, leading to a semiconducting ground state. For example, an orthorhombic compound CeNiSn, a cubic one $Ce_3Bi_4Pt_3$, and a tetragonal one $CeRu_4Sn_6$ possess an energy gap at low temperatures, and thus are called Kondo semiconductors (KSs). The ground state of all KSs is nonmagnetic because the 4*f* moments of Ce ions are killed by the Kondo effects.

The compounds CeT_2Al_{10} (T = Ru and Os) with the orthorhombic $YbFe_2Al_{10}$-type structure show semiconducting transport properties and yet exhibit an antiferromagnetic (AFM) transition. The AFM order has two unusual characteristics. One is the unexpectedly high ordering temperatures T_N, 27 K and 28.5 K for T = Ru and Os, respectively, which are higher by 10 K than T_N of the Gd counterparts. A promising model for the AFM order at high T_N was proposed by a study of polarized optical conductivity for $CeOs_2Al_{10}$. The study has revealed that a kind of charge density wave (CDW) develops along the *b* axis at 36 K far above T_N. The crystal structure can be viewed as constructed from Ce-*T* layers stacking along the *b* axis. Then, it was proposed that opening of the CDW-like gap along the *b* axis induces the AFM order. The other strange fact is that the direction of ordered moments μ_{AFM} along the *c* axis is different from the *a* axis that is the easy magnetization axis preferred by the crystal field effect in the paramagnetic state. To explain this puzzle, it was conjectured that the strong hybridization along the *a* axis prevents the moments from pointing to the *a* axis. Despite extensive studies, the relation among the anisotropic *c*-*f* hybridization, AFM transition at high T_N, and ordered moment direction along the hard axis remains unresolved.

In the present work, we aimed at understanding the relation between the anisotropic *c*-*f* hybridization and unusual AFM order in the Kondo semiconductors CeT_2Al_{10} (T = Ru and Os). First, we have investigated the effect of 3*p* electron doping on the physical properties of $CeRu_2Al_{10}$. On polycrystalline samples of $CeRu_2Al_{10-y}Si_y$ ($y \leq 0.38$), we have measured the

magnetic susceptibility χ, electrical resistivity ρ, and specific heat C. Second, in order to control the *c*-*f* hybridization, we have applied uniaxial pressure on the single crystals of CeT_2Al$_{10}$ (T = Ru and Os). We have measured the strains at room temperature and the magnetization and specific heat at low temperatures.

(1) Compositional analysis of polycrystalline samples of CeRu$_2$Al$_{10-y}$Si$_y$ revealed the solubility limit of Si to be 0.4. The lattice parameters do not change more than 0.2% for $y \leq 0.38$. Therefore, the effects of 3*p* electron doping in CeRu$_2$Al$_{10}$ on the *c*-*f* hybridization was expected to be much stronger than that of the volume change. It is found that the absolute value of paramagnetic Curie temperature θ_P in $\chi(T)$ largely decreases with increasing y, indicating the suppression of *c*-*f* hybridization. The thermal activation behavior in $\rho(T)$ above T_N disappears for $y \geq 0.3$ and T_N decreases to 12 K for $y = 0.38$. These systematic changes in $|\theta_P|$, $\rho(T)$, and T_N coincide with those reported in the 4*d*-electron doped system Ce(Ru$_{1-x}$Rh$_x$)$_2$Al$_{10}$ with respect to the number of doped electrons per formula unit. This coincidence indicates that the Al 3*p*- and Ru 4*d*- electrons in CeRu$_2$Al$_{10}$ play the equivalent role in both the formation of hybridization gap and the unusual AFM ordering.

(2) Application of uniaxial pressure on single crystals of CeT_2Al$_{10}$ (T = Ru and Os) has changed T_N, $\chi(T)$, and spin-flop field B^* in an anisotropic way. Under $P//a$ and $P//c$, the temperatures at the maximum $T_{\chi m}$ shifts to high temperatures. On the contrary, neither $T_{\chi m}$ nor $\chi(T_{\chi m})$ changes under $P//b$, indicating very weak effect of $P//b$ on the *c*-*f* hybridization. As a function of $T_{\chi m}$, the data of T_N under $P//a$ and $P//c$ are smoothly connected. This variation of T_N could be understood by assuming that the *c*-*f* hybridization governs the T_N. Under $P//b$, by contrast, T_N of both compounds significantly increases without any change in $T_{\chi m}$. This observation is at variance with the idea that *c*-*f* hybridization governs T_N in both compounds. Furthermore, we found a linear dependence of T_N on the *b*-axis parameter for both compounds under uniaxial pressure $P//b$ and hydrostatic pressure. This relation indicates that the distance between the Ce-T layers along the *b* axis is the key structural parameter determining T_N.

Contents

Chapter 1

Introduction

1.1 4*f*-electron systems

Fifteen elements ranging from La (Z = 57) to Lu (Z = 71), where Z is the atomic number, are called lanthanides (*Ln*). In addition, the elements including Sc (Z = 21) and Y (Z = 39) are called rare-earth elements. The electron configurations of the trivalent rare-earth ions are $4f^{n}5s^{2}5p^{6}5d^{1}6s^{2}$ (n = 0 –14). As shown in Fig. 1.1, the atomic charge density of 4*f* electrons is localized inside the closed 5*s* and 5*p* shells. The 5*d* and 6*s* electron states become itinerant in intermetallic compounds [1]. The 4*f* electrons yet remain well localized on the rare-earth atom with negligible overlap between 4*f* wave functions centered on neighboring atoms. However, since tails of the wave functions of the 4*f* electrons extend to the outer region of the closed shell, the 4*f* electrons hybridize with conduction electrons (*c*-*f* hybridization).

The 4*f*-electron systems based on Ce and Yb exhibit a large variety of properties such as heavy fermion behavior, valence fluctuations, and hybridization gap, which are originated from competition between the Kondo effect and the Ruderman-Kittel-Kasuya-Yosida (RKKY) interaction [2,3,4,5,6].

1.2 Ce-based compounds

1.2.1 RKKY interaction and Kondo effect

RKKY interaction

The RKKY interaction is an indirect exchange interaction between the localized magnetic moments of 4*f*-electrons which act via the conduction electrons. This interaction is the dominant mechanism for long-range magnetic ordering in Kondo lattice systems [1]. The RKKY interaction of localized spin systems is expressed as,

$$H_{ff} = -\sum_{ij} J(R_{ij})\, \boldsymbol{S}_i \cdot \boldsymbol{S}_j, \tag{1.1}$$

$$J(R_{ij}) \propto \frac{-2k_F R_{ij}\cos(2k_F R_{ij}) + \sin(2k_F R_{ij})}{(2k_F R_{ij})^4}, \tag{1.2}$$

where $J(\boldsymbol{R}_{\mathrm{ij}})$ is the strength of the magnetic exchange interaction between localized spins of $\boldsymbol{S}_{\mathrm{i}}$ and $\boldsymbol{S}_{\mathrm{j}}$, k_{F} is the radius of the conduction electron Fermi surface, and R_{ij} is the nearest-neighbor separation between magnetic ions $\boldsymbol{S}_i$ and $\boldsymbol{S}_j$. As shown in Fig. 1.2, $J(\boldsymbol{R}_{ij})$ attenuates while oscillating from positive to negative in proportion to R_{ij}^3. In rare-earth compounds, the total angular momentum $\boldsymbol{J}$ is the good quantum number than the spin momentum $\boldsymbol{S}$. Then, the Hamiltonian of RKKY interaction is given by,

$$H_{ff} = -\sum_{ij} (g_J - 1)^2 J(\boldsymbol{R}_{ij})\, \boldsymbol{J}_i \cdot \boldsymbol{J}_j, \tag{1.3}$$

where g_J is the Landé *g*-value. If the crystalline electric field (CEF) effect and Kondo effect were neglected, the magnetic transition temperature of a series of rare-earth compounds caused solely by the RKKY interaction can be scaled by the de Gennes factor,

$$dG = (g_J - 1)^2 J(J+1). \tag{1.4}$$

Among isostructural compounds, the Gd compound having the largest $dG = 15.75$ magnetically orders at the highest temperature. Because Ce compounds have $dG = 0.18$, they order magnetically at a temperature much lower than that of the Gd counterpart.

Furthermore, the characteristic temperature of the RKKY interaction, T_{RKKY}, is expressed as follow,

$$k_{\mathrm{B}}T_{\mathrm{RKKY}} \propto |J_{cf}|^2 N_c(E_{\mathrm{F}}), \tag{1.5}$$

where k_{B} is Boltzmann's constant, $N(E_{\mathrm{F}})$ is the density of states of conduction electrons at the Fermi energy E_{F}, and J_{cf} is the exchange coupling strength. J_{cf} is given by,

$$J_{cf} \propto \frac{< |V|^2 >}{E_F - E_{4f}}, \tag{1.6}$$

where V is the *c-f* hybridization matrix element and E_{4f} is the energy of the 4*f* level.

Kondo effect

The electrical resistivity $\rho(T)$ of normal metals such as Cu and Au decreases monotonically on cooling and settles to the residual resistivity when approaching zero temperature. However, when the normal metals contain magnetic impurities such as 3*d* transition metals of Mn and Fe at only 0.1 %, localized spins of the magnetic ions scatter conduction electrons. In this case, the electrical resistivity $\rho(T)$ shows a shallow minimum at low temperatures due to the scattering of conduction electrons by the exchange interaction with localized moments. With decreasing T, $\rho(T)$ increases in proportion to $-\log T$, and settles to the residual resistivity (unitarity limit) [3]. This phenomenon is called the Kondo effect and explained by the calculation of the second-order perturbation of the magnetic scattering due to the *s-d* (*c-f* in the case of magnetic impurities being rare-earth ions) exchange interaction [3,5]. As a result, the localized magnetic moment is screened by the spin polarization of conduction electrons, which couples antiparallel with the moment of the 4*f* electron.

The energy characterizing the Kondo effect is given by the Kondo temperature T_{K} as,

$$k_{\mathrm{B}}T_{\mathrm{K}} \sim W \exp\left(-\frac{1}{J_{cf}D_c(E_{\mathrm{F}})}\right), \tag{1.7}$$

where W is the conduction band width. At T_{K}, $\rho(T)$ reaches to a half of the value of the unitarity limit.

As the concentration of magnetic impurities is increased, interactions between impurity spins become important. Thereby, the local Kondo state gives way to spin glass state and further to magnetically ordered states. However, the Kondo effect survives on certain compounds containing magnetic ions at several dozen percents. This system is called a dense Kondo alloy or a Kondo lattice because magnetic ions are periodically aligned in a lattice. As an example of the dense Kondo effect of 4*f* electrons, $\rho(T)$ of $\mathrm{Ce}_x\mathrm{La}_{1\text{-}x}\mathrm{Cu}_6$ is shown in Fig. 1.4 [7]. The metallic behavior in $\rho(T)$ for $x = 0$ changes to the $-\log T$ dependence at $T > 1$ K for $0.094 \leq x \leq 0.5$. In the range $x \geq 0.5$, the local Kondo state at each 4*f* site becomes coherent at $T < 10$ K. Then, $\rho(T)$ passes through a maximum and decreases with decreasing temperature like in a metal.

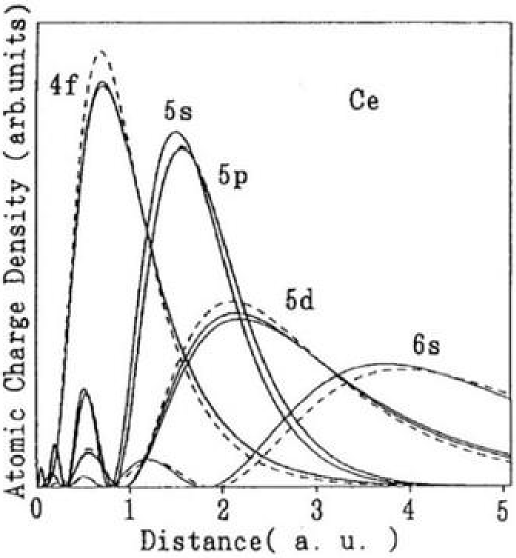

Figure 1.1: The radial components of atomic charge density for Ce [1].

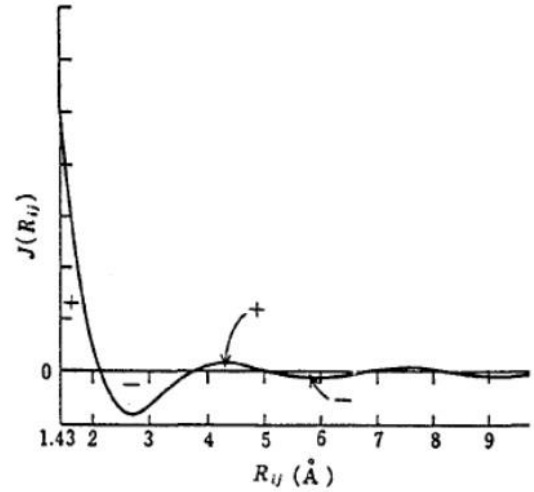

Figure 1.2: The indirect exchange coefficient $\boldsymbol{J}(\boldsymbol{R}_{ij})$ as a function of the distance between neighboring magnetic electrons R_{ij} [1].

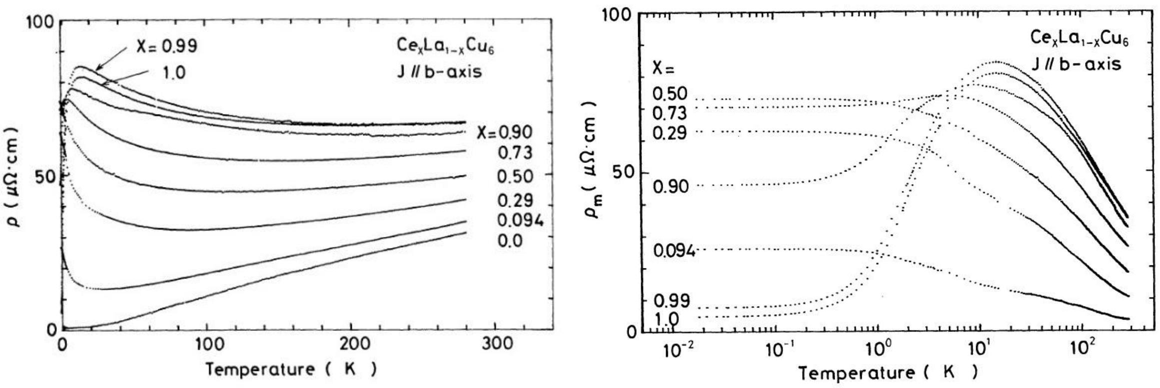

Figure 1.4: Temperature dependence of electrical resistivity for $Ce_xLa_{1-x}Cu_6$ [7].

Doniach phase diagram

Doniach [6] has drawn a magnetic phase diagram for one-dimensional Kondo lattice by comparing the binding energy of the Kondo singlet (Eq. (1.5)) with the characteristic energy of RKKY-type antiferromagnetic interaction (Eq. (1.3)). Both the Kondo effect and the RKKY interaction depend on the value of $|J_{\mathrm{cf}}|N(E_{\mathrm{F}})$. As shown in Fig. 1.3, a simple picture for the competition is the Doniach phase diagram [6]. For a small value of $|J_{\mathrm{cf}}|N(E_{\mathrm{F}})$, the RKKY interaction dominates the Kondo effect and therefore the antiferromagnetic order will occur. For a large value of $|J_{\mathrm{cf}}|N(E_{\mathrm{F}})$, on the contrary, the Kondo term becomes dominant and the antiferromagnetic order is suppressed because the magnetic moments are reduced by the Kondo screening. As a result, the Néel temperature T_{N} passes through a broad maximum and then disappears at a quantum critical point (QCP). On further increasing $|J_{\mathrm{cf}}|N(E_{\mathrm{F}})$, a paramagnetic ground state is stabilized by the strong Kondo effect. The 4*f* electronic state in this region is called an intermediate valance state.

Recently, the Doniach phase diagram has been revised by means of the continuous-time quantum Monte Carlo method combined with the dynamical mean-field theory [8]. The nature of the itinerant-localized transition for heavy electrons has been studied based on the Kondo lattice model, which includs the Heisenberg-type interaction between localized spins.

$$H = \sum_{\boldsymbol{k}\sigma} \xi_k \, c^{\dagger}_{\boldsymbol{k}\sigma} c_{\boldsymbol{k}\sigma} + J_{cf} \sum_{i} \boldsymbol{S}_i \cdot \boldsymbol{s}_{ci} + \frac{J_{\mathrm{H}}}{z} \sum_{(ij)} \boldsymbol{S}_i \cdot \boldsymbol{S}_j \,, \tag{1.8}$$

where $\xi_k = E_k - \mu$ with μ being the chemical potential, $\boldsymbol{S}_i$ is a localized electron spin, $\boldsymbol{s}_{ci}$ is a conduction electron spin, and J_{H} is the Heisenberg interaction between localized spins $\boldsymbol{S}_i$ and $\boldsymbol{S}_j$. The first and second terms represent the Kondo lattice model. The third term is the Heisenberg interaction. Fig. 1.4 (a) shows the temperature dependence of the resistivity $\rho(T)$ for the various values of J_{cf}. The characteristic temperature T_{F}^{*}, where $\rho(T)$ has the peak, corresponds to the effective Fermi temperature below which the heavy Fermi liquid is formed. Fig. 1.4 (b) shows the variations of T_N and T_F^* as a function of J_{cf}. The number of conduction electrons and the J_H are fixed as $n = 0.95$ per site and 0.025, respectively. With increasing J_{cf}, T_F^* decreases and disapears at $J_{cf} = 0.16$, which is located inside the AFM phase. In the range of itinerant side $J_{cf} > 0.16$, T_F^* increases with increasing J_{cf}. T_N increases initialy with increasing J_{cf} to 0.23, but suddenly decreases and goes to zero at $J_{cf} = 0.27$, where the magnetic QCP exists.

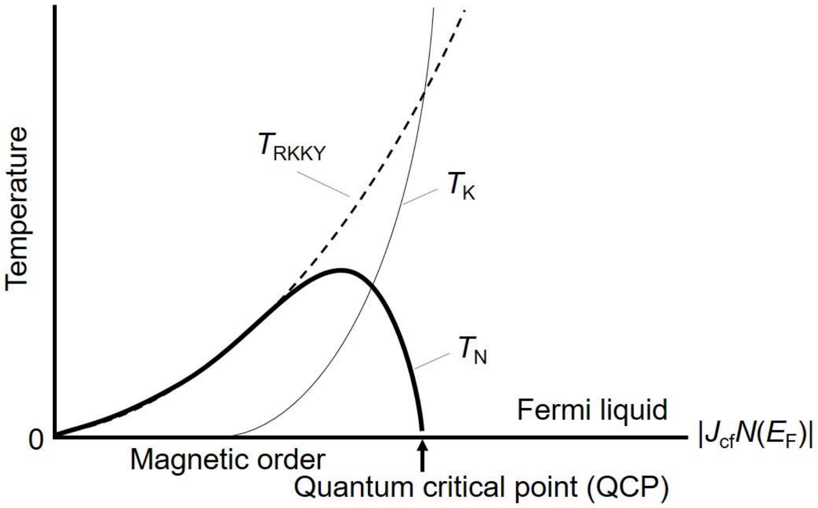

Figure 1.3: The phase diagram by the Doniach model [6]. T_N (solid line) is the antiferromagnetic temperature, T_K and T_{RKKY} (dotted line) are the characteristic temperatures of Kondo effect and RKKY interaction described by Eqs. (1.7) and (1.5), respectively. Non-Fermi liquid behaviors appear in the vicinity of the quantum critical point (QCP). On the right side of QCP, the Fermi liquid state recovers [2,3,4].

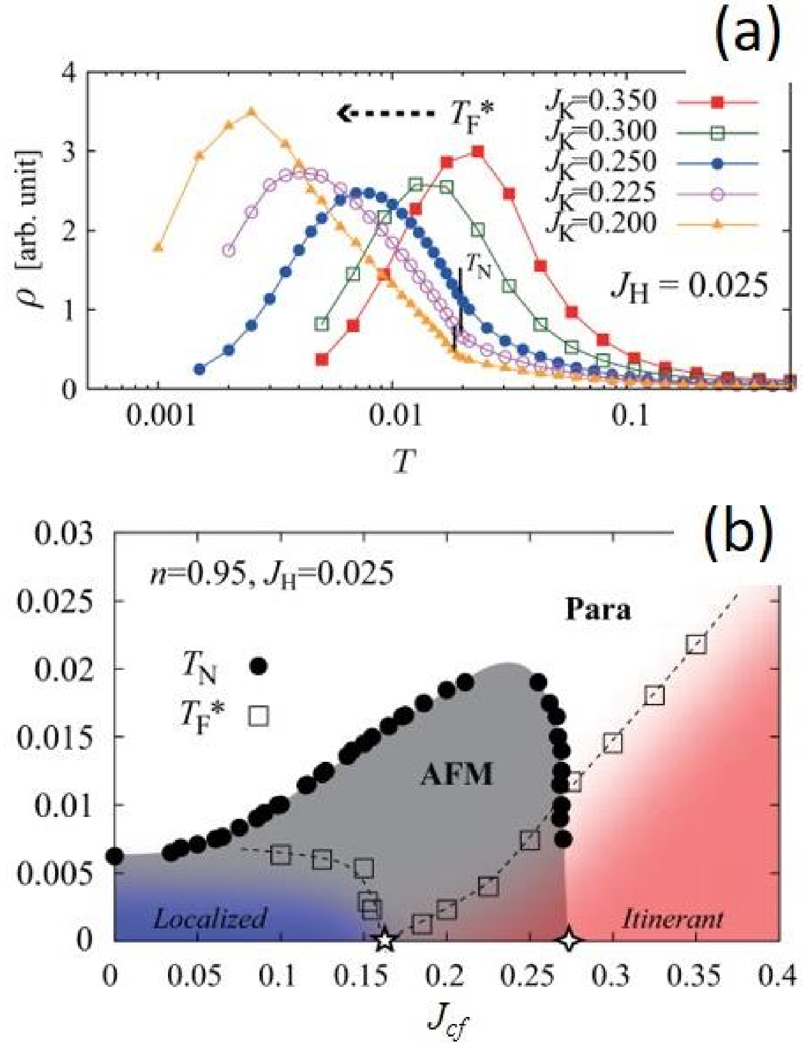

Figure 1.4: (a) Temperature dependence of the electrical resistivity $\rho(T)$ for $0.2 \leq J_{cf} \leq 0.35$ derived from calculation for the Kondo- Heisenberg lattice model [8]. The dotted arrow shows the change of T_F^* with decreasing J_{cf}. (b) Temperature versus J_{cf} phase diagram based on the Kondo-Heisenberg lattice model for the Heisenberg exchange J_H = 0.025 [8]. The number of conduction electrons is fixed as n = 0.95 per site.

1.2.2 Pressure effects on Ce based compounds

Hydrostatic pressure effect on the AFM transition in $CePd_2Al_3$ and CePdAl

The magnitude of *c-f* exchange coupling J_{cf} in Ce-based compounds can be tuned by chemical substitution and external pressure. For example, hexagonal compounds $CePd_2Al_3$ and CePdAl undergo AFM ordering below $T_N = 2.8$ K and 2.7 K, respectively [9,10]. Because the electronic specific heat coefficients γ are 380 and 270 mJ/molK^2, respectively, they are classified into heavy fermion antiferromagnets. Although the T_N's of both compounds are nearly equal at ambient pressure, the pressure dependences are very different [11]. As shown in Fig. 1.5(a), T_N of $CePd_2Al_3$ initially increases, then passes through a maximum near 0.75 GPa and falls rapidly at higher pressures. On the contrary, T_N of CePdAl is pressure insensitive at $P <$ 0.3 GPa and decreases monotonically at the $P >$ 0.3 GPa as shown in Fig.1.5(b). Fig. 1.6 shows the dependence of T_N on J_{cf} for $CePd_2Al_3$ and CePdAl. Here, the magnitude of J_{cf} was calculated using the interatomic distances between Ce and Al atoms based on the Harisson's model [12]. The value of J_{cf} increases with pressure for $CePd_2Al_3$ and CePdAl and all data of T_N can be mapped on a universal curve as a function of J_{cf}, in consistent with the Doniach phase diagram shown in Fig. 1.3 [6].

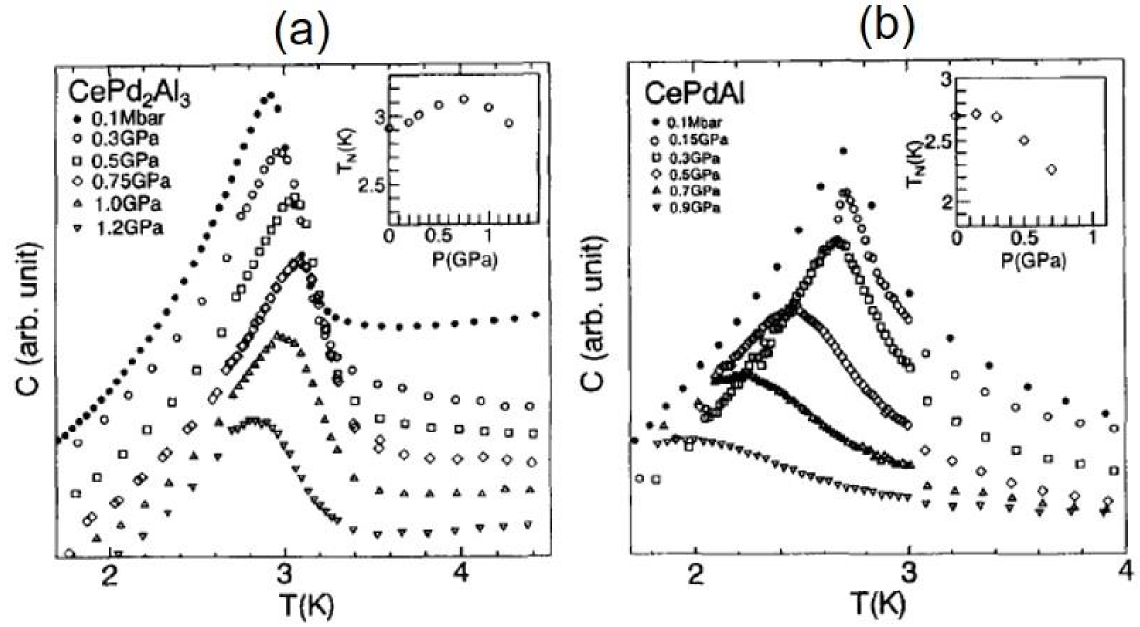

Figure 1.5: Temperature dependences of specific heat *C* of (a) $CePd_2Al_3$ and (b) CePdAl under hydrostatic pressures. The insets show the pressure dependences of T_N, respectively [11].

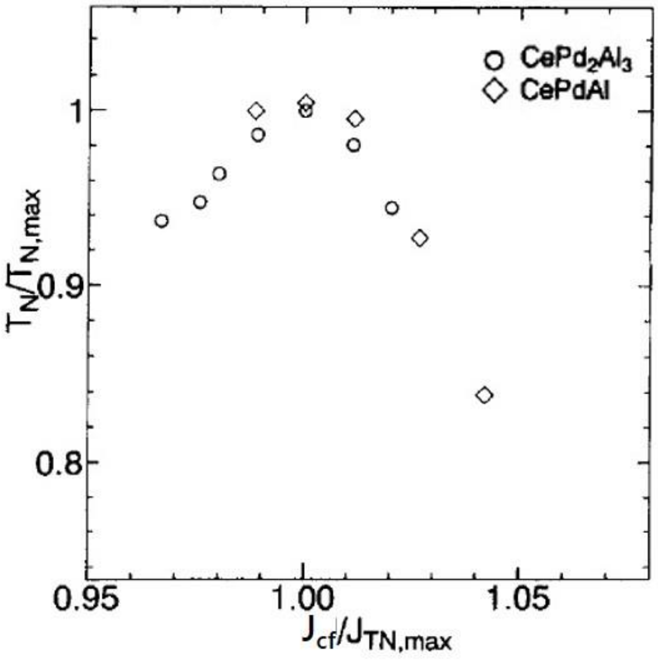

Figure 1.6: Antiferromagnetic transition temperature T_N versus the *c-f* coupling strength J_{cf} for $CePd_2Al_3$ and CePdAl. Both quantities are normalized to their values where T_N exhibits the maximum value [11].

Hydrostatic and uniaxial pressure effects on the superconductivity in Ce*M*In$_5$ (*M* = Rh, Ir, and Co)

The tetragonal Ce-based compounds Ce*M*In$_5$ (*M* = Rh, Ir, and Co) are located around QCP. CeRhIn$_5$ at ambient pressure exhibits a superconducting transition at $T_c = 0.1$ K within an AFM phase [13]. Hydrostatic pressure destroys the magnetism and raises T_c to a maximum of 2.1 K at 1.6 GPa. On the other hand, CeIrIn$_5$ and CeCoIn$_5$ exhibit superconductivity below $T_c = 0.4$ and 2.3 K, respectively [13]. Since the crystal structure can be viewed as alternating layers of CeIn$_3$ and MIn$_2$ stacked along the *c*-axis, it is expected that AFM correlations develop in the cubic (CeIn$_3$) layers in a manner similar to bulk CeIn$_3$. The CeIn$_3$ layers are weakly coupled by an interlayer interaction through the (*M*In$_2$) layer leading to a quasi-2D magnetic structure. For the alloys $\mathrm{Ce}M_{1-x}M'_x\mathrm{In}_5$, a linear relationship was found between T_c and the ratio of the tetragonal lattice constants c/a as shown in Fig. 1.7 [13]. This relation suggests a strong dependence of T_c on dimensionality. Another way to control dimensionality and hybridization is by applying pressure. Under hydrostatic pressure, T_c for CeRhIn$_5$ and CeCoIn$_5$ do not follow the linear dependence on c/a as shown in Fig. 1.7.

Fig. 1.8 shows the temperature dependences of specific heat divided by temperature C/T under applied pressure along the *a* and *c* axes for CeIrIn$_5$ [14]. Uniaxial pressure may lead to fairly small changes in the degree of hybridization, since lattice constants decrease along the direction of applied force but increase in the perpendicular directions. Under $P//a$, T_c is linearly increased, while T_c is linearly decreased under $P//c$, as shown in Fig. 1.9(a). The data in Fig. 1.9(a) are replotted as a function of c/a in Fig. 1.9(b) [14]. Interestingly, the opposite changes in T_c for $P//c$ and $P//a$ can be scaled by the ratio of the lattice parameters c/a. Therefore, the enhancement of T_c under $P//a$ was explained by not the effect of hybridization but the influence of the geometry promoting the two-dimensionality of the crystal structure.

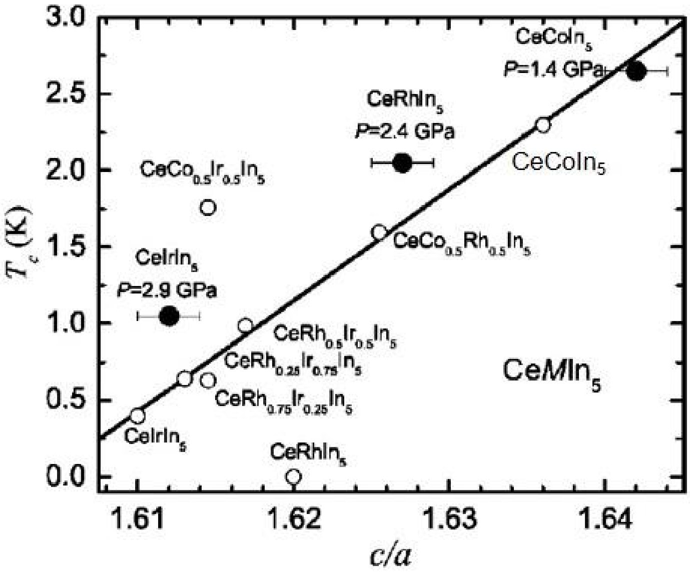

Figure 1.7: Superconducting transition temperatures T_c as a function of c/a for various CeMIn$_5$ (M = Rh, Ir, and Co) at ambient pressure (open circles) [13]. Also shown (solid circles) are T_c under hydrostatic pressure. The line is a least squares fit to the ambient pressure values.

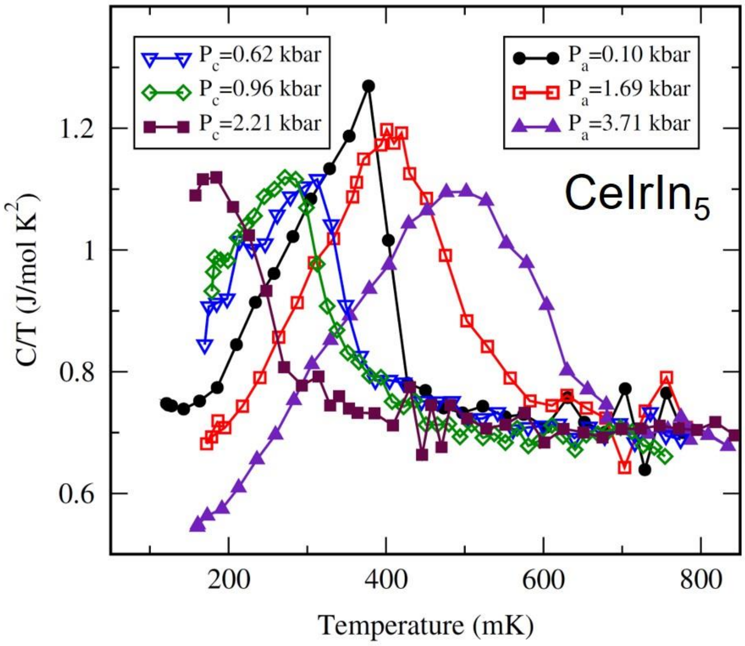

Figure 1.8: Temperature dependences of specific heat divided by temperature C/T under uniaxial pressures for the superconducting transition in CeIrIn$_5$ [14].

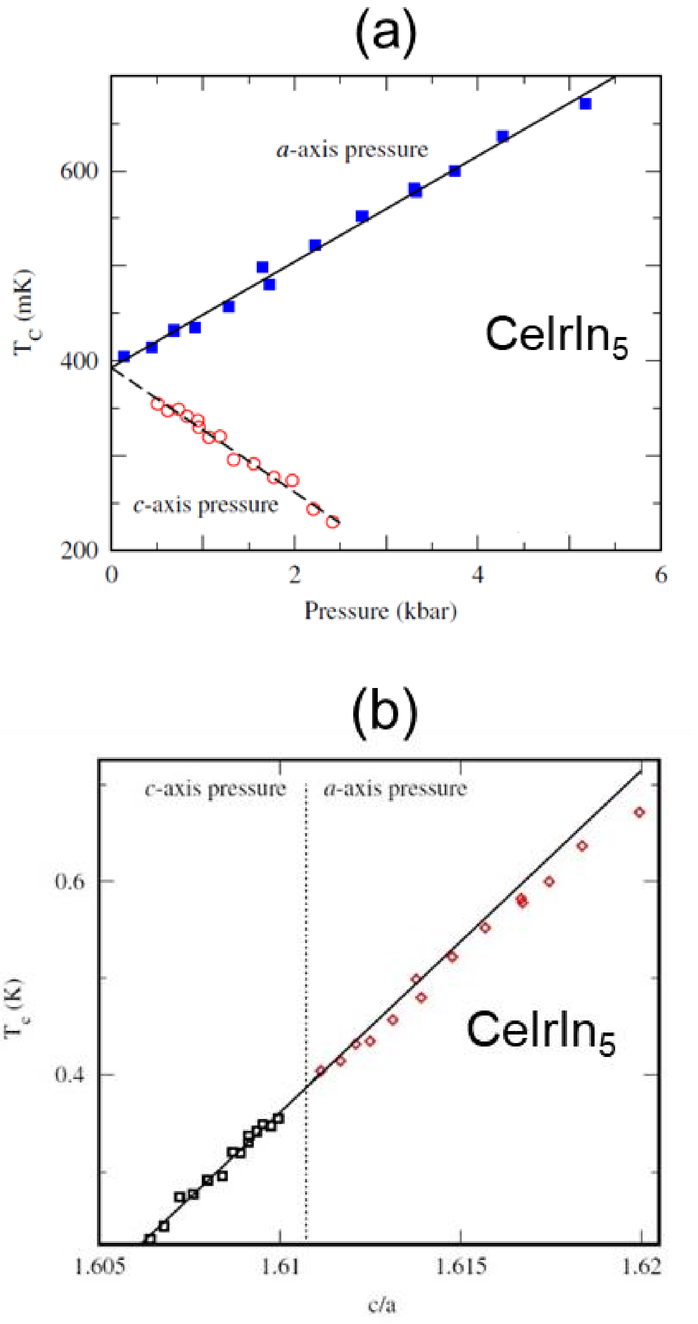

Figure 1.9: (a) Superconducting transition temperature T_c for CeIrIn$_5$ as a function of uniaxial pressure. (b) T_c as a function of the lattice parameter ratio c/a [14].

1.2.3 Kondo semiconductors and pressure effects

Kondo semiconductors

In a few heavy-fermion compounds, the *c*-*f* hybridization gives rise to a narrow gap at the Fermi energy E_F, leading to a semiconducting ground state as shown in Fig. 1.10 [15,16]. For example, an orthorhombic compound CeNiSn [16,17,18,19,20], a cubic one $Ce_3Bi_4Pt_3$ [21,22], and a tetragonal one $CeRu_4Sn_6$ [23, 24,25] possess a narrow gap at low temperatures, and thus called Kondo semiconductors (KSs). The crystal structure, transport gap, and Kondo temperature T_K of KSs are listed in Table 1.2. The cubic systems $Ce_3Bi_4Pt_3$ and YbB_{12} [26,27] have well-defined energy gaps of the order of T_K. On the other hand, an incomplete gap opens in the orthorhombic compounds CeNiSn [16,19,20] and CeRhSb [16,18,28,29]. The ground states in all KSs had been nonmagnetic because the 4*f* moments of Ce ions are fully compensated by the conduction electrons.

Temperature dependences of the electrical resistivity $\rho(T)$ of the KSs are shown in Fig. 1.11 (a) and (b) [36]. Activation-type behaviors are observed in $\rho(T)$ of $Ce_3Bi_4Pt_3$ and YbB_{12}. On the other hand, no semiconducting behavior is observed in that of CeNiSn and CeRhSb. Along the *a*-axis, $\rho(T)$ decreases with decreasing temperature after passing through a maximum or shoulder. The temperature dependence of $\chi(T)$ for KSs is shown in Fig. 1.11(c). All the curves of $\chi(T)$ are characterized by a broad maximum. The maximum temperature $T_{\chi m}$ is a measure of T_K through the relation $T_K \simeq 3T_{\chi m}$ for Ce compounds [37], if the CEF level schemes were similar among the compounds. The decreasing of χ at $T < T_{\chi m}$ is a result of the decrease in the electronic density of states [36]. The upturn in χ for YbB_{12} and $Ce_3Bi_4Pt_3$ at still lower temperature is ascribed to magnetic impurities.

Table 1.2: Crystal structure, transport gap, and Kondo temperature T_K of Kondo semiconductors.

Compound	Crystal structure type	Transport gap (K)	T_K (K)	Ref.
SmB_6	Cubic CaB_6	53 – 80	160	[30,31]
YbB_{12}	Cubic UB_{12}	124 – 136	240	[20,21]
$Ce_3Bi_4Pt_3$	Cubic $Y_3Sb_4Au_3$	84 – 100	240	[22,23]
$Ce_3Sb_4Pt_3$	Cubic $Y_3Sb_4Au_3$	950	1200	[32]
CeNiSn	Orthorhombic ϵ-TiNiSi	14 – 21	39	[16-20]
CeRhSb	Orthorhombic ϵ-TiNiSi	28	360	[16,18,28,29]
CeRhAs	Orthorhombic ϵ-TiNiSi	290	1300	[33,34]
$CeOs_4Sb_{12}$	Cubic $LaFe_4P_{12}$	10	90	[35]
$CeRu_4Sn_6$	Tetragonal YRu_4Sn_6	90-141	290	[24-26]

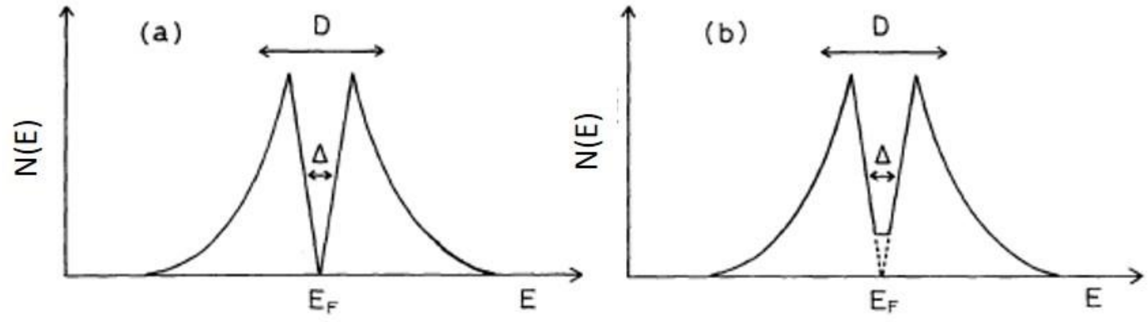

Figure 1.10: (a) V-shaped density of states for the gaped state in Kondo semiconductors for (a) CeRhAs, and (b) CeNiSn and CeRhSb [16].

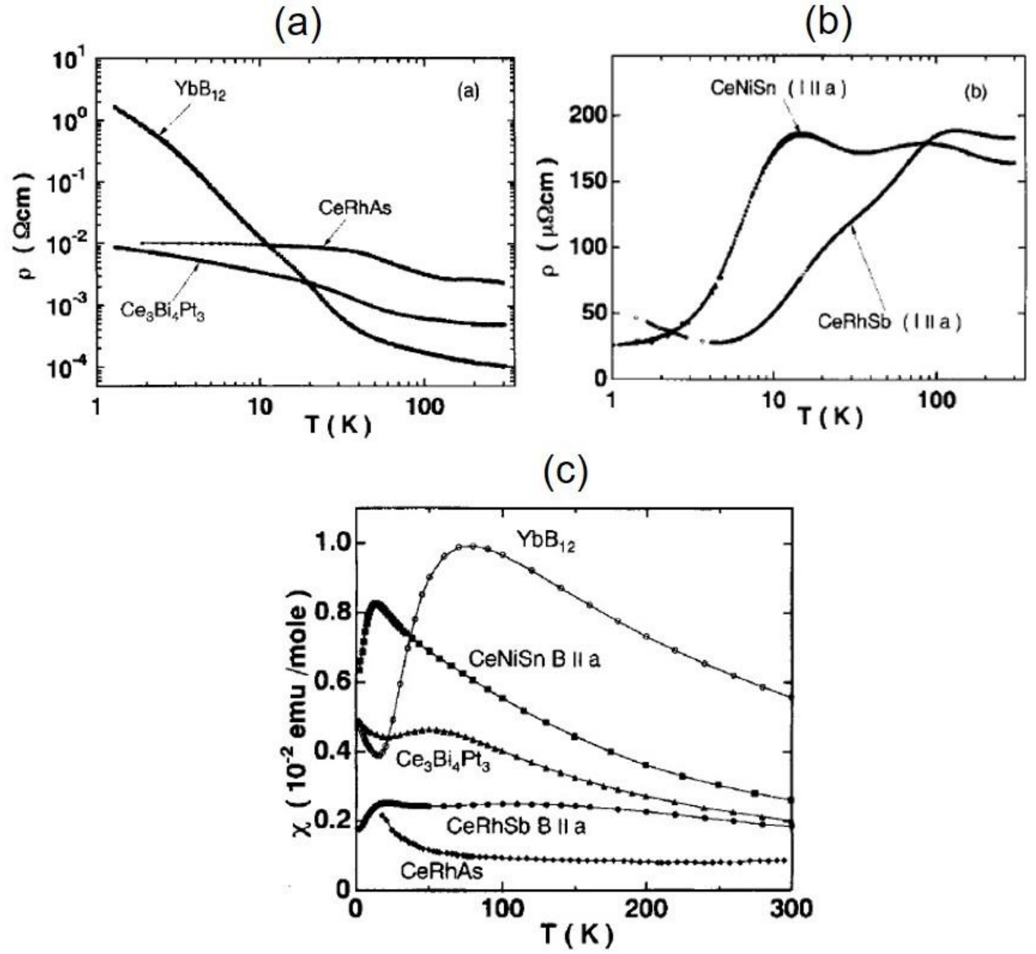

Figure 1.11: Temperature dependence of (a), (b) electrical resistivity $\rho(T)$ and (c) magnetic susceptibility $\chi(T)$ of YbB_{12}, $Ce_3Bi_4Pt_3$, CeNiSn, CeRhSb, and CeRhAs [36].

Pressure effects on Kondo semiconducters

The Kondo semiconductor CeNiSn belongs to the valence fluctuating regime. This compound does not order magnetically at low temperatures because the 4*f* moments are quenched by the strong *c*-*f* hybridization. A systematic study has shown that the gap formation in CeNiSn is very sensitive to the degree of *c*-*f* hybridization [36,38-40].

Because application of hydrostatic pressure strengthens the *c*-*f* hybridization in CeNiSn, the hybridization gap was expected to increase. However, the hybridization gap is suppressed as was indicated from the decreases in the absolute value of the Hall coefficient $|R_H|$ and in the slope of the logρ versus $1/T$ as shown in Fig. 1.12 (a) and (b), respectively [40].

Despite intensive studies, the role *c*-*f* hybridization had not been fully revealed. One of the reasons is that application of hydrostatic pressure strengthens the *c*-*f* hybridization in all directions. Therefore, uniaxial pressure was used to control the ground state of CeNiSn [41]. Fig. 1.12 shows the temperature dependences of the specific heat $C(T)$ and the magnetic susceptibility $\chi(T)$ under various uniaxial pressures. In fact, an AFM order was induced under uniaxial pressures applied along the orthorhombic *b* or *c* axis. Thereby, the lattice is elongated perpendicular to the applied pressure, then *c*-*f* hybridization along the *a* axis is weakened. This promotes localization of the 4*f* electrons, which is in favor of the AFM order.

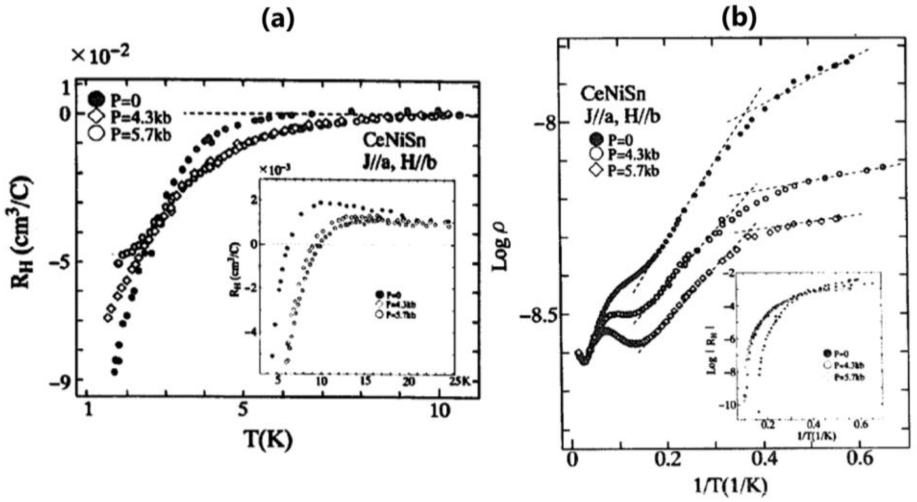

Figure 1.12: (a) Temperature dependence of Hall coefficient R_H for the single crystal of CeNiSn under hydrostatic pressures in the temperature range below 11 K [40]. The inset shows the behavior of R_H near its maximum at 3–25 K. (b) $\log\rho$ as a function of $1/T$ for CeNiSn under hydrostatic pressures. The inset shows $\log|R_\mathrm{H}|$ versus $1/T$.

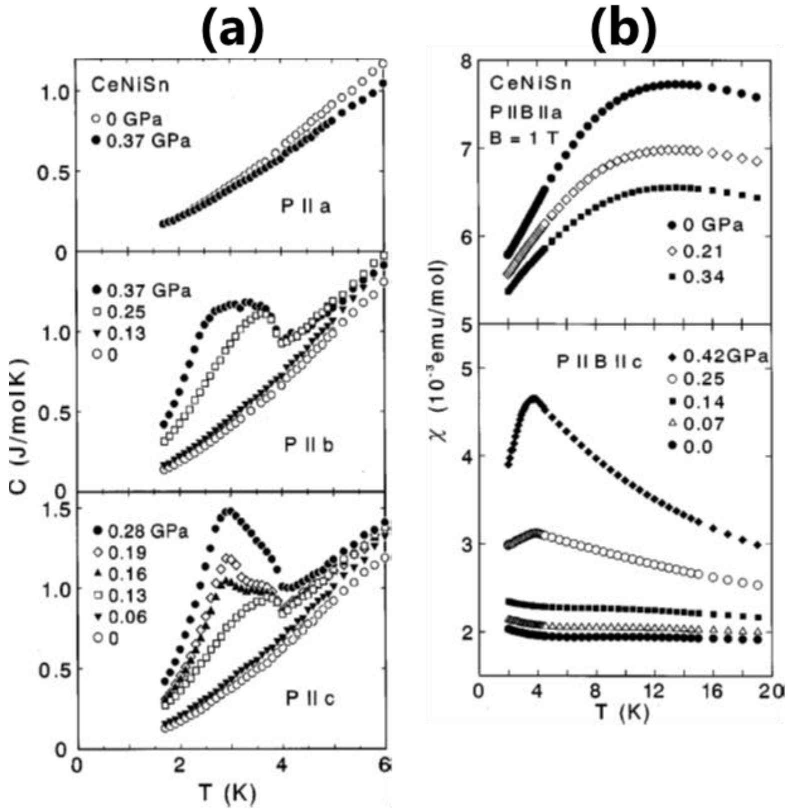

Figure 1.13: (a) Specific heat C of the single crystal CeNiSn as a function of T under uniaxial pressures [41]. (b) Magnetic susceptibility χ of CeNiSn as a function of temperature for different uniaxial pressures $P//B//a$ and $P//B//c$.

1.2.4 Substitution effects on Kondo semiconductors

The ground state of the Kondo semiconductor CeNiSn is very sensitive to carrier doping [36,38,39,42]. Fig. 1.14 (a) shows the temperature dependence of the Hall coefficient R_{H} for single crystals of $\mathrm{Ce}_{1\text{-}y}\mathrm{La}_y\mathrm{NiSn}$ and $\mathrm{CeNi}_{1\text{-}x}T_x\mathrm{Sn}$ (T = Co, Cu, Pt) [42]. For CeNiSn, R_{H} exhibits a maximum at 8.4 K, changes sign from positive to negative at 5.5 K and dramatically decreases with decreasing temperature. The absolute value of R_H at 1.7 K is reduced by substitutions with La for Ce and with Co, Cu, and Pt for Ni. This decrease in R_{H} suggests the suppression of the hybridization gap. With doping of 3*d* holes in CeNiSn by Co substitution for Ni, the maximum value of χ is suppressed as shown in Fig. 1.14 (b), indicating that the doping enhances the *c*-*f* hybridization [42]. On the other hand, doping of 3*d* electrons by Cu substitution for Ni enhances the maximum value of χ which indicates weakened *c*-*f* hybridization. Furthermore, Cu substitution at $x = 0.1$ induces an AFM order as manifested as a kink in the specific heat divided by temperature. (Fig. 1.14 (c)) [38]. The emergence of AFM order was attributed to the weakened *c*-*f* exchange interaction which is a consequence of the increase of Fermi energy with respect to the 4*f* level.

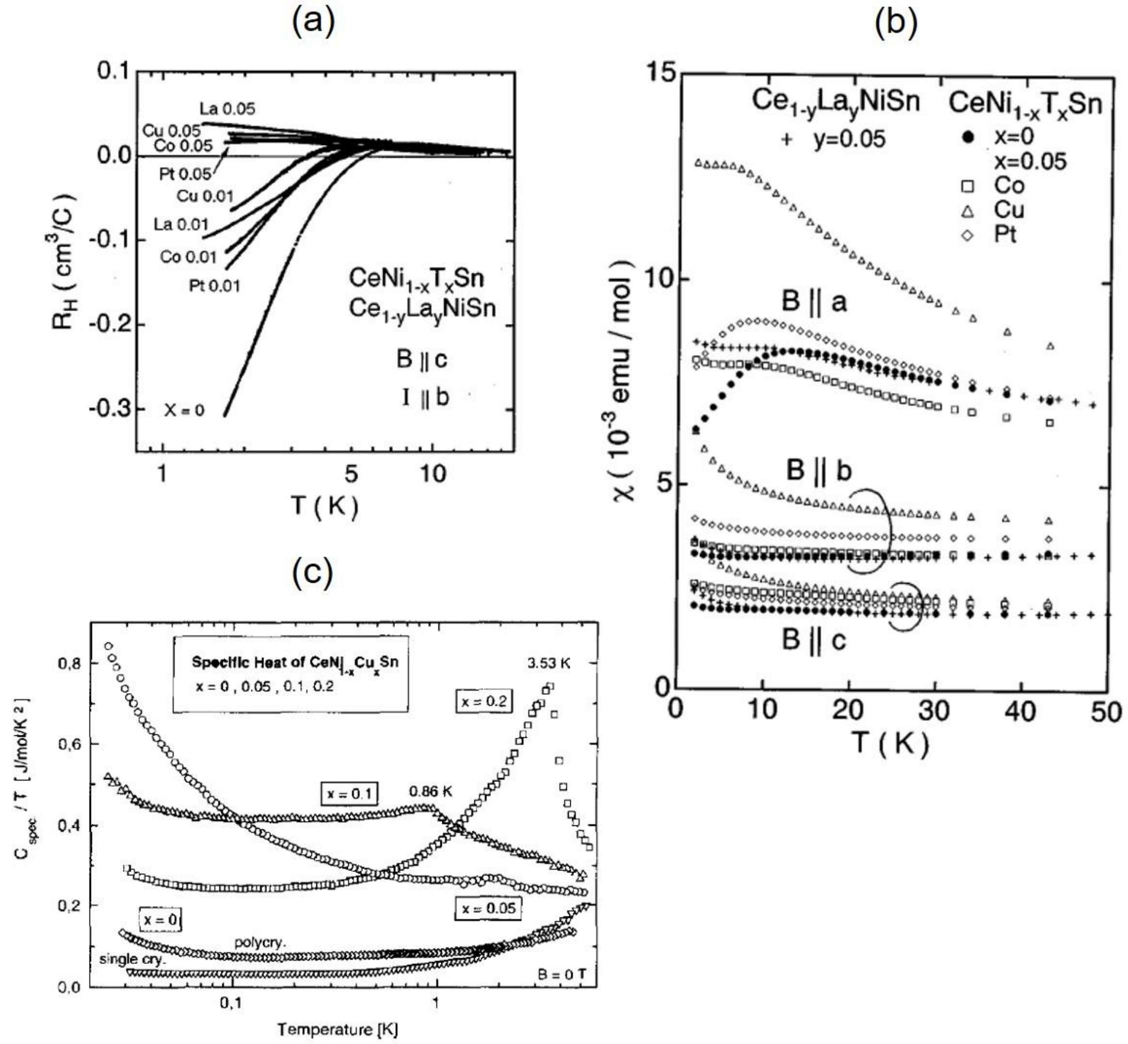

Figure 1.14: (a) Temperature dependence of the Hall coefficient R_H for single crystals of $Ce_{1-y}La_yNiSn$ and $CeNi_{1-x}T_xSn$ (T = Co, Cu, Pt) for x or y = 0, 0.01, and 0.05 [42]. (b) Temperature dependence of the magnetic susceptibility χ for single crystals of $Ce_{1-y}La_yNiSn$ and $CeNi_{1-x}T_xSn$ (T = Co, Cu, Pt) for x or y = 0 and 0.05 [42]. (c) Temperature dependence of specific heat of $CeNi_{1-x}Cu_xSn$ plotted as C/T versus $\log T$ [38].

1.3 Kondo semiconductors CeT_2Al$_{10}$ (T = Fe, Ru, and Os)

1.3.1 Crystal structure

The compounds CeT_2Al$_{10}$ (T = Fe, Ru, and Os) crystallize in the orthorhombic YbFe$_2$Al$_{10}$-type structure with the space group of *Cmcm*, No. 63 as shown in Fig. 1.15 [43-50]. There are two zigzag chains: one consists of the nearest Ce atoms (black solid line) and the other is Ce−*T*–Ce chain (green solid line). The crystal structure can be viewed as constructed from the Ce−*T* zigzag layers stacking along the *b*-axis. Furthermore, the local inversion symmetry at the Ce site with respect to the *b*-axis is absent, which allows the on-site mixing on 4*f*- and 5*d*- states of the Ce ion [51]. The structural parameters for *T* = Ru and Os are listed in Table 1.3, which were determined from the x-ray diffraction experiment at 300 K and the neutron diffraction experiment at 2 K, respectively [45,52]. The atomic distance between the nearest Ce-Ce atoms (~5.2 Å) is larger than those between the Ce and T or Al atoms (3.1~3.5 Å). When going from *T* = Fe to Ru and Os, the value of unit cell volume *V* increases by 3%.

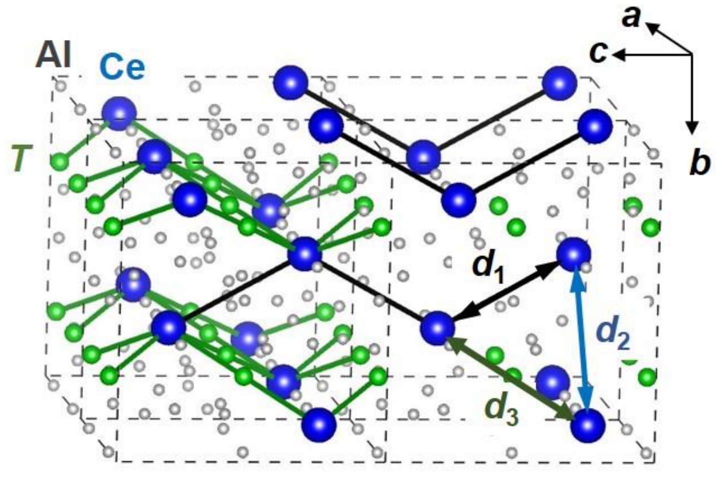

Figure 1.15: YbFe$_2$Al$_{10}$-type crystal structure of CeT_2Al$_{10}$ [43-50]. The first, second, and third nearest neighbor Ce-Ce distances d_1, d_2 and d_3 are drawn by arrows.

Table 1.3: Structural parameters of $CeRu_2Al_{10}$ in the orthorhombic $YbFe_2Al_{10}$-type structure with *Cmcm* space group determined from the x-ray diffraction experiment at 300 K [45].

atom	site	x	y	z
Ce	4c	0	0.12393	0.25
Ru	8d	0.25	0.25	0
Al1	8g	0.2240	0.3634	0.25
Al2	8g	0.3515	0.1304	0.25
Al3	8f	0	0.1599	0.6009
Al4	8f	0	0.3777	0.0500
Al5	8e	0.2261	0	0

Table 1.4: Structural parameters of $CeOs_2Al_{10}$ in the orthorhombic $YbFe_2Al_{10}$-type structure with *Cmcm* space group determined from the neutron diffraction experiment at 2 K [52].

atom	site	x	y	z
Ce	4c	0	0.1257	0.25
Os	8d	0.25	0.25	0
Al1	8g	0.2240	0.36530	0.25
Al2	8g	0.3494	0.1324	0.25
Al3	8f	0	0.1579	0.6020
Al4	8f	0	0.3779	0.0485
Al5	8e	0.2240	0	0

Table 1.5: Lattice parameters and unit cell volume for CeT_2Al_{10} (T = Fe, Ru, and Os) determined by powder x-ray diffraction experiments at 300 K [53,48,50].

T	a (Å)	b (Å)	c (Å)	V (Å^3)
Fe	9.004	10.229	9.075	835.8
Ru	9.1246	10.2806	9.1878	861.9
Os	9.1386	10.2662	9.1852	861.7

1.3.2 Magnetic, transport, and thermal properties of CeT_2Al$_{10}$ (T = Fe, Ru, and Os)

These compounds CeT_2Al$_{10}$ display semiconducting transport properties. Nevertheless, the compounds with T = Ru and Os exhibit an antiferromagnetic (AFM) transition at unexpectedly high temperatures T_N = 27 K and 28.5 K, respectively, although the Ce moments are reduced to 0.3-0.4 μ_B/Ce by the Kondo effect [43,46,48-50,52-54].

Fig. 1.16 (a)–(c) display temperature dependences of the resistivity $\rho(T)$ for CeT_2Al$_{10}$ (T = Fe, Ru, and Os) [52,48,49]. The −log$T$ dependence from 300 to 100 K is followed by a thermal activation-type behavior in the range from 80 to 30 K, as shown in the inset. By fitting the data with the formula $\rho = \rho_0\exp(\Delta/2k_BT)$, the values of Δ_a/k_B, Δ_b/k_B, and Δ_c/k_B are estimated to be 42, 50, and 58 K for T = Ru and 56, 83, and 65 K for T = Os, respectively [48,49,54]. In Fig. 1.16 (b) and (c), the activation behavior appears in two temperature ranges 60 K–T_N and 15–8 K for T = Os and 210–140 K and 21–11 K for T = Fe [52]. The AFM transition temperature T_N was taken as the midpoint of the jump in the specific heat divided by temperature C/T, as shown in Fig. 1.17 (a) [47,49,50]. Below T_N, the $\rho(T)$ data for T = Ru and Os increase abruptly, which may be attributed to formation of a superzone gap on the Fermi surface [56]. Such a superzone gap is formed by folding of the Brillouin zone associated with the AFM order.

Fig. 1.16 (d)-(f) display the temperature dependences of the thermopower $S(T)$. At T_N for T = Ru and Os, S_b decreases but S_a and S_c jump in coincidence with those in $\rho(T)$. At a glance, the anisotropic behavior in $S(T)$ is stronger than in $\rho(T)$ especially for T = Os. Upon crossing the T_N, S_b(T) drops dramatically from 30 to −7 μV/K [57].

The temperature variations of magnetic susceptibility $\chi(T)$ are shown in Fig. 1.16 (d)–(f) [52,48,49]. The data of $\chi(T)$ for the three compounds exhibit anisotropy, $\chi(B//a) > \chi(B//c) > \chi(B//b)$. By keeping this anisotropy, the absolute values of χ along the three directions decrease on going from T = Os to T = Ru and then to T = Fe. Concomitantly, the temperature at the maximum in $\chi(B//a)$, $T_{\chi\mathrm{m}}$, increases from 30 K for T = Ru to 45 K for T = Os and to 70 K for T = Fe. If the Kondo temperature T_K is estimated as $3T_{\chi\mathrm{m}}$, then T_K increases from 90 K for T = Ru, 135 K for T = Os, to 210 K for T = Fe. This increasing order in T_K is consistent with that in the effective *c-f* hybridization strength, $V_\mathrm{eff}(T = \mathrm{Ru}) < V_\mathrm{eff}(T = \mathrm{Os}) < V_\mathrm{eff}(T = \mathrm{Fe})$. This relation was derived from the hard x-ray photoemission spectroscopy experiments [58]. Furthermore, the broad peak in $\chi_a(T)$ and $\chi_c(T)$ for $\mathrm{CeFe_2Al_{10}}$ is a characteristic of a valence-fluctuation system [53]. In fact, the valence-fluctuating state in $\mathrm{CeFe_2Al_{10}}$ was confirmed by the x-ray absorption measurements [59]. The decrease in $\chi(T)$ below T_N along the three principal directions for T = Ru and Os was considered to be unusual for antiferromagnets with localized moments. However, the behaviors were reproduced by the calculation of $\chi(T)$ on the Kondo lattice model by using the dynamical mean field theory and the continuous-time quantum Monte Carlo method [60]. Furthermore, the anisotropic susceptibilities of $\mathrm{Ce}T_2\mathrm{Al_{10}}$ with T = Ru, Os, and Fe in the whole temperature range were reproduced by incorporating the effects of the crystalline electric field (CEF) in the anisotropic Kondo lattice as shown in Fig. 1.18 (a)-(c), respectively [61].

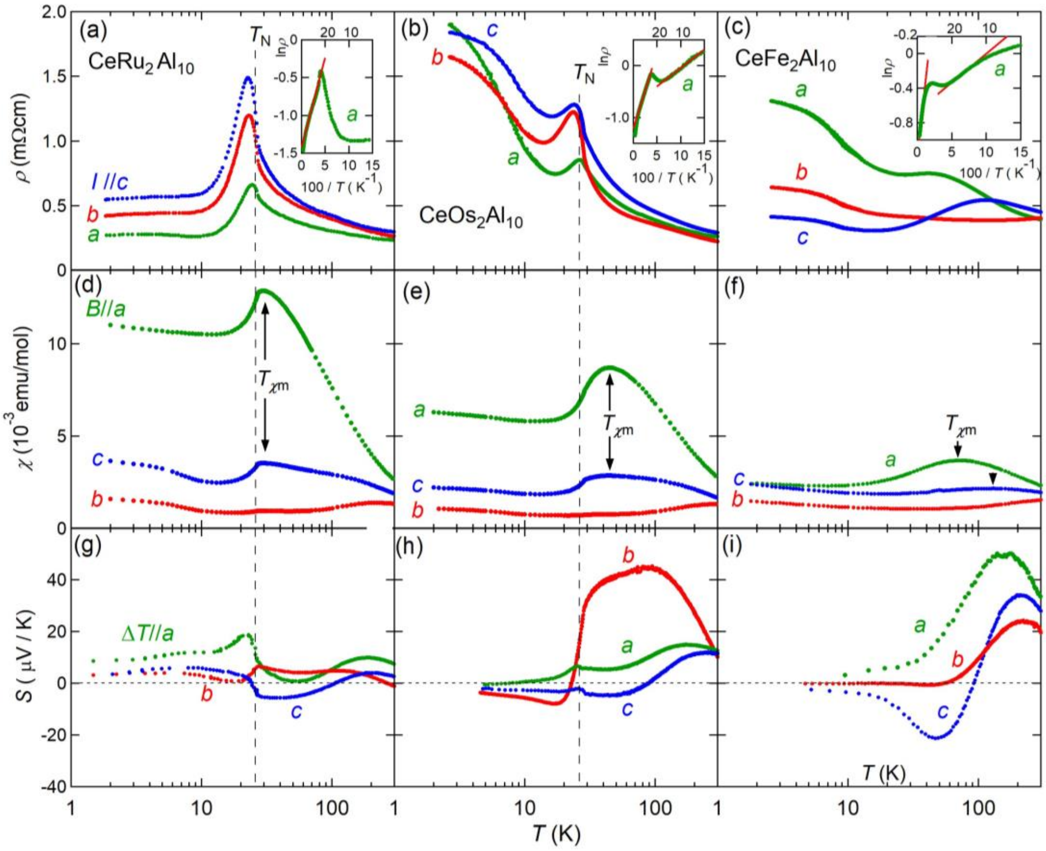

Figure 1.16: Temperature variations of the resistivity $\rho(T)$, magnetic susceptibility $\chi(T)$, and thermopower $S(T)$ along the three principal axes for single crystals of CeT_2Al$_{10}$ (T = Fe, Ru, and Os) [49,50,53,57]. The dotted lines indicate the AFM transition temperature T_N. The insets show the Arrhenius plot of $\rho(T)$

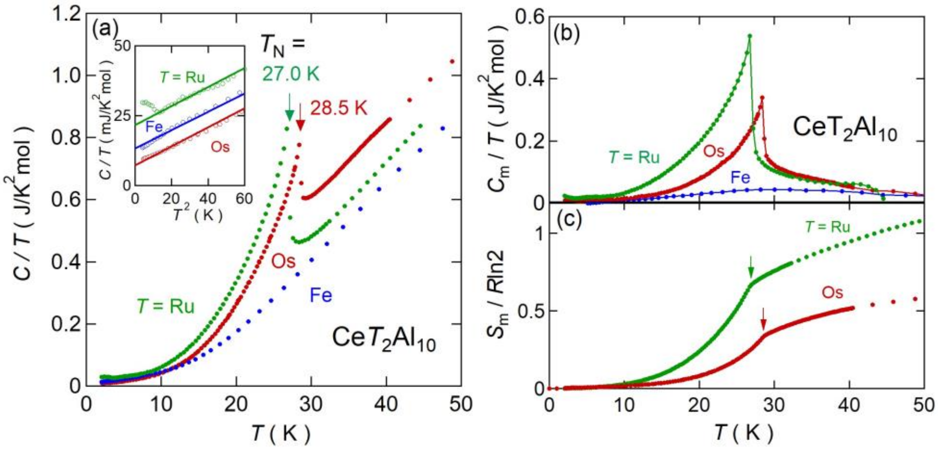

Figure 1.17: Temperature dependences of (a) the specific heat divided by temperature C/T, (b) magnetic part C_m/T, and (c) magnetic entropy S_m divided by Rlog2 for CeT_2Al$_{10}$ (T = Fe, Ru, and Os) [47,49,50]. The arrows indicate T_N defined as the midpoint of the jump in C/T. The inset of (a) shows C/T vs T^2.

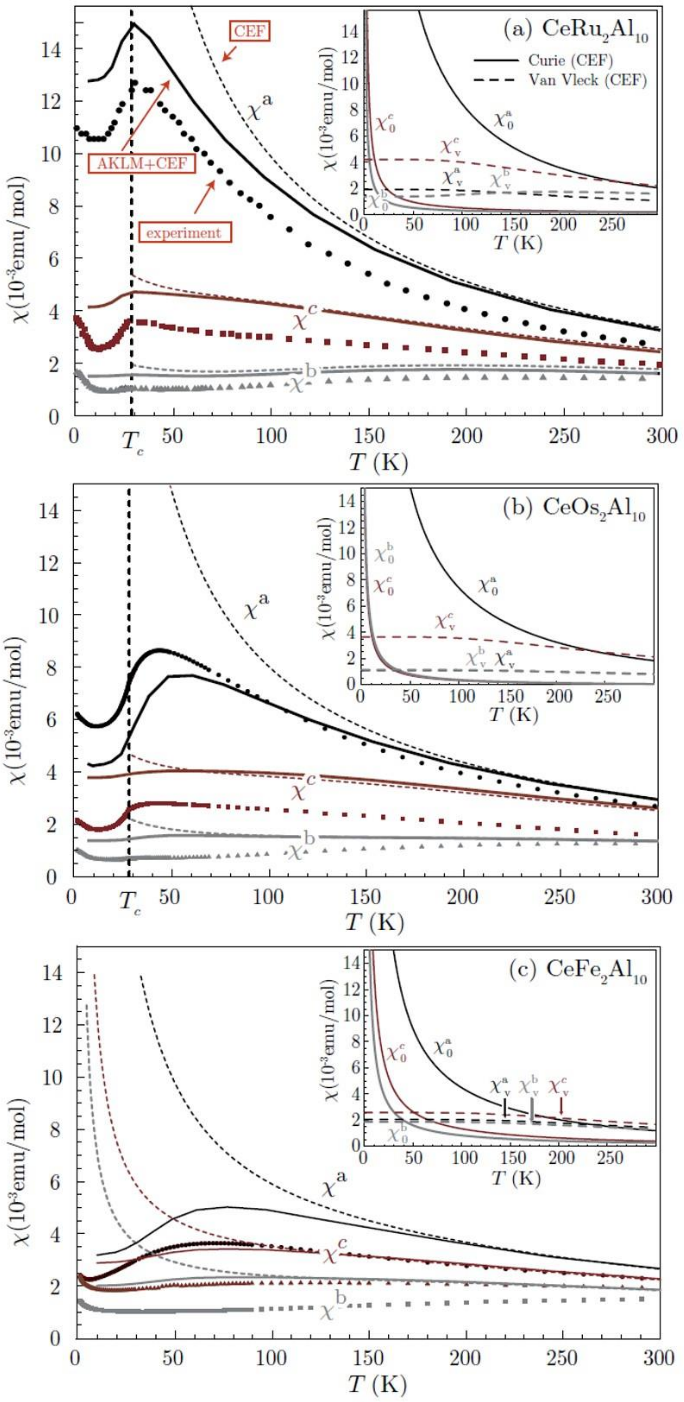

Figure 1.18: Temperature dependence of magnetic susceptibilities calculated for CeT_2Al$_{10}$ for (a) T = Ru, (b) T = Os, and (c) T = Fe [61]. The solid curves are calculated by the anisotropic Kondo lattice model combined with the CEF wave functions. The experimental data of magnetic susceptibility are shown by the symbols. The dashed lines represent the magnetic susceptibilities of the CEF model. The solid and dashed lines in the insets indicate the Curie terms χ_0 and the Van Vleck terms χ_V of the CEF model, respectively.

Fig. 1.19 shows the antiferromagnetic structure of CeT_2Al$_{10}$ (T = Ru and Os) determined by neutron diffraction experiments [52,54,62]. As shown in Fig. 1.20, the magnetic Bragg peak of (0 1 0) develops with decreasing temperature below 27 K and 28.5 K for T = Ru and Os, respectively [62]. The observed intensities of magnetic Bragg peak agreed with intensities calculated by assuming the magnetic structure shown in the Fig. 1.19, where the ordered Ce moments μ_{AFM} are oriented along the *c* axis. Interestingly, this direction is different from the *a* axis of the easy magnetization axis in the paramagnetic state [49,50,53]. To explain this puzzle, it was conjectured that the strong hybridization along the *a* axis prevents the moments from pointing to the *a* axis [45]. The magnitude of the ordered moments was estimated as $0.43\mu_{\mathrm{B}}$ for T = Ru and as $0.29\mu_{\mathrm{B}}$ for T = Os. Recently, resonant polarised soft x-ray scattering at the Ce *M*-edge has been used to refine the magnetic structure of CeRu$_2$Al$_{10}$ [63]. The polarization dependence of the x-ray magnetic scattering suggests that the magnetic structure is non-collinear in nature, and the $\mu_{\mathrm{AFM}}//c$ is canted towards the *a*-axis by 9.6°±1.1. Furthermore, μSR experiments of CeT_2Al$_{10}$ (T = Ru and Os) clearly revealed coherent frequency oscillations blow T_{N}, indicating the presence of an internal field at the muon site as shown in Fig. 1.21 (a) and (b) [46,52,54]. These observations confirmed the long-range magnetic order of the Ce moments below T_{N} in CeT_2Al$_{10}$ (T = Ru and Os).

Let us briefly summarize the results of structural and magnetic studies of the series of compounds LnT_2Al$_{10}$ (*Ln*: lanthanides, T = Fe, Ru, and Os). The orthorhombic lattice parameters decrease on going from *Ln* = La to *Ln* = Lu according to the lanthanide contraction as shown in Fig. 1.22 [45,64]. Compared with the expected lattice parameters from the interpolation between *Ln* = La and *Ln* = Pr, the *a*- and *c*-axis parameters for *Ln* = Ce are smaller by 0.2% whereas the *b*- axis parameter is smaller only by 0.07%. This anisotropic contraction suggests that the *c*-*f* hybridization in the *a*-*c* plane is stronger than along the *b* direction. However, this suggestion has not been confirmed yet by microscopic measurements yet.

Fig. 1.23 shows the magnetic transition temperatures of the series of (a) $Ln\mathrm{Ru_2Al_{10}}$ and (b) $Ln\mathrm{Os_2Al_{10}}$ versus the de Gennes factor $dG = (g_J - 1)^2J(J + 1)$, where J is the total angular momentum of Ln^{3+} ion [64,65,66]. For Ln = Ce, the T_N's are largely deviated from the dG scaling by factors of 150. Namely, both $\mathrm{Ce}T_2\mathrm{Al_{10}}$ (T = Ru and Os) with Ce moments of 0.29-0.43 μ_B have T_N's higher than those of the Gd counterparts with 7 μ_B/Gd. This fact indicates that the high T_N for $\mathrm{Ce}T_2\mathrm{Al_{10}}$ cannot be explained by the simple RKKY interaction between the localized magnetic moments of $\mathrm{Ce^{3+}}$ ions. We need to take into account of the effects of *c-f* hybridization and CEF on the magnetic order.

The polarized optical conductivity spectra σ (ω) with the electric field along the orthorhombic principal axes of $\mathrm{Ce}T_2\mathrm{Al_{10}}$ are shown in Fig. 1.24 [67,68]. Shoulder structures gradually evolve on cooling at around 55, 45, and 40 meV for T = Fe, Os, and Ru, respectively, which were attributed to *c-f* hybridization gap. However, along the *b*-axis, the $\sigma(\omega)$ spectra for T = Ru and Os have a shoulder or peak at 20 meV, which develops on cooling below 40 K. It was understood as a charge excitation gap caused by band nesting due to charge density wave (CDW) formation. The 20-meV peak intensities are shown as the cross-hatched areas in Fig. 1.25 (a). To evaluate the total intensity, the effective electron number N_eff was calculated by integrating the excess conduction $\Delta\sigma(\hbar\omega)$,

$$N_{eff} = \frac{4m_0}{h^2e^2}\int_0^\infty \Delta\sigma\,(\hbar\omega)d\hbar\omega, \tag{1.9}$$

where h is the Planck constant, e the elementary charge, m_0 the electron rest mass, and $\hbar\omega$ the photon energy. The obtained N_effs for T = Ru and Os are shown as a function of temperature in Fig. 1.25 [68]. The results of $N_\mathrm{eff}(T)$ indicate that the charge excitation gap for T = Ru and Os develops at 32 K and 38 K, respectively, which temperatures are higher than T_N. The crystal structure presented in Fig. 1.15 can be viewed as constructed from Ce-T layers stacking along the *b* axis. Then, it was proposed that opening of the CDW-like gap along the *b* axis induces the AFM order [67,68].

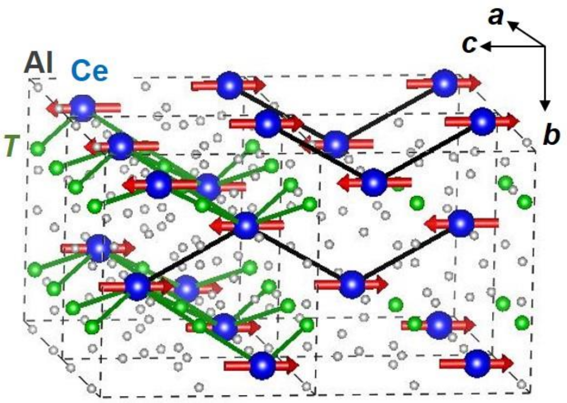

Figure 1.19: Antiferromagnetic structure of CeT_2Al$_{10}$ (T = Ru, and Os). The black and green solid lines represent the nearest Ce-Ce and Ce-T-Ce zigzag chains, respectively [52,54,62].

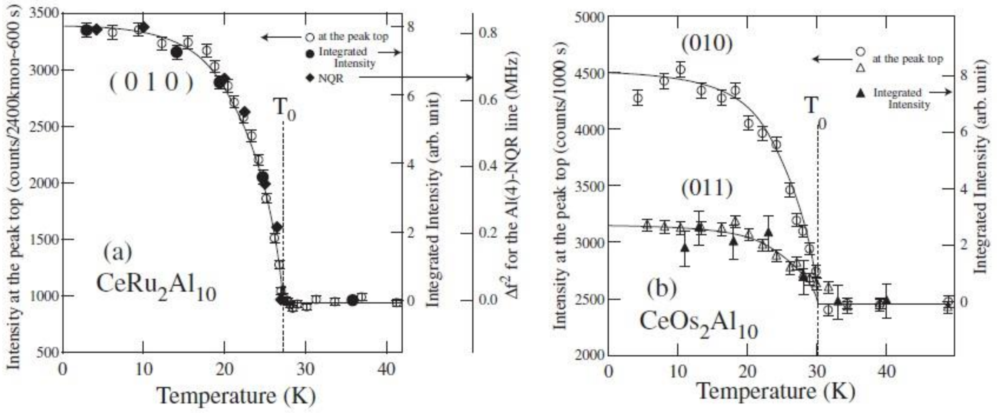

Figure 1.20: Temperature dependences of magnetic peak intensities of (a) CeRu$_2$Al$_{10}$ and (b) CeOs$_2$Al$_{10}$. The open symbols display the heights of the peak top and closed symbols are the integrated intensities [62].

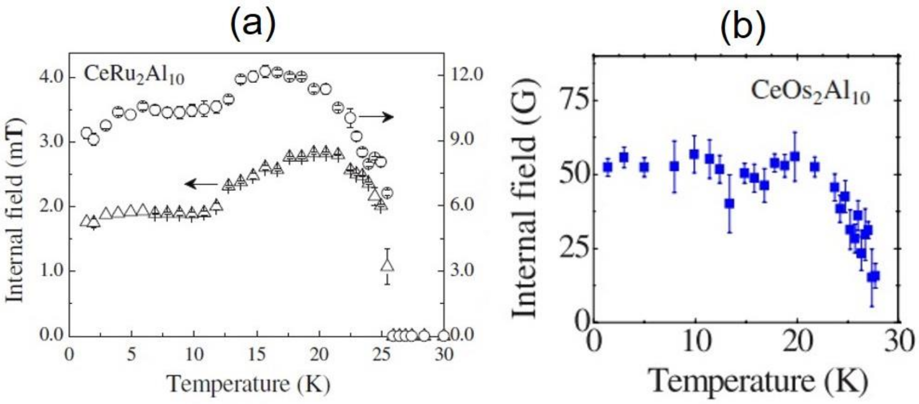

Figure 1.21: Internal field at the muon sites vs temperature for (a) CeRu$_2$Al$_{10}$ and (b) CeOs$_2$Al$_{10}$ [46,52,54].

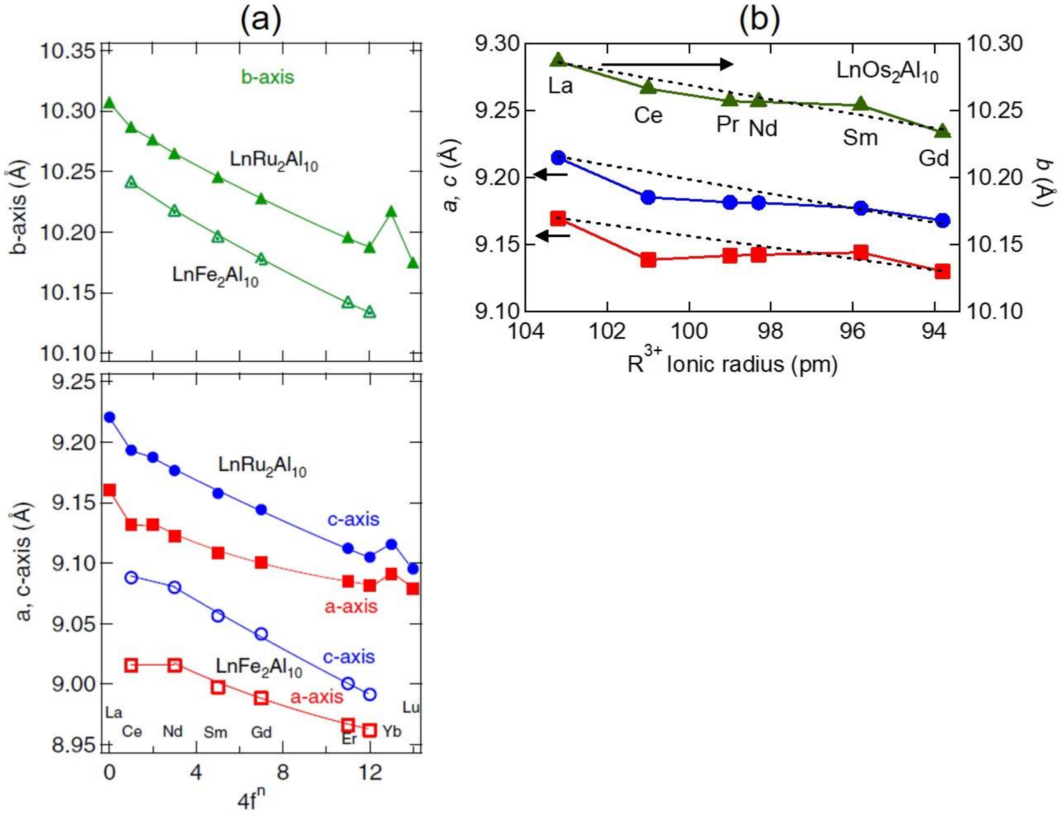

Figure 1.22: (a) Lattice parameters along the three principal axes of the series of compounds LnT_2Al_{10} (T = Ru and Fe) at 300 K. (b) Lattice parameters along the three principal axes of $LnOs_2Al_{10}$ at 300 K as a function of the ionic radius of Ln^{3+} [45,64].

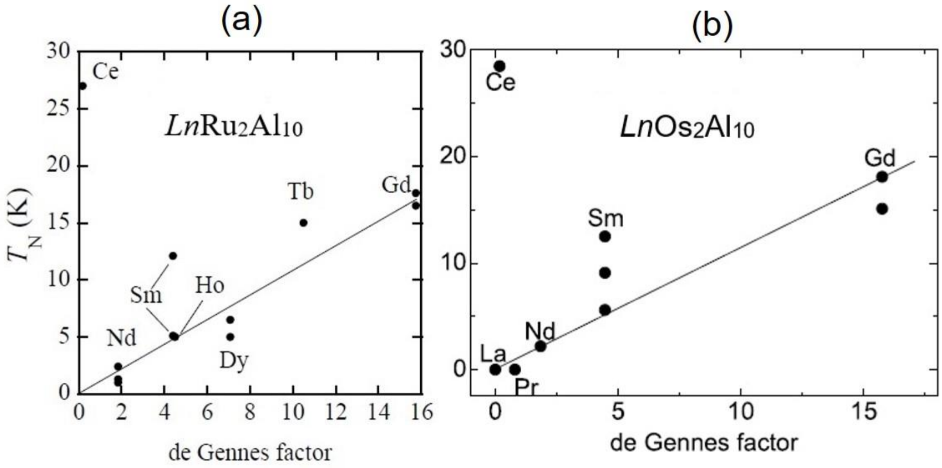

Figure 1.23. Magnetic transition temperatures of (a) $LnRu_2Al_{10}$ (Ln = Ce, Nd, Sm, Ho, Dy, Tb, and Gd) and (b) $LnOs_2Al_{10}$ (Ln = La, Ce, Pr, Nd, Sm, and Gd) against the de Gennnes factor $dG = (g_J - 1)^2 J(J+1)$ [64,66].

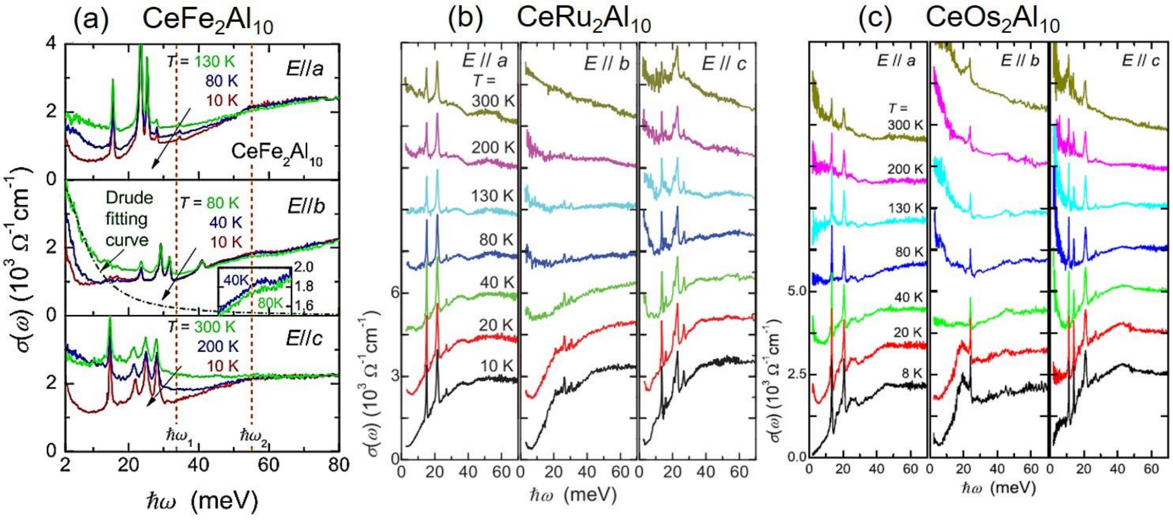

Figure 1.24: Temperature dependences of optical conductivities $\sigma(\omega)$ of CeT_2Al$_{10}$ for (a) T = Fe, (b)T = Ru, and (c) T = Os [67,68].

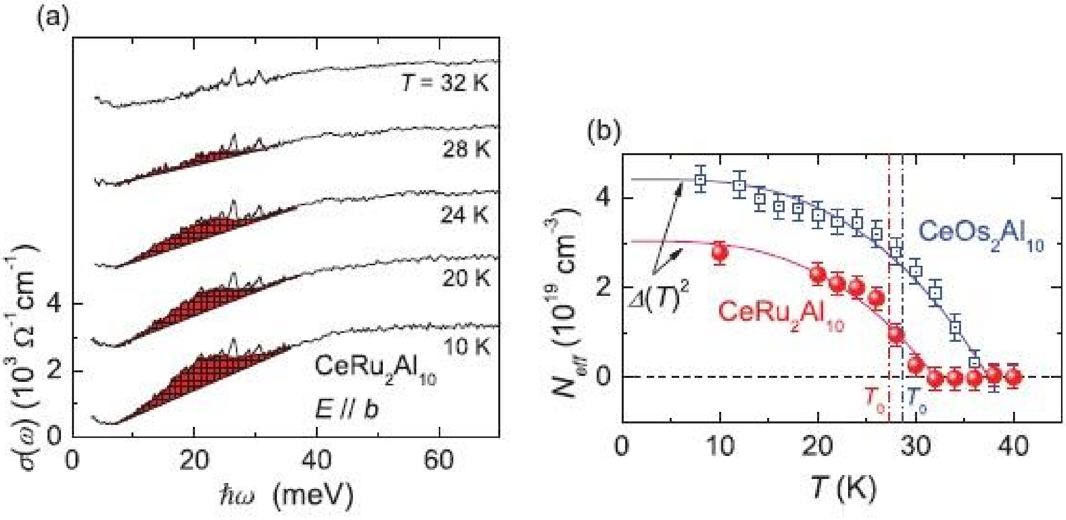

Figure 1.25: (a) Optical conductivity spectrum $\sigma(\omega)$ for CeRu$_2$Al$_{10}$ in $E//b$ at different temperatures [68]. The cross-hatched areas at around 20 meV are shoulder structures caused by band nesting due to CDW formation. (b) Effective electron number N_{eff} of the shoulders shown in (a) for CeRu$_2$Al$_{10}$ and CeOs$_2$Al$_{10}$ plotted as a function of temperature.

Fig.1.26 (a)-(c) and (d) show the isothermal magnetization for $CeRu_2Al_{10}$ and $CeOs_2Al_{10}$ for $B//a$, $B//b$, and $B//c$, respectively [50,69]. The magnetic field applied along the c axis induces a spin flop transition from $\mu_{AFM}//c$ to $\mu_{AFM}//b$ at $B^* = 4$ T and 7 T for $T =$ Ru and Os, respectively. This reorientation of μ_{AFM} was confirmed by the ^{27}Al NMR experiment of $CeRu_2Al_{10}$ [70]. The reorientation to not the easy a axis but to the hard b axis was attributed to the strong c-f hybridization along the a axis [45,70].

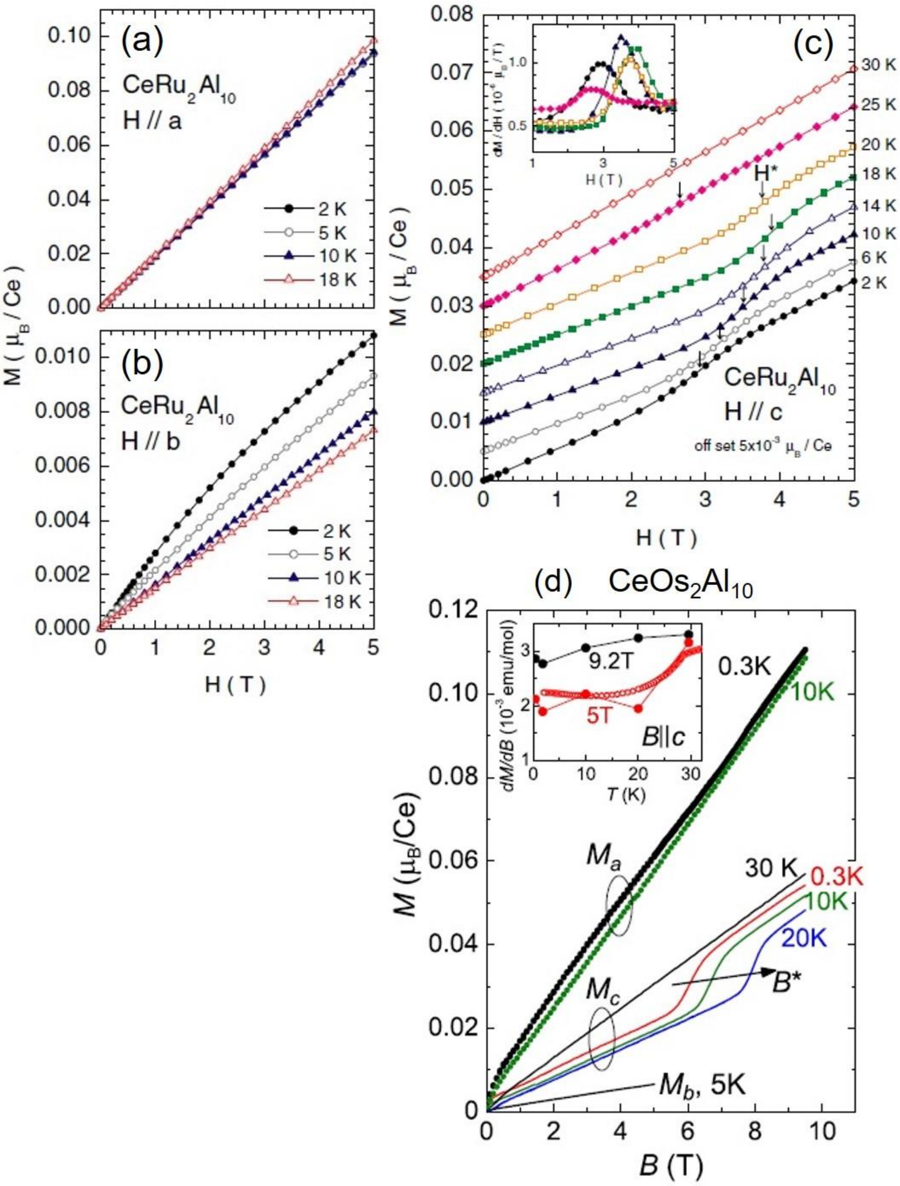

Figure 1.26: Isothermal magnetization for (a)-(c) $CeRu_2Al_{10}$ and (d) $CeOs_2Al_{10}$ for $B//a$, $B//b$, and $B//c$, respectively [50,69].

1.3.3 Substitution effects on the magnetic, transport, and optical properties of CeT_2Al$_{10}$ (T = Fe, Ru, and Os)

Chemical substitutions at the transition metal T site in CeT_2Al$_{10}$ have been used to investigate how the magnetic properties depend on the electronic states derived from T atoms.

Ce(Ru$_{1-x}$Fe$_x$)$_2$Al$_{10}$

The physical properties of Ce(Ru$_{1-x}$Fe$_x$)$_2$Al$_{10}$ have been reported by several research groups [59,71,72,73]. The lattice parameters along the three principal axes decrease gradually with increasing Fe composition x as shown in Fig. 1.27 (a) [72]. While going from $x = 0$ to $x = 1$, the unit cell contracts by about 3.5%. Fig. 1.27 (b)-(d) show the inverse magnetic susceptibility $1/\chi$, normalized electrical resistivity $\rho(T)$, and C/T of polycrystalline samples of Ce(Ru$_{1-x}$Fe$_x$)$_2$Al$_{10}$ [73]. With increasing x, the temperature at the minimum in $1/\chi$ gradually increases, indicating enhancement of the Kondo coupling. In $\rho(T)$, the semiconducting behavior observed between 70 K and 30 K for $x = 0$ becomes vague for $x = 0.6$, then a maximum in $\rho(T)$ appears at $x = 0.7$. For $x = 0.5$ and 0.6, a broadened jump of C/T due to an AFM transition is observed at 22 K and 17 K, respectively. Such a jump is not observed for $x \geq 0.7$.

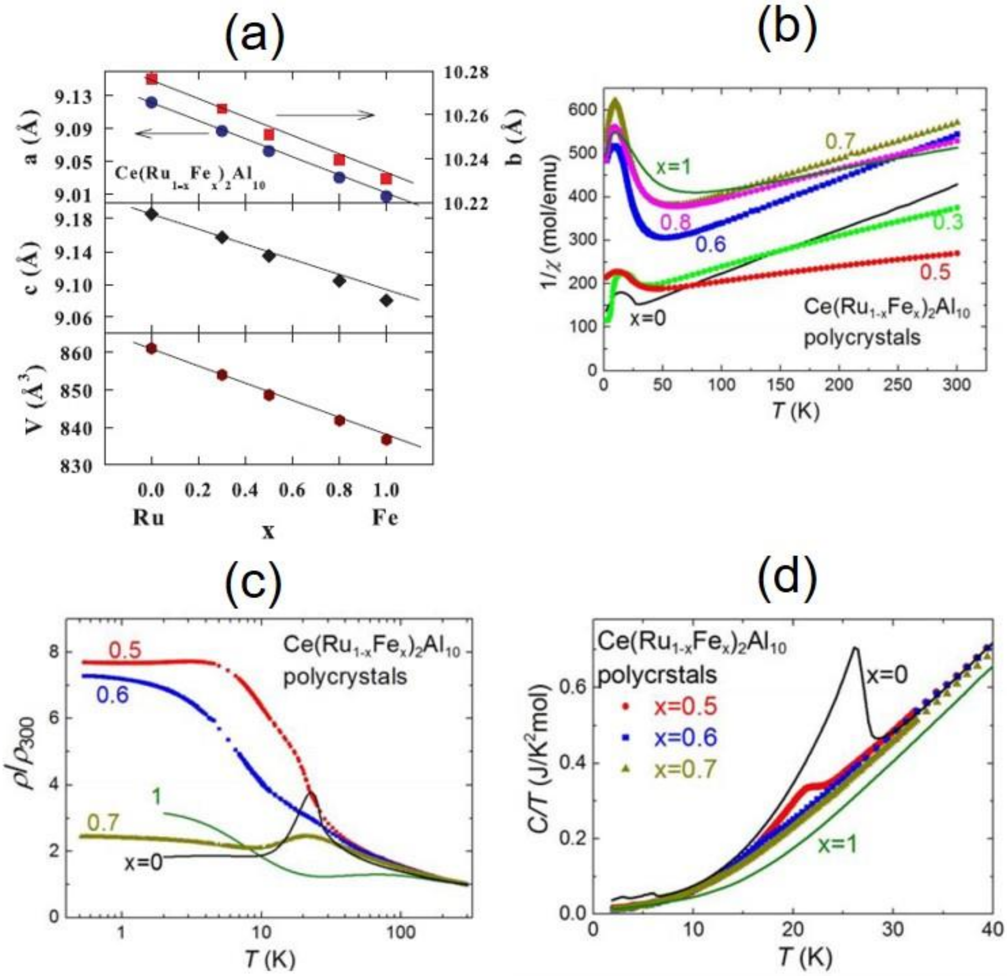

Figure 1.27: (a) Lattice parameters and unit cell volume versus Fe composition x in the alloys $Ce(Ru_{1-x}Fe_x)_2Al_{10}$ ($0 \leq x \leq 1$) [72]. Temperature dependences of (b) inverse magnetic susceptibility $1/\chi$, (c) electrical resistivity $\rho(T)$ normalized by the value at 300 K, ρ/ρ_{300K}, and (d) specific heat divided by temperature C/T [73].

$Ce(Ru_{1-x}Rh_x)_2Al_{10}$ and $Ce(Os_{1-x}Ir_x)_2Al_{10}$

Significant effects of substitutions of Rh for Ru in $Ce(Ru_{1-x}Rh_x)_2Al_{10}$ and Ir for Os in $Ce(Os_{1-x}Ir_x)_2Al_{10}$ on the physical properties have been reported [74-76]. Fig. 1.28 (a)-(c) show the temperature dependences of $\chi(T)$, $\rho(T)$, and C/T of single-crystalline samples of $Ce(Ru_{1-x}Rh_x)_2Al_{10}$ [74,75]. For $x = 0.05$, the sharp peak in χ for $B//a$ and the absence of the drop in χ for $B//c$ at $T < T_N$ suggested that the AFM ordered moments μ_{AFM} are oriented parallel to the easy a axis. This reorientation of μ_{AFM} from the c-axis for $x = 0$ to the a-axis for $x = 0.05$ is confirmed by the isothermal magnetization and neutron diffraction measurements [77]. Concomitantly, the size of μ_{AFM} is increased by three times. However, both the T_{N} and the transport gap in $\rho(T)$ are strongly suppressed. In $\mathrm{Ce(Os_{1-\mathit{x}}Ir_{\mathit{x}})_2Al_{10}}$, similar enhancement and reorientation of μ_{AFM} as well as the suppression of transport gap occur at $x = 0.08$ as shown in Fig. 1.28 (d)-(f) [76,78]. Therefore, it has been argued that the hybridization of the 4*f* electron with the 4*d* or 5*d* electrons of the *T* elements plays an important role in the unusual magnetic order.

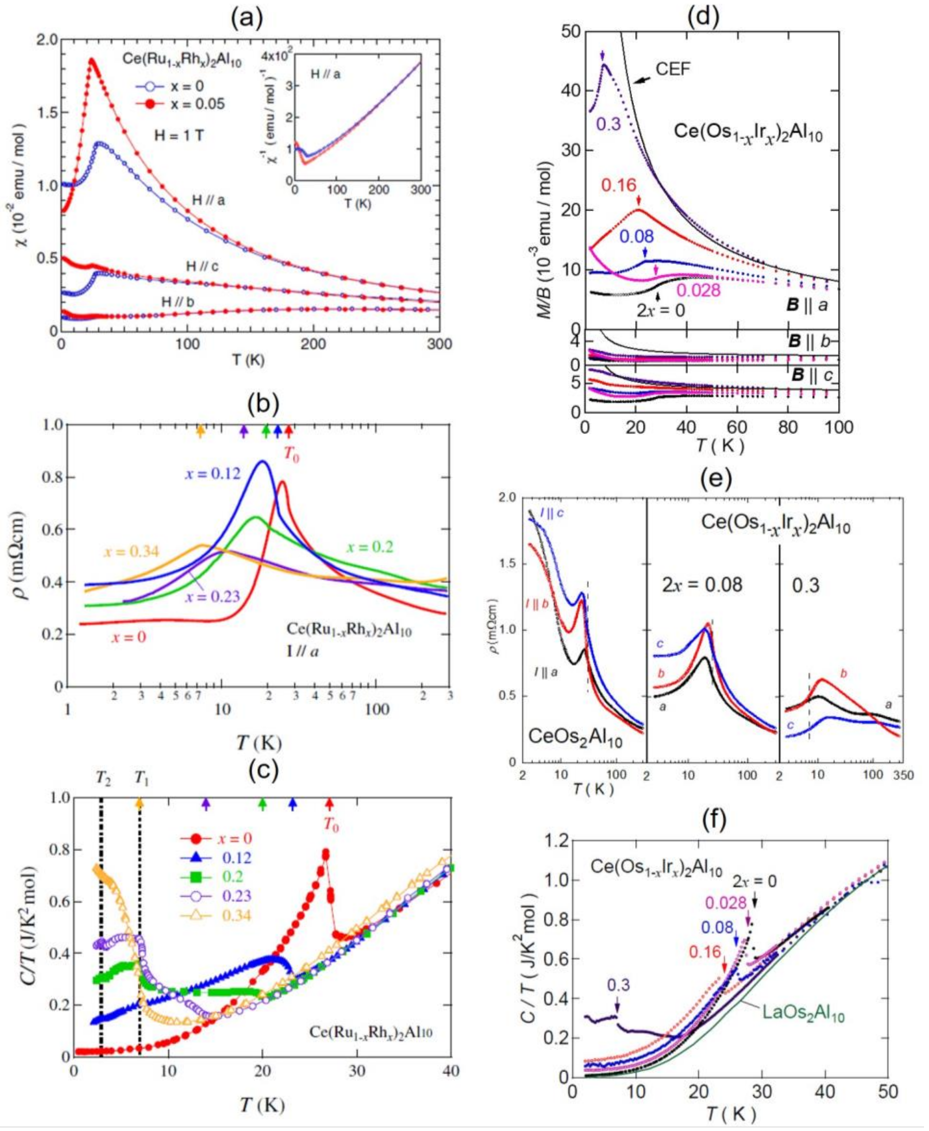

Figure 1.28: Temperature dependences of χ, ρ and C/T for single-crystalline samples of (a)-(c) $\mathrm{Ce(Ru_{1-\mathit{x}}Rh_{\mathit{x}})_2Al_{10}}$ and (d)-(f) $\mathrm{Ce(Os_{1-\mathit{x}}Ir_{\mathit{x}})_2Al_{10}}$ [74-76].

$CeRu_2Al_{10-y}Si_y$

On the other hand, it was expected that the Al 3*p* electron states also hybridize with the Ce 4*f* states. In fact, as shown in Fig. 1.29 (a), the resistivity $\rho(T)$ of $CeRu_2Al_{9.9}Si_{0.1}$ showed that the transport gap is suppressed and T_N is decreased to 23 K [79]. Furthermore, as shown in Fig. 1.29 (b), $\chi_a(T)$ is enlarged and the drop in $\chi_b(T)$ at T_N disappeared, suggesting reorientation of μ_{AFM} from the *c* axis to the *a* axis. In order words, doping of 3*p* electrons to $CeRu_2Al_{10}$ strongly suppresses both the T_N and hybridization gap. Because the number of 3*p* electrons added by Si substitution in $CeRu_2Al_{9.9}Si_{0.1}$ is equal to that of 4*d* electrons in $Ce(Ru_{0.95}Rh_{0.05})_2Al_{10}$, it was pointed out that the 3*p* electron doping gives an equivalence effect with that of the 4*d* electron doping.

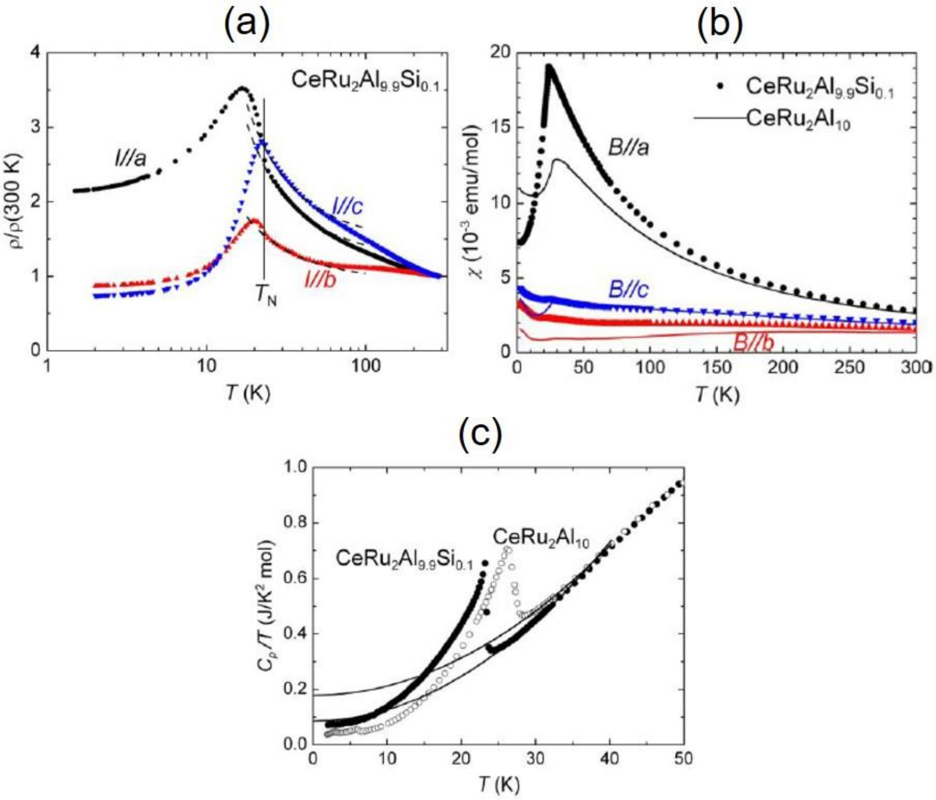

Figure 1.29: Temperature dependences of (a) ρ/ρ_{300K}, (b) χ and (c) C/T for single-crystalline samples of $CeRu_2Al_{10}$ and $CeRu_2Al_{9.9}Si_{0.1}$ [79].

1.3.4 Pressure effects on the magnetic, transport, and optical properties

of CeT_2Al$_{10}$ (T = Fe, Ru, and Os)

Fig. 1.30 (a)-(c) and (d)-(f) show the temperature dependences of $\rho(T)$ along the a-axis of CeT_2Al$_{10}$ (T = Fe, Ru, and Os) and $\chi(T)$ of T = Ru and Os along the three principal axes under hydrostatic pressures, respectively [49,80-83]. Upon application of hydrostatic pressure on CeRu$_2$Al$_{10}$, both $\rho(T)$ and $\chi(T)$ approximate those of CeOs$_2$Al$_{10}$ under ambient pressure. In fact, the behavior of $\rho(T)$ for T = Ru at P = 2.0 GPa is analogous to that for that of T = Os at ambient pressure. Under pressure, the maxima of $\chi_a(T)$ and $\chi_c(T)$ at 45 K for T = Os are suppressed and the temperatures at the maximum $T_{\chi\mathrm{m}}$ is increased. These changes in $\chi(T)$ and ρ (T) indicate that application of pressure enhances the c-f hybridization in these systems.

On the other hand, as shown in Fig 1.30 (c), T_N for T = Os rises slightly with pressure up to 0.7 GPa, and then decreases at higher pressures. As shown in Fig 1.30 (g), the jump of d(χT)/dT around T_N decreases with increasing pressure. For an antiferromagnet, d(χT)/dT near T_N is known to be proportional to the specific heat jump ΔC [84]. In fact, d(χT)/dT at ambient pressure is well scaled by the magnetic contribution to the specific heat C_m. Fig. 1.31(a) represents the pressure dependences of T_N, T_max, activation energies $\Delta_\mathrm{H}/k_\mathrm{B}$ for $T > T_\mathrm{N}$ and $\Delta_\mathrm{L}/k_\mathrm{B}$ for $T < T_\mathrm{N}$ in $\rho_a(T)$, and the jump of d(χT)/dT at T_N for T = Os. With increasing pressure, $\Delta_\mathrm{H}/k_\mathrm{B}$ decreases steeply, while $\Delta_\mathrm{L}/k_\mathrm{B}$ gradually approaches zero at a critical pressure $P_\mathrm{c} \simeq 2.5$ GPa. the jump of d(χT)/dT at T_N linearly decreases with pressure and vanishes at P_c.

Fig. 1.31(b) shows the pressure dependence of T_N for T = Ru and T = Os. T_N increase to the maxima at 32 and 29 K, and abruptly disappear at 5.0 and 2.5 GPa, respectively [49,81-83]. These dependences of T_N seem to be consistent with a recent phase diagram of T_N as a function of the Kondo exchange coupling, which was constructed by the dynamical mean field calculation for an anisotropic Kondo lattice model [61].

Let us move to the relation between T_N and the lattice parameters. Fig 1.31(c) shows the variations of T_N for Ce(Ru$_{1-x}$Fe$_x$)$_2$Al$_{10}$ vs x and T_N of CeRu$_2$Al$_{10}$ vs P. We compare the lattice contractions by Fe substitution with that by application of hydrostatic pressure in Fig. 1.31(d). The $T_N(x)$ monotonically decrease with x without showing the maximum found in $T_N(P)$ at 32 K. Under hydrostatic pressure at room temperature, the lattice parameters of $CeRu_2Al_{10}$ decrease in a similar way as $LaRu_2Al_{10}$, whereby $\Delta b/b_0$ is 80% of $\Delta a/a_0 \simeq \Delta c/c_0$ [85]. However, in case of chemical pressure caused by substitution of Fe for Ru, $\Delta b/b_0$ is only 50% of $\Delta a/a_0 \simeq \Delta c/c_0$ [72]. This smaller change in the b axis parameter compared with that under hydrostatic pressure was thought to be responsible for the monotonic decrease in T_N with x in $Ce(Ru_{1-x}Fe_x)_2Al_{10}$ [73].

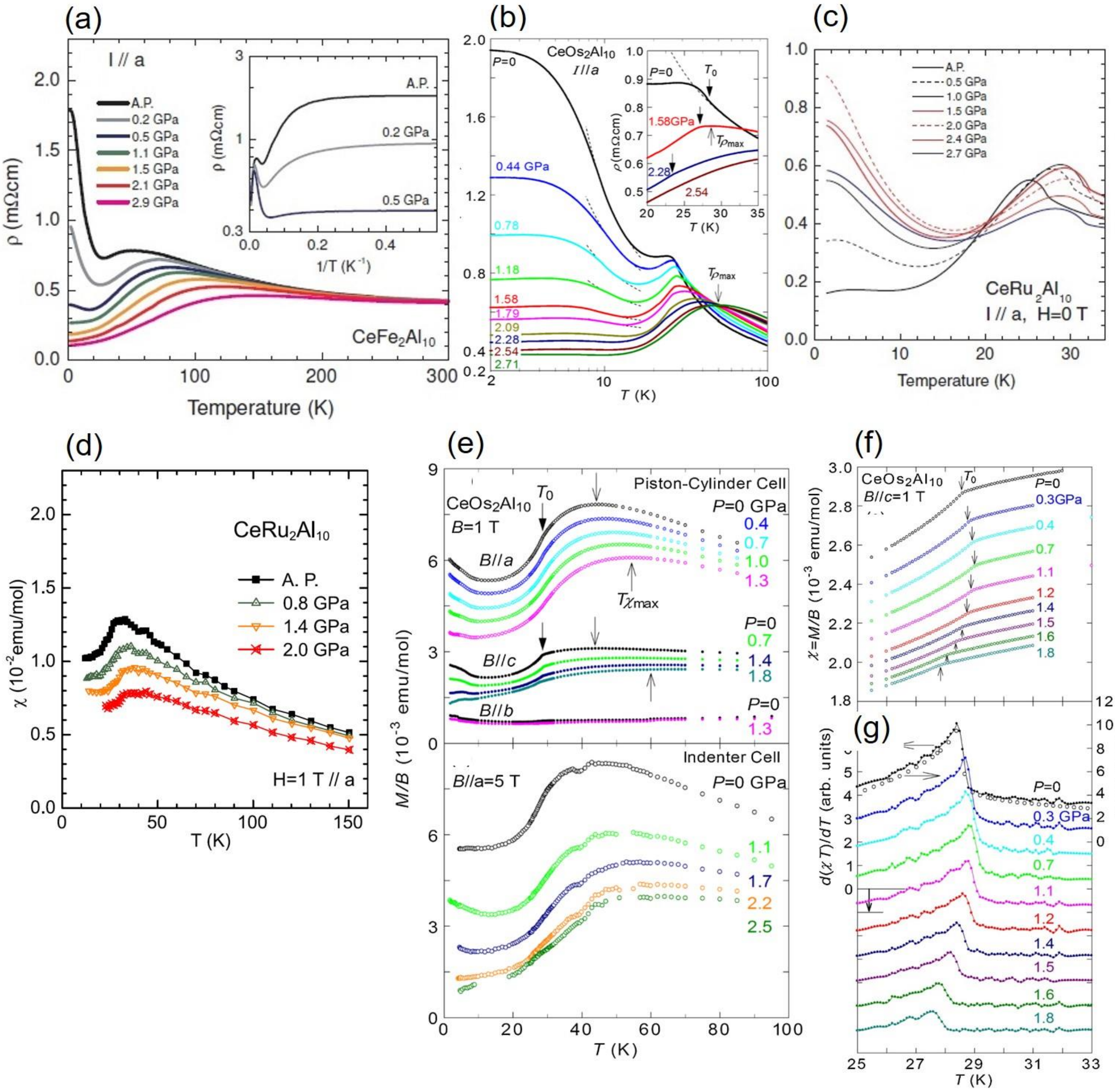

Figure 1.30: Temperature dependences of (a)-(c) $\rho(T)$ along the *a* axis for CeT_2Al$_{10}$ (T = Fe, Ru, and Os) under various hydrostatic pressures [80-82], (d) $\chi(T)$ for T = Ru and (e)-(f) T = Os, and d(χT)/dT for T = Os under $B//c$. The data of the magnetic contribution C_m to the specific heat at $P = 0$ is cited from Fig. 1.17.

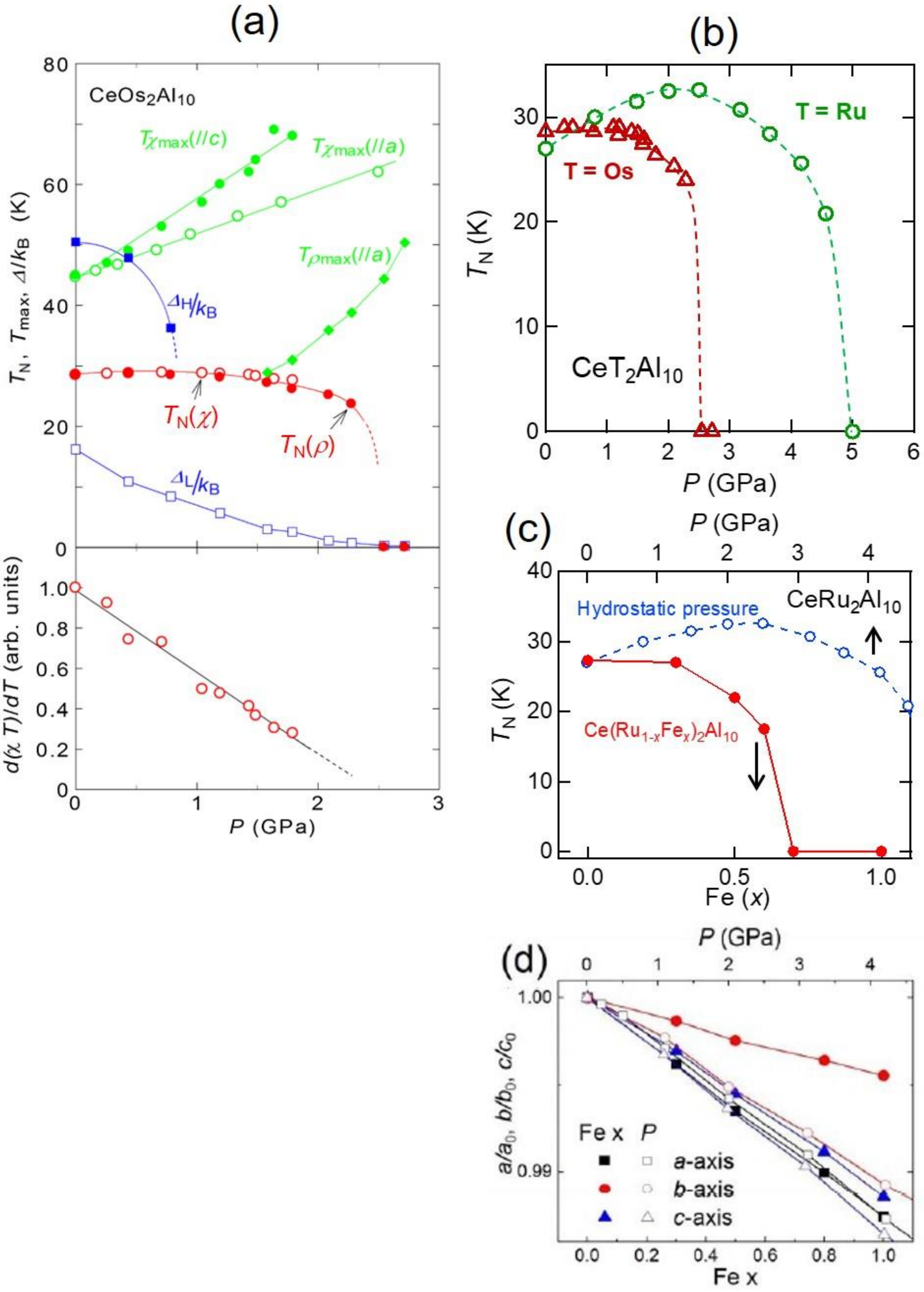

Figure 1.31: Pressure dependences of (a) T_N, T_{max} in $\chi_a(T)$, activation energies in $\rho_a(T)$ Δ_H/k_B for $T > T_N$, and Δ_L/k_B for $T < T_N$ and of the jump of $d(\chi T)/dT$ at T_N for CeOs$_2$Al$_{10}$ [82]. (b) Pressure dependences of T_N for CeT_2Al$_{10}$ (T = Ru and Os) [49,80,82]. (c) T_N vs x in Ce(Ru$_{1-x}$Fe$_x$)$_2$Al$_{10}$ and T_N vs pressure P for CeRu$_2$Al$_{10}$ [49,73,80]. (d) Normalized lattice parameters for Ce(Ru$_{1-x}$Fe$_x$)$_2$Al$_{10}$ as a function of x and for CeRu$_2$Al$_{10}$ as a function of P [72,85].

The direction of the ordered moments μ_{AFM} in CeT_2Al$_{10}$ is easily changed by applications of magnetic field and pressure as well as atomic substitution. Fig. 1.32 (a) and (b) show $\chi(T)$ and magnetization $M(B)$ of Ce$_{1-x}$La$_x$Ru$_2$Al$_{10}$, respectively [86]. The spin flop transition at $B^*\sim$ 4 T for $x = 0$ decreases with increasing x. For $x = 0.1$, metamagnetic anomaly is absent in $M(B//c)$, although $\chi(T)$ exhibits the anomaly at T_{N}. The AFM state with $\mu_{\mathrm{AFM}}//b$ is stabilized even in zero field, which was confirmed by neutron diffraction experiments [87].

Fig. 1.33 (b) shows pressure dependence of B^* which was determined by the magnetoresistance of Ce$_{1-x}$La$_x$Ru$_2$Al$_{10}$ ($x = 0$, 0.03, and 0.1) at 1.4 K for $I//c$ and $B//c$ under various pressures as shown in Fig. 1.33(a). Fig. 1.33 (c) shows the pressure dependence of T_{N} for Ce$_{1-x}$La$_x$Ru$_2$Al$_{10}$. The AFM structure for $x = 0.1$ changes from $\mu_{\mathrm{AFM}}//b$ at $P = 0$ to $\mu_{\mathrm{AFM}}//c$ at $P = 0.3$ GPa, while T_{N} remains unchanged [86]. This fact suggested that the mechanism for the high T_{N} is different from that determines the direction of μ_{AFM}. The strong sensitivity of the AFM structure to the pressure and substitution supported the idea that the anisotropic c-f hybridization plays an essential role in the unusual AFM order of CeT_2Al$_{10}$ (T = Ru and Os).

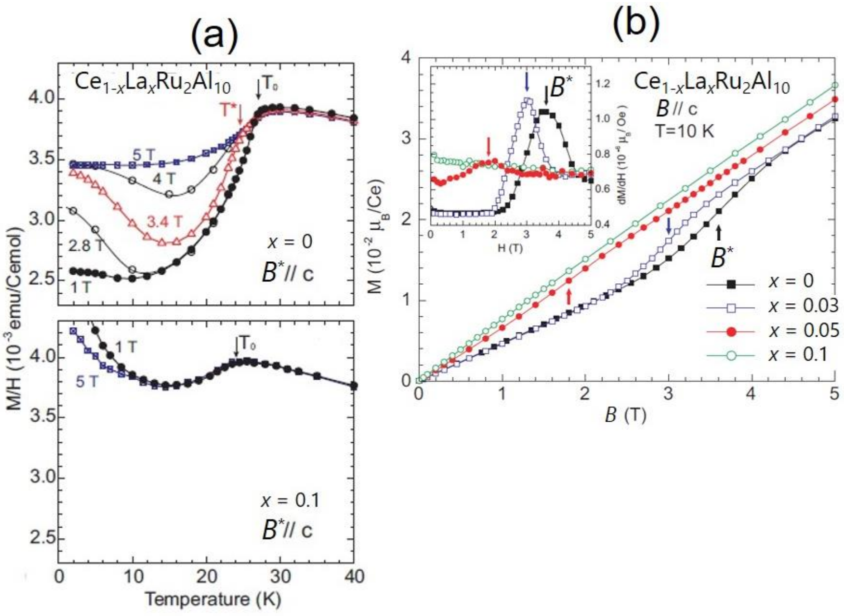

Figure 1.32: (a) Temperature dependence of $\chi(T)$ for Ce$_{1\text{-}x}$La$_x$Ru$_2$Al$_{10}$ (x = 0 and 0.1) [86]. (b) Magnetic field dependence of magnetization for Ce$_{1\text{-}x}$La$_x$Ru$_2$Al$_{10}$ ($0 \leq x \leq 0.1$) at 10 K.

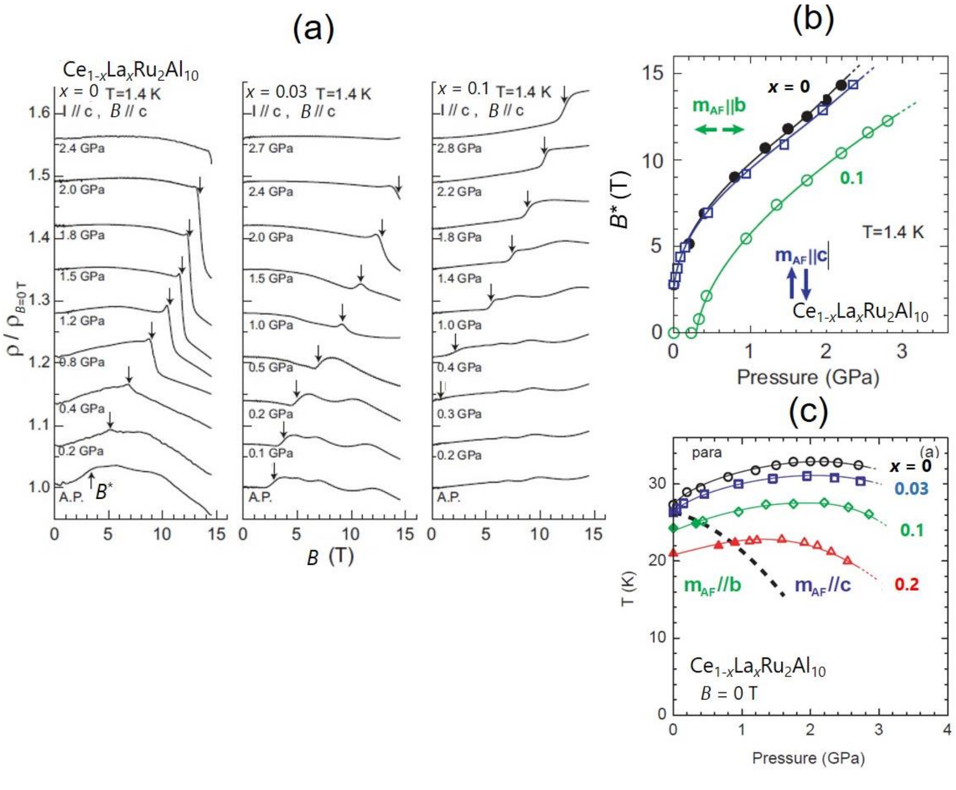

Figure 1.33: (a) Magnetoresistance $\rho(B)$ of Ce$_{1\text{-}x}$La$_x$Ru$_2$Al$_{10}$ (x = 0, 0.03, and 0.1) at 1.4 K for $I//c$ and $B//c$ under various pressures, where vertical scales are normalized by the value at B = 0 T and shifted with an offset [86]. (b) Pressure dependence of spin-flop transition field B^* for Ce$_{1\text{-}x}$La$_x$Ru$_2$Al$_{10}$ (x = 0 and 0.1). (c) Pressure dependence of T_N for Ce$_{1\text{-}x}$La$_x$Ru$_2$Al$_{10}$ ($x \leq$ 0.2).

1.4 Purpose of the present study

The compounds CeT_2Al$_{10}$ (T = Ru and Os) with the orthorhombic YbFe$_2$Al$_{10}$-type structure show semiconducting transport properties and yet exhibit an antiferromagnetic (AFM) transition [43,46,48-50,52-54]. The AFM order has two unusual characteristics. One is the unexpectedly high ordering temperatures T_N, 27 K and 28.5 K for T = Ru and Os, respectively, which temperatures are higher by 10 K than T_N of the Gd counterparts [64,65]. The study of polarized optical conductivity for CeT_2Al$_{10}$ has revealed that a kind of charge density waves (CDW) develops along the *b* axis at 36 K far above T_N [67,68]. Then, it was proposed that opening of the CDW-like gap along the *b* axis induces the AFM order. The other strange fact is that the direction of ordered moments along the *c* axis is different from the *a* axis that is the easy magnetization axis preferred by the CEF in the paramagnetic state [69,70]. To explain this puzzle, it was conjectured that the strong hybridization along the *a* axis prevents the moments from pointing to the *a* axis [45,70]. Despite extensive studies, the relation among the anisotropic *c*-*f* hybridization, AFM transition at high T_N, and ordered moment direction along the hard axis remains unresolved.

The present study aims to clarify the relation between the anisotropic *c*-*f* hybridization and unusual AFM order in CeT_2Al$_{10}$ (T = Ru and Os). For that purpose, we conducted two experiments. First, we have investigated the 3*p* electron doping effect of the Al site in CeRu$_2$Al$_{10}$. For polycrystalline samples of CeRu$_2$Al$_{10-y}$Si$_y$ ($y \leq 0.38$), we have measured the magnetic susceptibility, electrical resistivity, and specific heat C. Second, in order to control the *c*-*f* hybridization, we have applied uniaxial pressure on the single crystals of CeT_2Al$_{10}$ (T = Ru and Os). we have measured the magnetization and specific heat at low temperatures and strains at room temperature.

Chapter 2

Sample preparation and characterizations

2.1 Preparation of polycrystales of $CeRu_2Al_{10-y}Si_y$ and single crystals of CeT_2Al_{10} (T = Fe, Ru, and Os)

Starting materials used to prepare polycrystals and single crystals for the present work are listed in Table 2.1. Powder of Ru and Os was pressed into pellets of 0.5g each, which were arc melted into balls. Polycrystalline samples of $CeRu_2Al_{10-y}Si_y$ ($0 \leq y \leq 0.5$) were prepared by arc melting the constituent amounts of pure elements under a purified argon atmosphere. The obtained ingots were sealed in an evacuated quartz ampoule and then annealed at 800°C for one week [48].

Single crystals of CeT_2Al_{10} (T = Fe, Ru, and Os) were grown using an Al self-flux method [50]. Binary alloys of CeT_2 were prepared by arc melting of pure elements to avoid distribution of T elements with high melting points. Al used as a flux has a relatively low melting point at 661°C and reacts with quartz. In order to prevent this reaction, the crushed ingots of the alloy together with an excess amount of Al in the ratio 1:2:30 were loaded into a magnesia or alumina crucible. As shown in Fig. 2.1, the crucible was sealed in a quartz ampoule under an Ar atmosphere of 1/3 atm. Fig. 2.2 and 2.3 display the temperature programs for the crystal growth of $CeFe_2Al_{10}$ and CeT_2Al_{10} (Ru and Os), respectively. The mixture of $CeFe_2$ and Al_{30} in the magnesia crucible was heated to 900°C, kept for 12 hours, and then slowly cooled at a rate 2°C/h (Fig. 2.2). The mixture of $CeRu_2$ ($CeOs_2$) and Al_{30} in the alumina crucible were heated to 1150°C (1200°C) for 5 hours and then cooled at a rate 2°C/h (Fig. 2.3). The ampoule was removed from the box furnace at 720°C to centrifuge the Al flux. The residual Al was etched with aqueous NaOH solution. The single crystals of CeT_2Al$_{10}$ (T = Fe, Ru, and Os) are shown in Fig. 2.4.

Table 2.1: Starting materials used for the preparation of samples of CeT_2Al$_{10}$ (T = Fe, Ru, and Os). The materials supplied from companies with * were used for polycrystals.

Materials	Suppliers	Purity	Shape
Ce	Ames Lab. MPC	4N	Rod
Ce	Rare Metallic*	3N	Lump
Os	Tanaka Kikinzoku	3N	Powder
Ru	Tanaka Kikinzoku	3N	Powder
Fe	Rare Metallic	4N	Ingot
Al	Rare Metallic*	5N	Ingot
Al	Alfa Aesar	5N	Rod
Si	Rare Metallic	5N	Chip

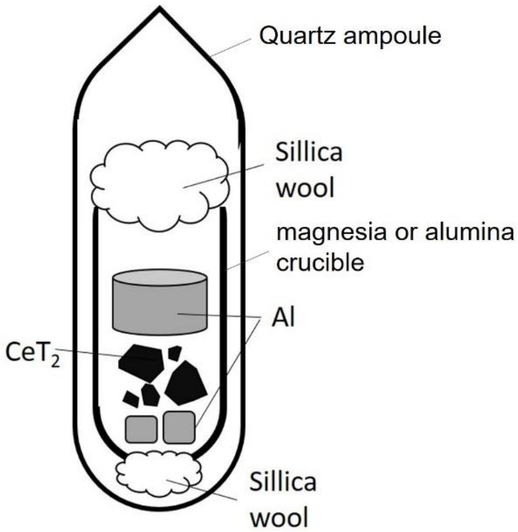

Figure 2.1: Quartz ampoule encapsulating CeT_2 (T = Fe, Ru, and Os) crushed ingot and pieces of Al for the single crystal growth. The silica wool was placed above and below the crucible made of magnesia or alumina.

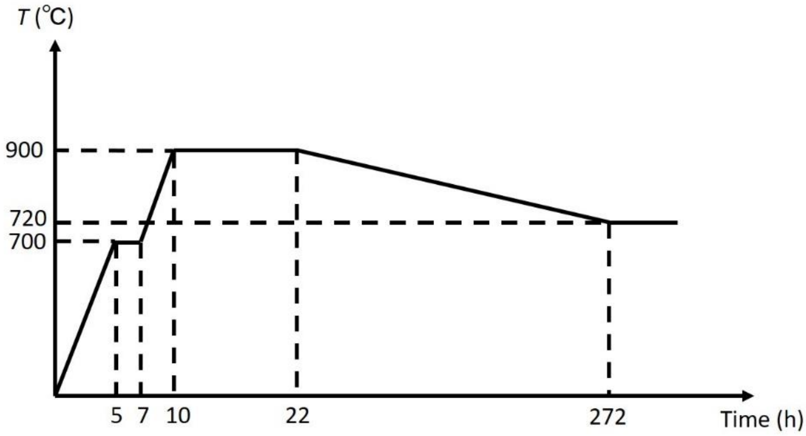

Figure 2.2: Temperature program as a function of time for the growth of single crystals of $CeFe_2Al_{10}$.

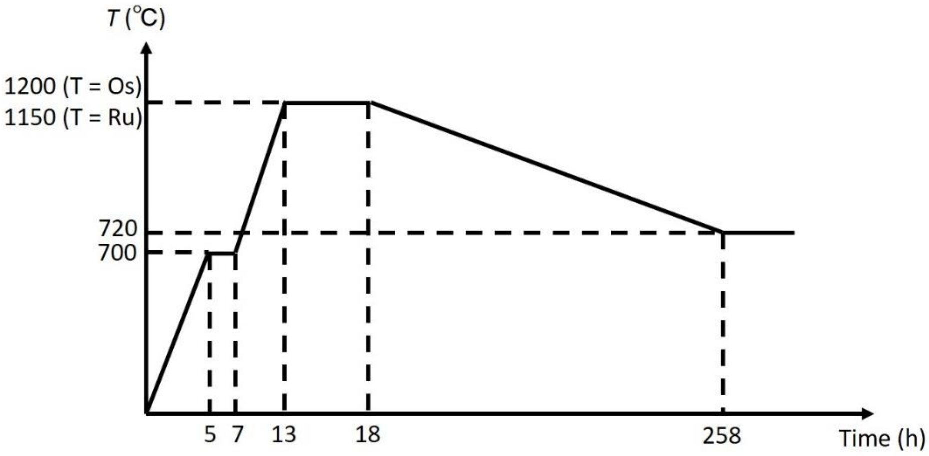

Figure 2.3: Temperature program as a function of time for the growth of single crystals of CeT_2Al_{10} (T = Ru, Os).

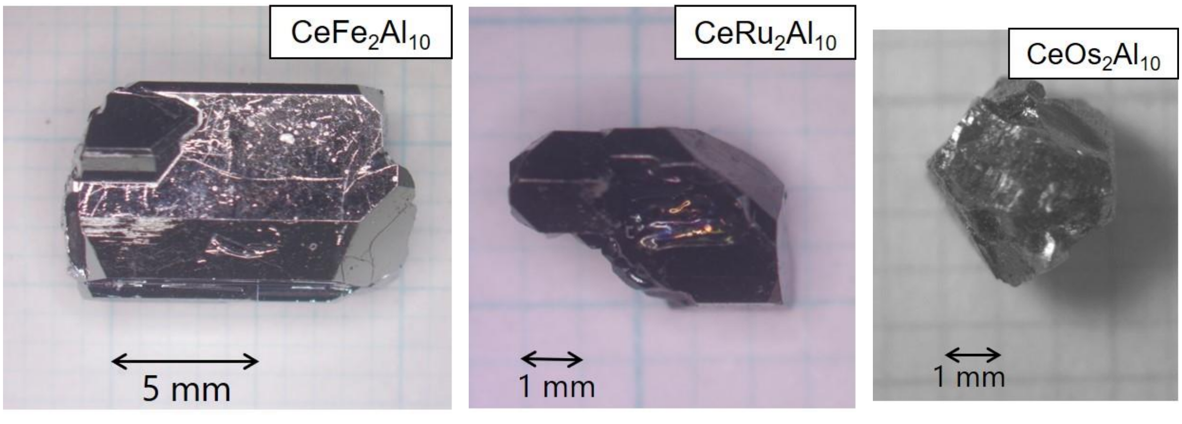

Figure. 2.4: Photographs of the single crystals of CeT_2Al_{10} (T = Fe, Ru, and Os).

2.2 Characterizations of samples

The samples were characterized by combining powder x-ray diffraction (Rigaku UltimaIV) with a Cu target (TOSHIBA Copper-A-41, $V = 40$ kV and $I = 30$ mA), Laue back diffraction (TRYSE TRY-IPLC) with a W target (TOSHIBA Tungsten-A-40, $V = 25$ kV and $I = 20$ mV). The chemical composition was determined by the wavelength dispersive electron-probe microanalysis (EPMA, JEOL JXA-8100) and the energy dispersive x-ray analysis (EDX, HITCHI EDAX). From the powder x-ray diffraction patterns, the crystallographic structures and the lattice parameters have been determined by the analysis software RIETAN-FP [88]. Back scattered electron (BSE) images of the polished surface of the samples were observed by the EPMA and EDX system operated at 20 keV.

2.2.1 X-ray diffraction

Powder x-ray diffraction patterns of $CeRu_2Al_{10-y}Si_y$ in the diffraction range $10° \leq 2\theta \leq 120°$ are shown in Fig. 2.5. The diffraction peaks are indexed by the orthorhombic $YbFe_2Al_{10}$-type structure. The lattice parameters and lattice volume linearly decrease with increasing y as shown in Fig. 2.6. Since the change in the volume is smaller than 0.3% for $y \leq 0.38$, we expect that the chemical pressure effect on the c-f hybridization may be much weaker than that of doping of 3p electrons.

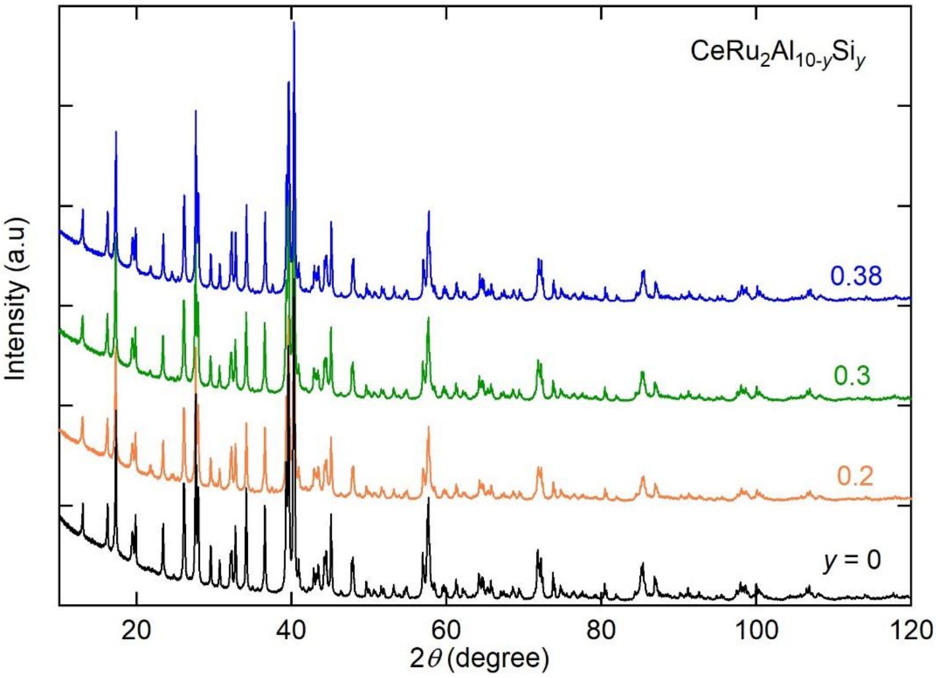

Figure 2.5: Powder x-ray diffraction patterns of polycrystalline samples of $CeRu_2Al_{10-y}Si_y$ for $0 \leq y \leq 0.38$.

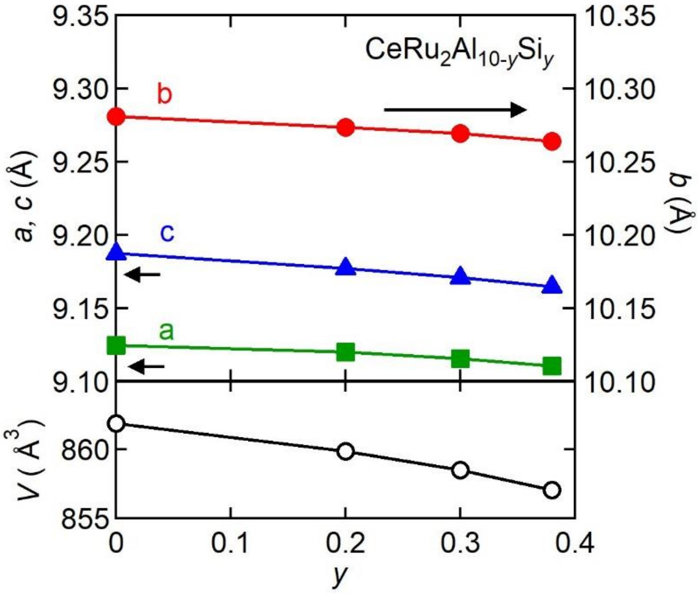

Figure 2.6: Lattice parameters a, b, and c and unit cell volume V of $CeRu_2Al_{10-y}Si_y$ as a function of y.

2.2.2 Electron microscopy

Fig. 2.7, 2.8, and 2.9 are the back scattered electron images for polished polycrystalline samples prepared from initial compositions $CeRu_2Al_{10-Y}Si_Y$ with $Y = 0.2$, 0.3, 0.38, and 0.5. The compositions determined by EPMA ($Y = 0.2$) or EDX ($Y = 0.3$, 0.38, and 0.5) are listed in Table 2.2. In the BSE image of Fig. 2.7, the framed area is the bottom of the ingot, which was rapidly cooled on the hearth. The gray areas are $CeRu_2Al_{9.8}Si_{0.2}$, while the white areas have an average composition of CeAlSi. For the measurement of physical properties, the areas of impurities were carefully removed. As shown in Fig. 2.8, the BSE images for $Y = 0.3$ and 0.38 are rather homogeneous without impurity phases. The compositions of EDX analysis are consistent with the nominal composition. For the sample with $Y = 0.5$, we find three phases. The dominant gray phase is the $CeRu_2Al_{10-y}Si_y$ phase with $y = 0.4$, the dark gray phase is $RuAl_4$, and the white phase has an average composition of CeAlSi. The last phase belongs to have a wide homogeneity range $CeAl_xSi_{2-x}$ ($0.45 \leq x \leq 1.28$) keeping the α-$ThSi_2$-type structure [89,90]. Therefore, nearly single-phase samples of $CeRu_2Al_{10-y}Si_y$ were obtained with $y \leq 0.38$, for which physical properties have been measured.

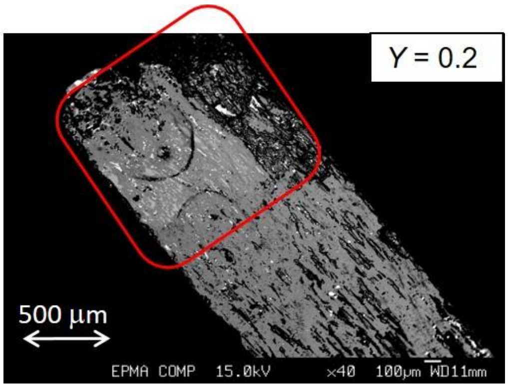

Figure 2.7: Backscattered electron image for the polished sample CeRu$_2$Al$_{10-Y}$Si$_Y$ with the initial composition Y = 0.2. The framed area is the bottom of the ingot which was rapidly cooled on the hearth.

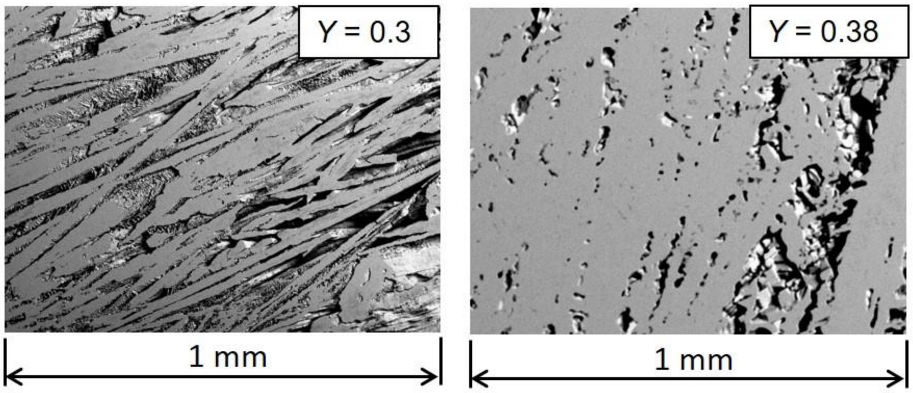

Figure 2.8: Backscattered electron images for the polished samples CeRu$_2$Al$_{10-Y}$Si$_Y$ with the initial compositions Y = 0.3 and 0.38, respectively.

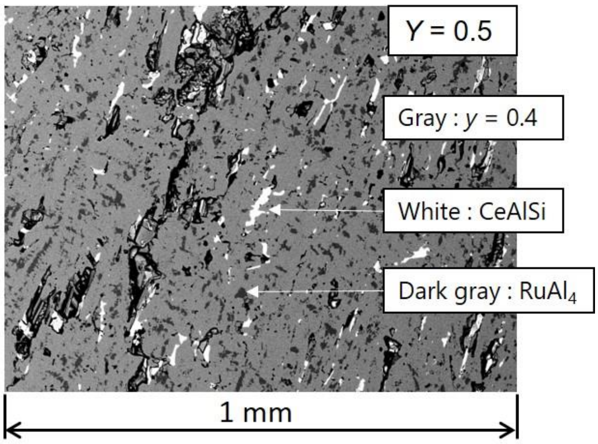

Figure 2.9: Backscattered electron image for the polished sample CeRu$_2$Al$_{10-Y}$Si$_Y$ with the initial composition Y = 0.5.

2.2.3 Orienting crystal direction

The single crystals of CeT_2Al$_{10}$ (T = Fe, Ru, and Os) were oriented by the Laue method and shaped by the spark erosion for the measurements of strain, magnetic susceptibility, specific heat, and electrical resistivity, respectively. The Laue photos taken for these planes are shown in Fig. 2.10, which are in accord with simulated patterns in the Fig. 2.11.

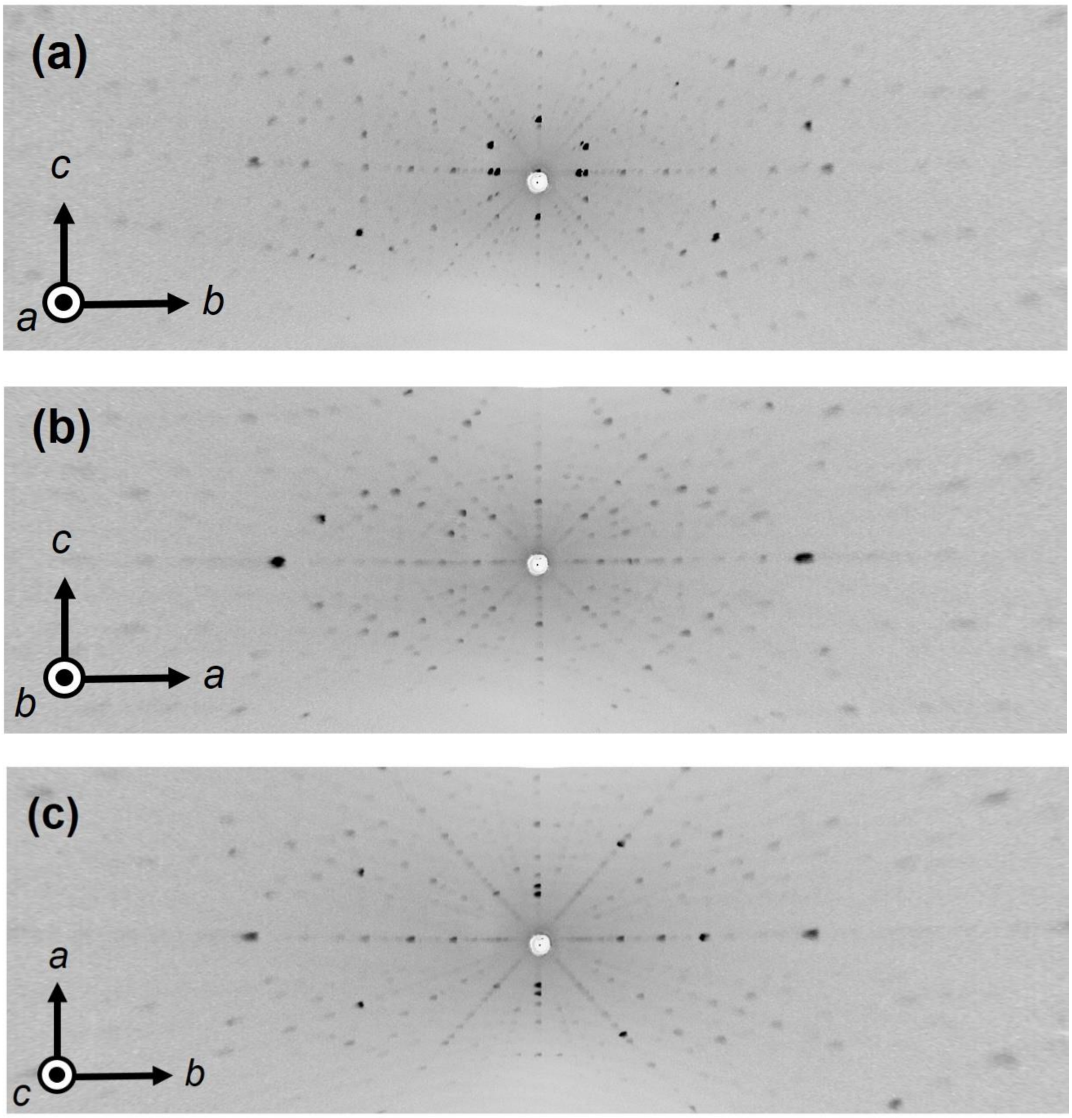

Figure 2.10: X-ray Laue pictures of a CeFe$_2$Al$_{10}$ single crystal oriented in the (a) (1 0 0), (b) (0 1 0), and (c) (0 0 1) directions, respectively.

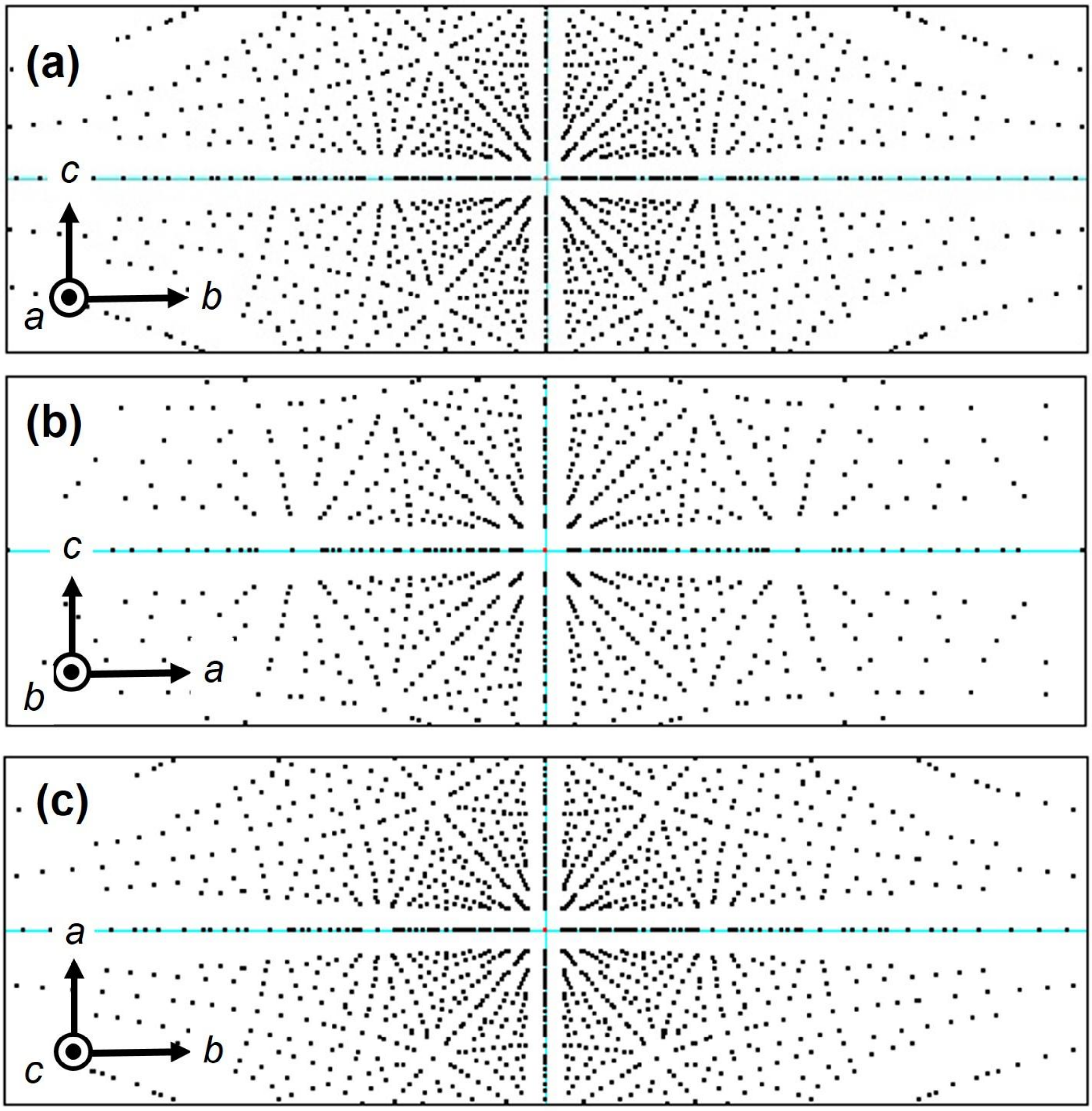

Figure 2.11: X-ray Laue patterns simulated for $CeFe_2Al_{10}$ oriented in the (a) (1 0 0), (b) (0 1 0), and (c) (0 0 1) directions, respectively.

Chapter 3

Experimental methods

3.1 Measurements of magnetic, transport, and thermal properties under ambient pressure

3.1.1 Magnetization

The magnetization was measured by using a commercial superconducting quantum interference device (SQUID) magnetometer. The temperature dependence of magnetization $M(T)$ was measured in an external field $B = 1$ T from 2 to 300 K. The isothermal magnetization $M(B)$ at 2 K was measured up to $B = 5$ T.

3.1.2 Electrical resistivity

The electrical resistivity was measured by a standard DC four-probe method on the sample of a typical dimension of $0.5 \times 0.5 \times 2$ mm^3. As electrical leads, four Ag wires of 50μm indiameter (Nilaco) were connected to the sample surface by using spot welder and Ag paste (Tamura Seisakusho VL-10). A ^{3}He cryostat was used for the measurement in the temperature range from 0.5 K to 300 K. In order to exclude the influence of the thermoelectro-motive force caused by the temperature gradient in the sample, the DC current was inverted at each temperature, thereby the average of the voltages V^+ and V^- was taken as the voltage.

3.1.3 Specific heat

Specific heat measurements were performed by a thermal relaxation method using a PPMS (Quantum Design Inc.) in the temperature range 2–50 K. The sample platform in the PPMS heat capacity option is shown in Fig. 3.1. A sample plate of approximately 10 mg was mounted on the platform. The sample was thermally connected to the addenda with Apiezone N-grease. The PPMS controls the heat supplied to and released from the sample while monitoring the resulting change in temperature T. The amount of heat $P(t)$ is equal to P_0 during the heating portion of the measurement and equal to zero during the cooling portion. Based on the temperature response in the cooling period, the relaxation time τ is calculated. The entire response of the sample platform is fit to a model that accounts for both the thermal relaxation of the sample platform to the bath temperature and that of the sample platform to sample itself. The τ leads to heat capacity at constant pressure C by using the equations as described below.

$$\tau = \frac{C}{K} = \frac{C_s + C_h}{K_W}, \tag{3.1}$$

$$K_W = \frac{1}{\Delta T}, \tag{3.2}$$

$$C = K_W \tau = \frac{P_\tau}{\Delta T}, \tag{3.3}$$

$$C_s = \frac{P_\tau}{\Delta T} - C_h, \tag{3.4}$$

where C_{h} and C_{S}, are respectively the heat capacities of the sample platform and sample, and K_{w} is the thermal conductance of the wires of Au-35%Pd.

Two-tau model

The two-tau model is used to measure the heat capacity of the sample when poor thermal attachment of the sample to the platform produces a temperature difference between the two. This model simulates the effect of heat flowing between the sample platform and puck. The following equations express the two-tau model.

$$P(t) = \int_{T_S(t)}^{T_P(t)} K_W(T')dT' + \int_{T_S(t)}^{T_P(t)} K_g(T')dT' + C_h(T)\frac{dT_P(t)}{dt} \tag{3.5}$$

$$C_h(T)\frac{dT_P(t)}{dt} = P(t) - K_W(T_P(t) - T_0) - K_g(T_P(t) - T_s(t)) \tag{3.6}$$

$$C_s(T)\frac{dT_s(t)}{dt} = \ K_g(T_P(t) - T_s(t)) \tag{3.7}$$

where K_g is the thermal conductance between the two due to the grease, and T_0 is the temperature of the heat bath. The respective temperatures of the platform and sample are given by $T_P(t)$ and $T_s(t)$, respectively.

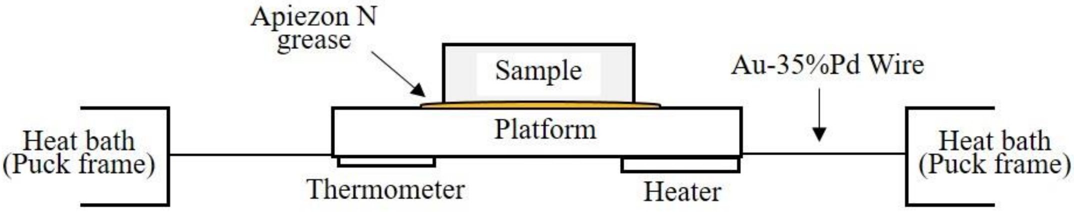

Figure. 3.1: Thermal connections to the sample and platform in PPMS heat capacity option.

3.2 Measurements of electrical resistivity and magnetization under hydrostatic pressures

3.2.1 Electrical resistivity and magnetoresistance

The electrical resistivity was measured from 0.6 to 80 K, and the magnetoresistance was measured in magnetic fields up to 9.5 T at 2 K using an ac four-terminal method by an ac resistance bridge (LR-700, LINER RESEARCH INC.). Hydrostatic pressures were generated by a clamp-type piston-cylinder pressure cells made of NiCrAl and Cu-Be. Daphne oil 7373 was used as the pressure transmitting medium. The pressure cell was screwed to the ^{3}He pot of the Heliox refrigerator (Oxford Instrum. Inc.), which was inserted in a 10 T superconducting magnet (Oxford Instrum. Inc.). The pressure was determined by measuring the superconducting transition in the ac susceptibility of a piece of tin [91].

3.2.2 Magnetization

For the susceptibility measurement, hydrostatic pressures up to 1.56 GPa were applied on a sample of $CeRu_2Al_{10}$ using a piston-cylinder pressure cell of 8.5 mm in diameter made of NiCrAl alloy shown in Fig. 3.2. Daphne oil 7373 was used as the pressure transmitting medium. The pressure cell was inserted to a commercial SQUID magnetometer (MPMS, Quantum Design Inc.). The temperature dependence of magnetization $M(T)$ was measured in an external field B =1 T from 2 to 300 K. The pressure was determined by measuring the superconducting transition in the dc- susceptibility of a piece of tin [91].

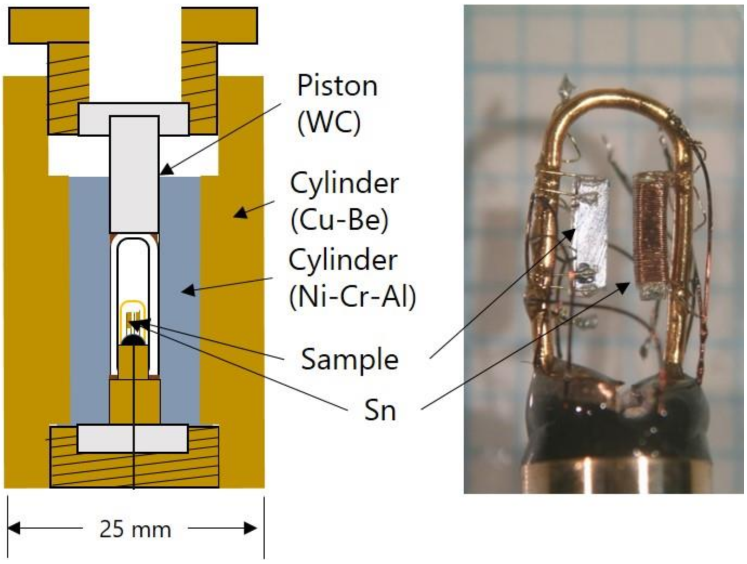

Figure 3.1: (left) Cross-sectional view of the piston-cylinder-type high pressure cell. (right) A photo of the sample and Sn manometer set for resistivity measurements.

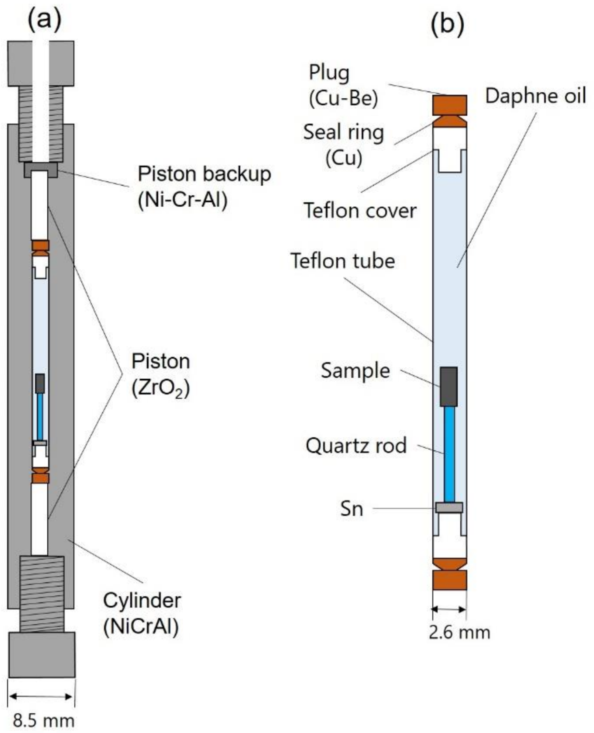

Figure 3.2: (a) Cross-sectional view of the piston-cylinder-type high pressure cell for the susceptibility measurement. (b) Expand sectional view of the part in the inside of cylinder of (a).

3.3 Measurements of lattice strain, magnetization, specific heat under uniaxial pressures

3.3.1 Lattice strain

The strain of single crystalline samples was measured by the strain gauge method at room temperature under uniaxial pressures up to 0.25 GPa. Fig. 3.3 is the pressure cell for the strain measurement. The sample was sandwiched between two Teflon sheet. A pair of pistons was made of tungsten carbide (WC) with diameter of 6 mm. The relative change in length $\Delta L/L$ can be detected electrically by using the relationship $\Delta R/R = K_s \Delta L/L$, where $\Delta R/R$ is the relative change in the electrical resistance R of the strain gauge and $K_s = 1.98$ is the gauge factor. Strain gauges (KFR-02N-120-C1-16N10C2, Kyowa Electronic Institute Inc.) were glued on the surfaces of a rectangular sample of $2 \times 2 \times 2$ mm^3 using the cyanoacrylate-based adhesive (Aron Alpha, Toagosei). The pressure dependence of R was measured by means of an ac-Wheatstone-bridge (DPM-601A, Kyowa Electronic Institute Inc.). The data at pressures above 0.05 GPa were reproducible in the measurements with increasing and decreasing pressures.

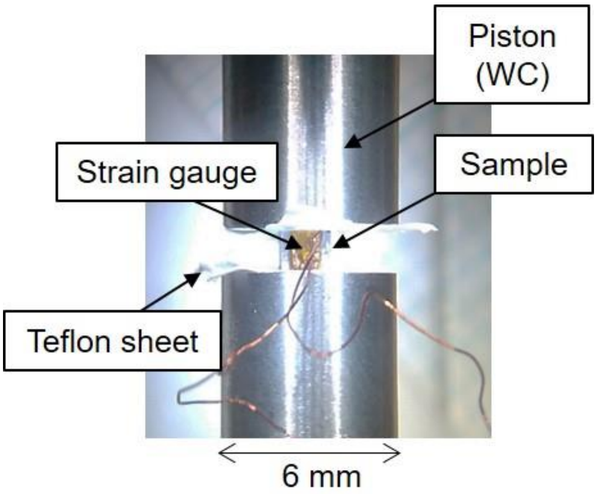

Figure 3.3: A photo of the pressure cell for the strain measurement.

3.3.2 Magnetization

For the susceptibility measurement, uniaxial pressures up to 0.97 GPa were applied on a sample plate of 0.5–0.8 mm in thickness by a homemade pressure cell made of non-magnetic composite ceramic (FCY20A, Fuji die Co. Ltd). The composite ceramic is a mixture of Y_2O_3-partially stabilized ZrO_2 and Al_2O_3 synthesized under high temperature and pressure. Depending on the configurations $P//B$ and $P\perp B$, two type of pressure cells of 8.8 mm in diameter shown in Fig 3.4 were inserted to a commercial SQUID magnetometer (MPMS, Quantum Design Inc.). The cylinder, and the upper and lower nuts of the pressure cells are made of Cu-Be alloy. To observe the spin-flop transition, the magnetization processes $M(B)$ in $B//c$ up to 5 T were measured at 2 K. The range of magnetic field for $M(B)$ measurements was extended up to 9.5 T using a high-resolution capacitive magnetometer equipped with a pressure cell [92]. The load-sensing device for the uniaxial pressure cell shown in Fig. 3.5 and Fig. 3.6 is screwed to the ^{3}He pot of the Heliox refrigerator (Oxford Instrum. Inc.). The pressure was determined by measuring the superconducting transition in the dc susceptibility of a piece of tin placed at the end of the pressure cell [89] by using the SQUID magnetometer (MPMS, Quantum Design Inc.). The magnetizations of the sample at 5 T and 9.5 T are, respectively, about 4% and −50% of those of the pressure cell containing the sample as shown in Fig. 3.7.

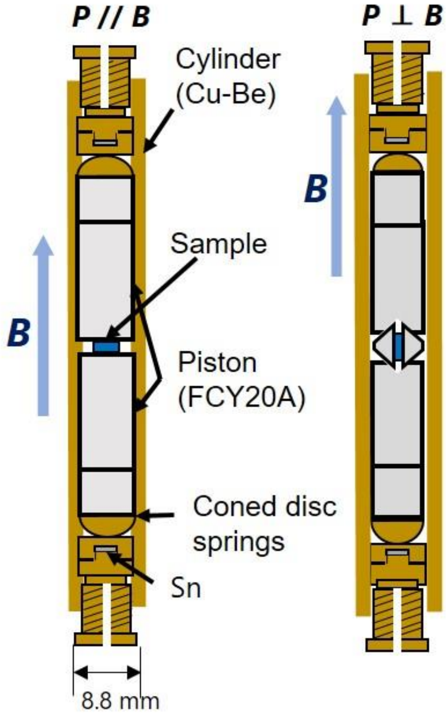

Figure 3.4: Cross sectional view of the piston cylinder cell for the measurement of magnetization under uniaxial pressures for $P//B$ (left) and $P\perp B$ (right).

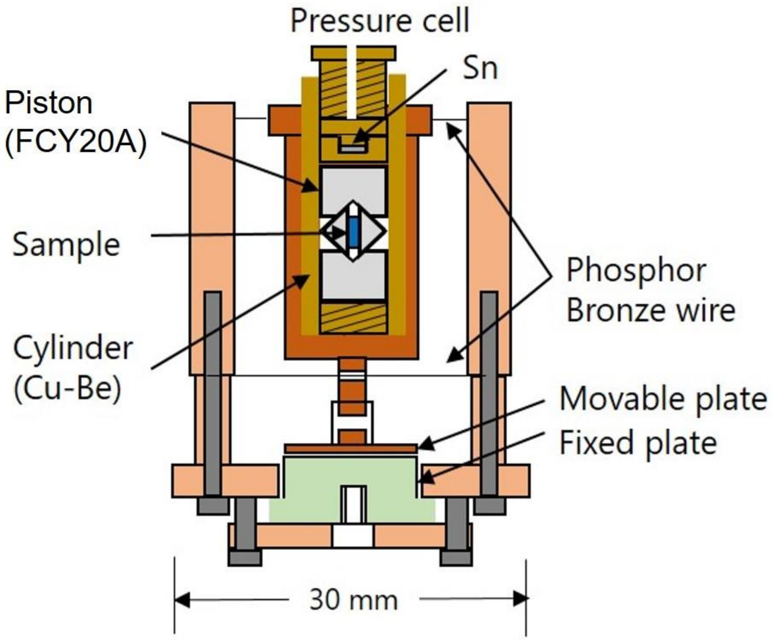

Figure 3.5: Cross sectional view of the load-sensing device for the capacitive magnetometer for uniaxial pressure cell. The sample is sandwiched by pistons, which apply uniaxial pressure $P\perp B$.

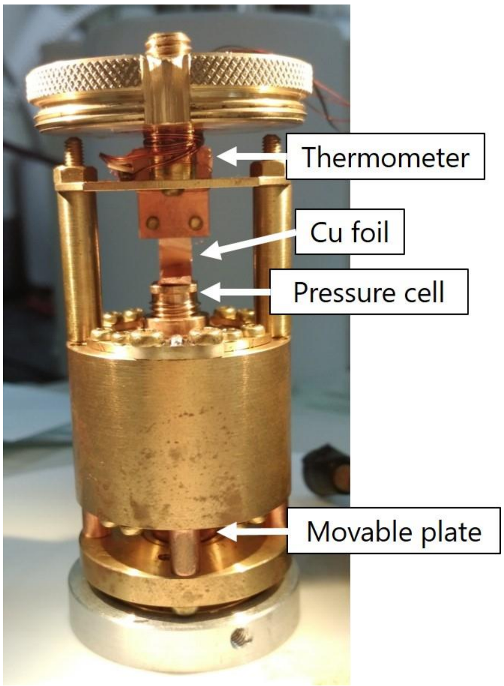

Figure 3.6: The load-sensing device for the capacitive magnetometer for pressure cell.

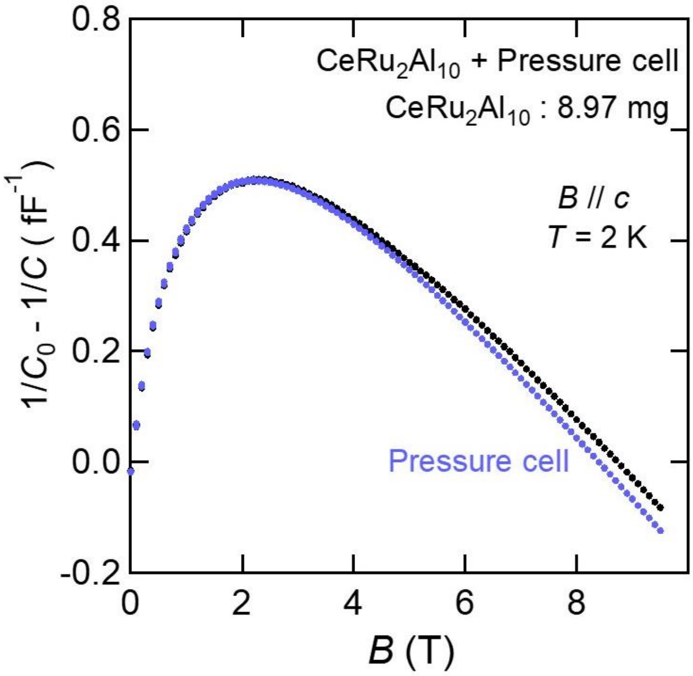

Figure 3.7: Magnetic field dependence of the signals of capacitance for $CeRu_2Al_{10}$ sample and pressure cell and that without the sample.

3.3.3 Specific heat

The specific heat under uniaxial pressures up to 0.45 GPa was measured by using an ac calorimeter in the temperature range 1.6–40 K [93]. The uniaxial pressure cell is shown in Fig. 3.8. We used disk-shaped samples of 2 mm in diameter and 0.2 mm in thickness. The sample was sandwiched between two Cu-Be plates, on which a thermometer and a heater were mounted, respectively. A pair of pistons was made of ZrO_2 with a rather low thermal conductivity. To achieve better thermal isolation, diamond powder was placed between the Cu-Be and piston. The pressure was determined by the pressure dependence of superconducting transition temperature of a piece of indium [94].

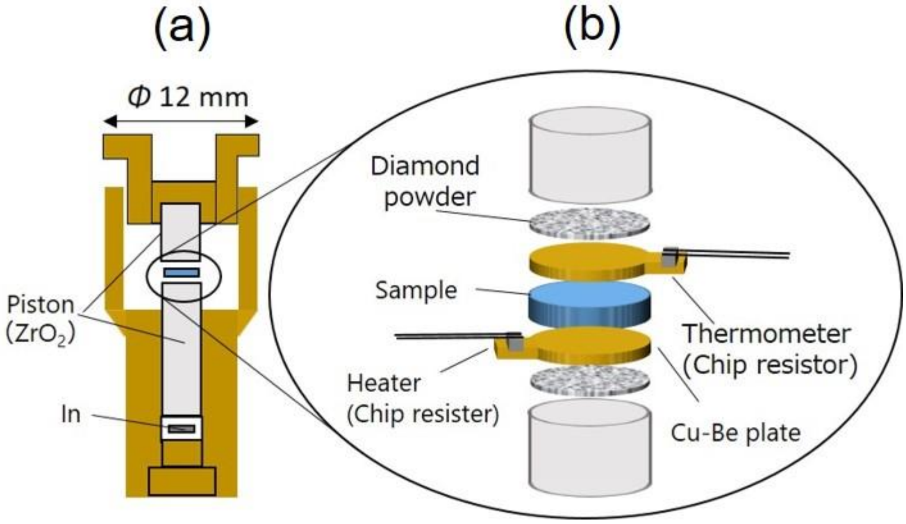

Figure 3.8: (a) Cross section of the uniaxial pressure cell for ac calorimetric measurements. (b) An expanded sectional view of the part in the circle of (a).

Chapter 4

Results and discussion

4.1 Magnetic, transport, and thermal properties of $CeRu_2Al_{10}$ doped with 3*p* electrons

Magnetic susceptibility

Figs. 4.1 (a) and (b), respectively, show the temperature dependences of the magnetic susceptibility $\chi(T)$ and its inverse $1/\chi$ for $CeRu_2Al_{10-y}Si_y$. At temperatures below 50 K, χ increases with increasing y. Above 100 K, the dependences of $1/\chi$ for all samples follow the Curie-Weiss law. A least square fit to the data with the Curie-Weiss form yielded the effective magnetic moment μ_{eff} and paramagnetic Curie temperature θ_{P}. With increasing y from 0 to 0.38, μ_{eff} decreases from 2.6 to 2.4μ_{B}/Ce and $|\theta_{\mathrm{P}}|$ decreases from 100 K to 13 K. Decrease in both μ_{eff} and $|\theta_{\mathrm{P}}|$ for $CeRu_2Al_{10-y}Si_y$ indicates that the Si substitution suppresses the *c*-*f* hybridization leading to the localization of the Ce 4*f* electrons. The obtained values for μ_{eff} and $|\theta_{\mathrm{P}}|$ are summarized in Table 4.1. We note here that $|\theta_{\mathrm{P}}|$ for $y \geq 0.3$ is close to T_{N} determined by the specific heat anomaly presented below.

Table. 4.1: Effective magnetic moment μ_{eff}, paramagnetic Curie temperature θ_{P}, and transition temperature T_{N} for polycrystalline samples of $\mathrm{CeRu_2Al_{10-\mathit{y}}Si_{\mathit{y}}}$. The data for x = 0 are taken from the previous polycrystalline study [48].

y	μ_{eff} (μ_{B})	θ_{P} (K)	T_{N} (K)
0	2.6	−100	27
0.2	2.44	−44	20.5
0.3	2.40	−18	16.5
0.38	2.43	−13	12

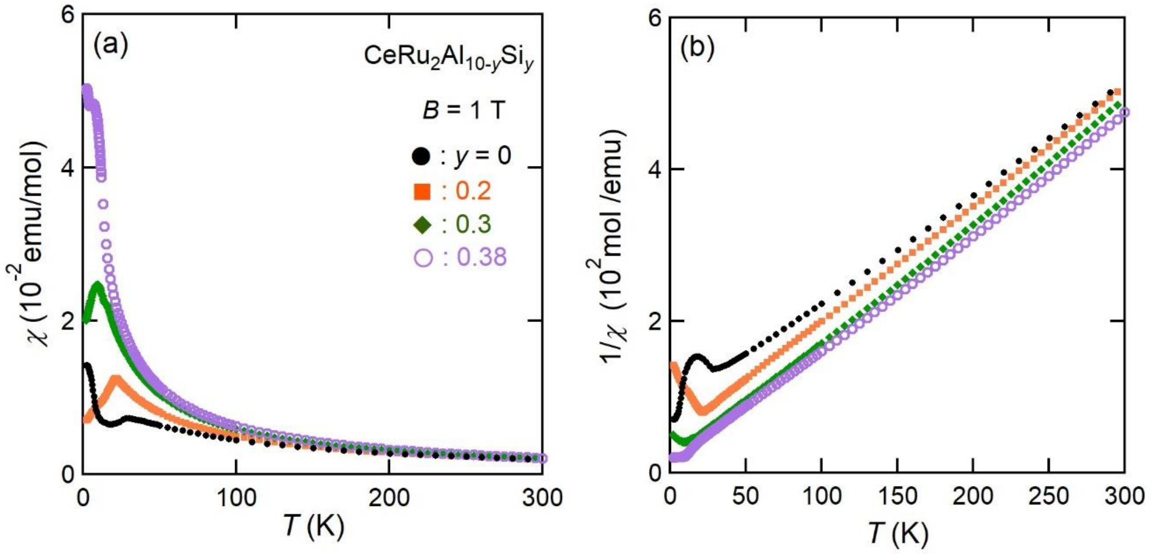

Figure 4.1: Temperature dependence of (a) the magnetic susceptibility χ and (b) the inverse $1/\chi$ for $\mathrm{CeRu_2Al_{10-\mathit{y}}Si_{\mathit{y}}}$.

Electrical resistivity

Fig 4.2 shows the temperature dependence of $\rho(T)$ for $CeRu_2Al_{10-y}Si_y$ whose values were normalized by the value at 300 K. The $\rho(T)$ curves for $y \leq 0.2$ show a thermal activation behavior, $\rho \propto \exp(\Delta/2k_BT)$, where Δ is the activation energy. The fits to the data are drawn by the dashed curves in Fig. 2. The value of $\Delta/2k_B$ strongly decreases from 40 K for $y = 0$ to 14 K for $y = 0.2$. This suppression of Δ is consistent with that found in the single crystal with $y = 0.1$ [79]. For $y = 0.3$, $\rho(T)$ above T_N does not follow the activation-type form but obeys $-\log T$ dependence. This means that the hybridization gap disappears for $y \geq 0.3$ in $CeRu_2Al_{10-y}Si_y$. The disappearance of the activation behavior in $\rho(T)$ by alloying was also reported in $Ce(Ru_{1-x}Rh_x)_2Al_{10}$ at $x \geq 0.23$ [75]. The jump in $\rho(T)$ at T_N in $CeRu_2Al_{10}$ was attributed to the sudden decrease in the carrier density by the gap formation associated with the AFM order. Such a jump in $\rho(T)$ remains for $y = 0.1$, but disappears for $y = 0.2$, suggesting a change in the AFM structure. The temperature at the maximum of $\rho(T)$ for $y = 0.3$ agrees with T_N determined by the specific heat anomaly. For $y = 0.38$, the hump in $\rho(T)$ at around 130 K can be attributed to the crystal field excitations.

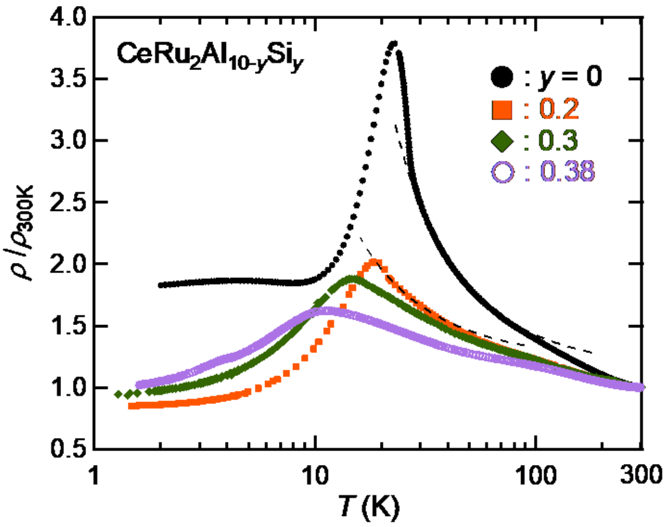

Figure 4.2: Temperature dependence of the electrical resistivity normalized by the value at 300 K ρ/ρ_{300K} for $CeRu_2Al_{10-y}Si_y$. The dashed lines represent the activation-type behavior at $T > 70$ K.

Specific heat

Fig. 4.3(a) shows the results of specific heat divided by temperature C/T for $\mathrm{CeRu_2Al_{10-\mathit{y}}Si_{\mathit{y}}}$. The pronounced jump for all samples is the manifestation of long-ranged AFM ordering. The transition temperature T_{N}, which was taken as the midpoint of the jump in C/T, decreases with increasing y. However, the magnitude of the jump at T_{N} remains unchanged up to $y = 0.38$ despite of the high degree of atomic disorder in the lattice. This fact is consistent with the stabilization of magnetic moments with increasing y due to the weakening of the c-f hybridization as mentioned above. The magnetic entropy $S_{\mathrm{mag}}(T)$ was calculated by the integration of the magnetic specific heat C_{m}/T, in which C_{m} denotes the differential in C between $\mathrm{CeRu_2Al_{10-\mathit{y}}Si_{\mathit{y}}}$ and a nonmagnetic reference $\mathrm{LaRu_2Al_{10}}$. The value of S_{mag} reaches 4 J/Kmol = $0.7R\ln 2$ at T_{N} as shown in Fig. 4.3(b). Similar changes in C_{m} and S_{mag} with substitution were observed in $\mathrm{Ce(Ru_{1-\mathit{x}}Rh_{\mathit{x}})_2Al_{10}}$ for $x \leq 0.34$ [75].

We pay our attention to an additional anomaly in C/T for $y \geq 0.3$. The small hump at 11 K for $y = 0.3$ can be attributed to the magnetic transition of $\mathrm{CeAl_{0.9}Si_{1.1}}$ impurity ($T_{\mathrm{C}} = 11$ K), because the presence of this impurity was detected by the EDX. For $y = 0.38$, in addition to the large increase below 13 K, a sharp anomaly appears at 4.2 K, where $\rho(T)$ also shows a weak anomaly (see Fig. 4.2) and $\chi(T)$ displays an upturn as shown in Fig. 4.1(a). As mentioned in the Section 2, the compound $\mathrm{CeAl_{\mathit{x}}Si_{2-\mathit{x}}}$ has a large homogeneity range $0.45 \leq x \leq 1.28$ in which the ordering temperature changes from $T_{\mathrm{N}} = 4.2$ K for $\mathrm{CeAl_{1.2}Si_{0.8}}$ to $T_{\mathrm{C}} = 11$ K for $\mathrm{CeAl_{0.9}Si_{1.1}}$ [89,90,95]. Therefore, we conjecture that the peak in C/T is not intrinsic to the host phase but is due to the magnetic order of the impurity phase of $\mathrm{CeAl_{1.2}Si_{0.8}}$.

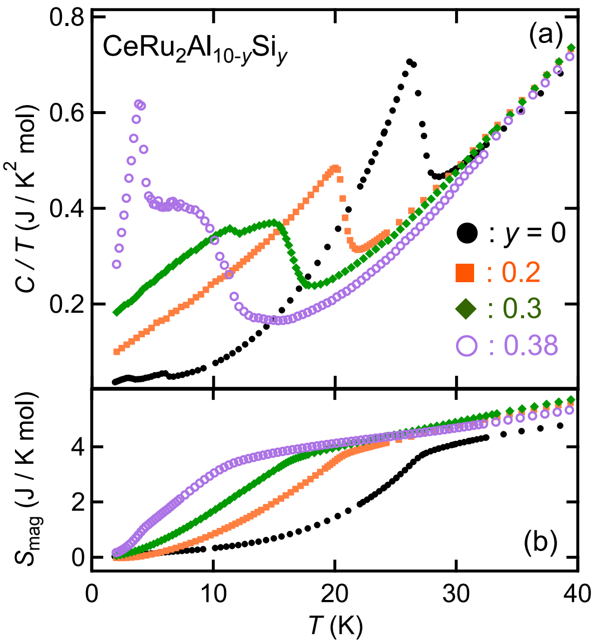

Figure 4.3: Temperature dependences of (a) specific heat divided by temperature C/T and (b) magnetic entropy S_{mag} for CeRu$_2$Al$_{10\text{-}y}$Si$_y$.

Discussion

The variations of the T_N and $|\theta_P|$ for $CeRu_2Al_{10-y}Si_y$ as a function of y are plotted in Fig. 4.4. The data of T_N include that for the single crystal with $y = 0.1$ [79]. Both $|\theta_P|$ and T_N decrease linearly with y. This relation indicates that the depression of T_N is a result of the decrease in T_K, because $|\theta_P|/2$ is a measure of T_K [96]. This observation is opposite to what is expected from the conventional Doniach phase diagram [6], in which the decrease of T_K is accompanied with the enhancement of T_N in the vicinity of the critical region. Our observation is rather consistent with a recent theory dealing with the itinerant-localized transition of the Kondo lattice [8]. The phase diagram of this theory has a certain range of the Kondo interaction where both T_K and T_N decrease.

We notice in Fig. 4.4 that the degree of decrease in T_N for $CeRu_2Al_{10-y}Si_y$ is comparable with that for $Ce(Ru_{1-x}Rh_x)_2Al_{10}$ as a function of doped electron number per formula unit; y and $2x$. There are common features between the two systems. The activation behavior in $\rho(T)$ disappears as y ($2x$) is increased to 0.3 (0.46). The maximum values of $\chi(T)$ approach 5×10^{-2} emu/mol for both $y = 0.38$ and $2x = 0.46$ [75]. These resemblances suggest that the increases of $3p$ and $4d$ electrons in $CeRu_2Al_{10}$ result in the same effects on the physical properties. This argument is consistent with the band structure in which the Ce $4f$ state is hybridized with both Ru $4d$ and Al $3p$ states near the Fermi level [97].

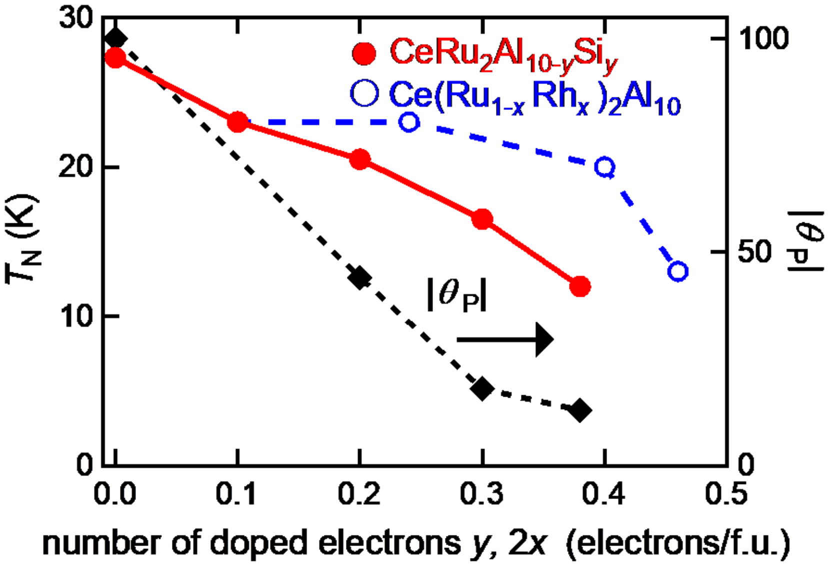

Figure 4.4: Variations of the Néel temperature T_N and absolute value of paramagnetic Curie temperature $|\theta_P|$ as a function of doped electron number per formula unit of $CeRu_2Al_{10-y}Si_y$. The values of T_N for $Ce(Ru_{1-x}Rh_x)_2Al_{10}$ are plotted for comparison [74,75].

4.2 Pressure effects on structural and magnetic properties

4.2.1 $CeFe_2Al_{10}$ under uniaxial pressure

The temperature dependence of magnetic susceptibility $\chi(T)$ of $CeFe_2Al_{10}$ under ambient pressure is shown in Fig. 1.16 (i). The result of $\chi(T)$ is characterized by strong anisotropy $\chi_a(T) > \chi_c(T) > \chi_b(T)$. The temperatures at the maximum $T_{\chi m}$ for χ_a and χ_c are 70 K and 122 K, respectably [53]. Fig. 4.5 shows $\chi_a(T)$, $\chi_c(T)$, and $\chi_b(T)$ under uniaxial pressures applied parallel to the magnetic field. With increasing P to 0.47 GPa, $T_{\chi m}$ increases up to 81 K under $P//a$ and to 140 K under $P//c$. With increasing $P//a$, $\chi_a(T)$ at $T < 10$ K increases but the rise of $\chi_c(T)$ at $T < 10$ K does not depend on $P//c$. On the other hand, $\chi_b(T)$ hardly changes under $P//b$ in the whole temperature range.

Fig. 4.6 shows the plot of C/T vs T^2 for $CeFe_2Al_{10}$ under $P//b$. With pressurizing up to $P = 0.55$ GPa, the values of C/T hardly change in the temperature range 0.6 - 35 K. Accordingly, the electronic specific heat coefficient γ stays at 8 mJ/K^{2}mol. No signs of phase transition appear in $\chi(T)$ and C/T under $P//b$ up to 0.5 GPa.

Here, we consider the reason why $\chi_a(T)$ at $T < 10$ K increased by $P//a$. As described in §1.3.4, $\rho(T)$ of $CeFe_2Al_{10}$ exhibits thermal activation type behavior below 20 K. The activation energy is suppressed by the application of hydrostatic pressure. This pressure effect suggested that the pseudogap is suppressed as the *c*-*f* hybridization is strengthened by hydrostatic pressure. In analogy, the increase of $\chi(T)$ at $T < 10$ K under $P//$a suggests that the pseudogap is suppressed and the electronic density of states at the Fermi level increases.

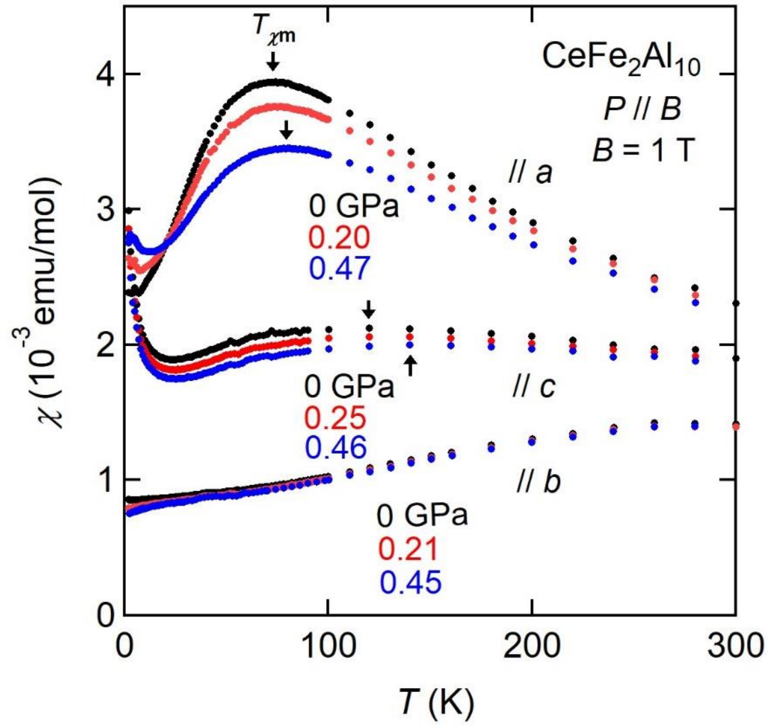

Figure 4.5: Temperature dependence of magnetic susceptibility $\chi(T)$ for CeFe$_2$Al$_{10}$ measured under uniaxial pressures $P//B//a$, $P//B//b$, and $P//B//c$.

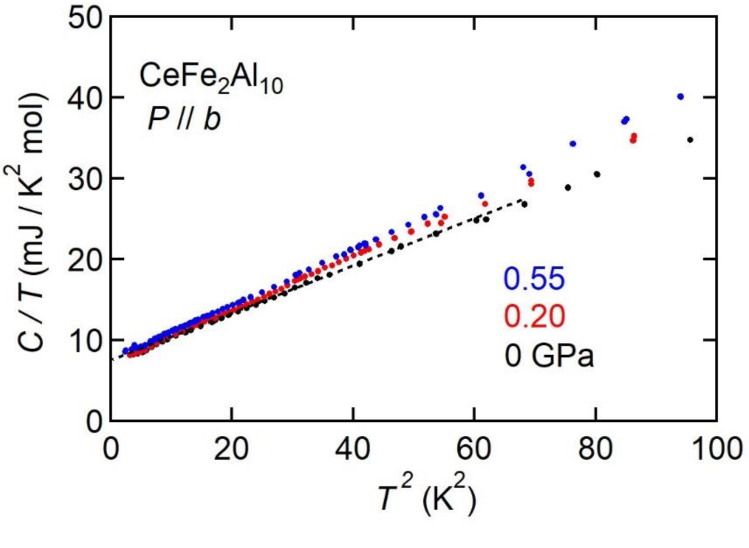

Figure 4.6: Temperature dependence of specific heat C_p of CeFe$_2$Al$_{10}$ under pressures applied along the b axis up to 0.55 GPa.

4.2.2 $CeRu_2Al_{10}$ under hydrostatic pressure

Electrical resistivity and magnetoresistance

Fig. 4.7 and Fig. 4.8 show the temperature dependence of the resistivity $\rho(T)$ for $I//c$ and the longitudinal magnetoresistance $\rho(B)$ at 2 K for $I//B//c$ under various pressures, respectively. With increasing pressure, $\rho(T)$ is increased below 10 K which is consistent with the previous measurement as shown in Fig. 1.30 (c) [81]. However, the magnetoresistance $\rho(B)$ at ambient pressure increases linearly with B and jumps at B = 5 T, which behavior is different from the previous measurement as shown in Fig. 1.33 (a). Previous data was nonlinear and no jump. The midpoint of the jump is 5.2 T which agrees with the spin-flop transition field B^* in $M(B//c)$ as shown in Fig 4.9. With increasing pressure to 1.24 GPa, B^* increases to 9.2 T.

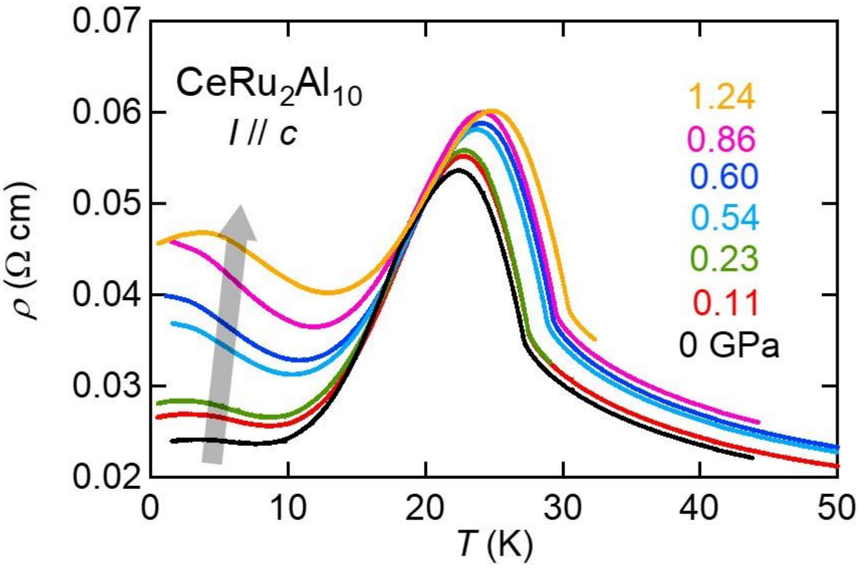

Figure 4.7: Temperature dependence of electrical resistivity ρ of $CeRu_2Al_{10}$ along the c axis under various pressures up to 1.24 GPa.

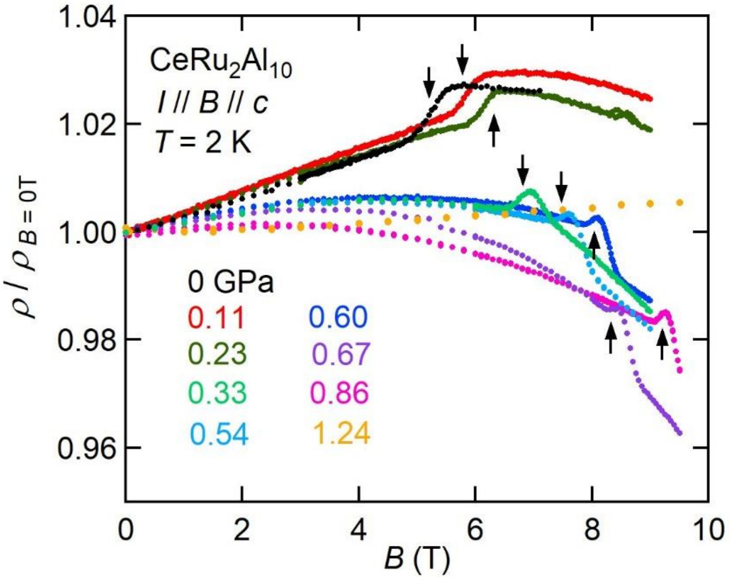

Figure 4.8: Magnetoresistance $\rho(B)$ of CeRu$_2$Al$_{10}$ at 2 K for *I*//*c* and *B*//*c* under various pressures, where vertical scales are normalized by the value at $B = 0$.

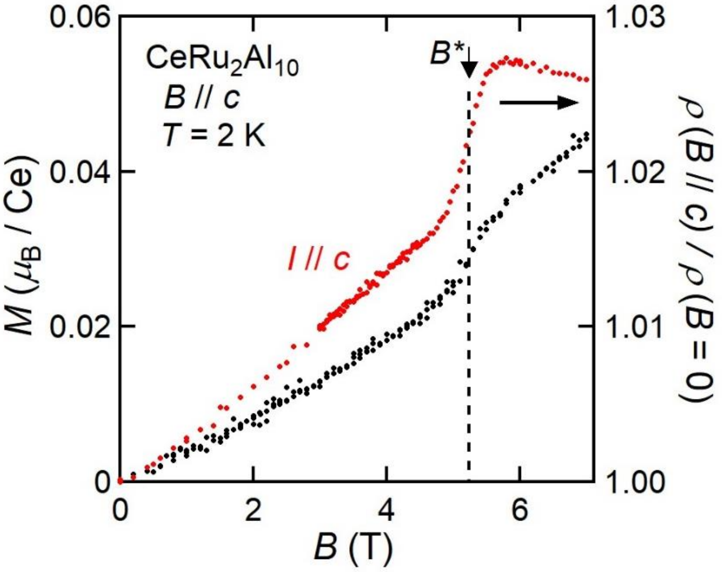

Figure 4.9: Magnetization $M(B//c)$ and magnetoresistance $\rho(B//c)/\rho(B=0)$ for the longitudinal configuration at ambient pressure. The spin flop field B^* taken as the midpoint of the jump in $M(B//c)$ agrees with that in $\rho(B//c)$.

Magnetic susceptibility

Figs. 4.10(a) and 4.10(b) show the temperature dependences of magnetic susceptibility $\chi(T)$ of T = Ru for $B//c$ under various hydrostatic pressures P_h. With increasing pressure, the magnitude of the maximum of $\chi_c(T)$ at 30 K is suppressed and the temperatures at the maximum $T_{\chi m}$ is increased. At P_h = 1.56 GPa, T_N and $T_{\chi m}$ reach 31.5 K and 43.5 K, respectively, which value are higher and comparable with for T = Os at ambient pressure.

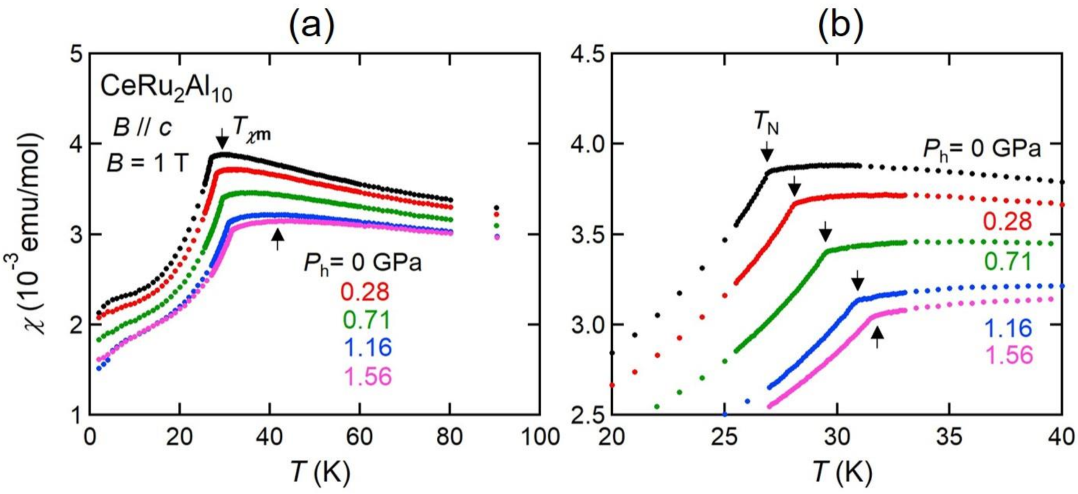

Figure 4.10: (a) Temperature dependence of magnetic susceptibility $\chi(T)$ for $CeRu_2Al_{10}$ measured in $B//c$ under various hydrostatic pressures. (b) The data of $\chi(T)$ near the antiferromagnetic transition temperature T_N.

4.2.3 $CeRu_2Al_{10}$ and $CeOs_2Al_{10}$ under uniaxial pressure

Lattice strain

Fig. 4.11(a) show the uniaxial pressure dependences of the relative length variations $\Delta L/L$ for CeT_2Al_{10} (T = Ru, Os) at room temperature. The slope of the data gives the rate $(1/L_0)dL/dP$ (%/GPa), whose values are listed in Table 4.2 together with the reported data under hydrostatic pressure P_h [85]. The lattice parameters perpendicular to the applied pressure increase through the Poison ratio. For T = Ru, the contraction rate along the pressure $P//b$ is 37% of those for $P//a$ and $P//c$, where the rates for $P//a$ and $P//c$ are similar. The rates for $P//a$ and $P//c$ decrease by 40% on going from T = Ru to T = Os. These relations are consistent with the data obtained under hydrostatic pressure [85] as shown in Table 4.2.

The set of data of $\Delta L/L$ in Fig. 4.11(a) gives the volume contraction under uniaxial pressures shown in Fig. 4.11(b). Under $P//a$ and $P//c$, the contractions in T = Os are smaller than in T = Ru. It is noteworthy that the volume does not decrease under $P//b$ up to 0.5 GPa for both compounds.

Table 4.2: Pressure derivative of the lattice parameters a, b, and c of CeT_2Al_{10} (T = Ru, Os) at room temperature under uniaxial pressures $P//a$, $P//b$, and $P//c$. The data under hydrostatic pressure P_h are taken from Ref. [85].

	P_u (T = Ru)			P_u (T = Os)			P_h (Ref. 85)	
	$P//a$	$P//b$	$P//c$	$P//a$	$P//b$	$P//c$	T = Ru	T = Os
$(1/a_0)da/dP$ (%/GPa)	−0.56	0.15	0.15	−0.32	0.07	0.13	−0.32	−0.29
$(1/b_0)db/dP$ (%/GPa)	0.14	−0.21	0.11	0.08	−0.20	0.16	−0.28	−0.23
$(1/c_0)dc/dP$ (%/GPa)	0.16	0.08	−0.58	0.09	0.12	−0.39	−0.35	−0.30

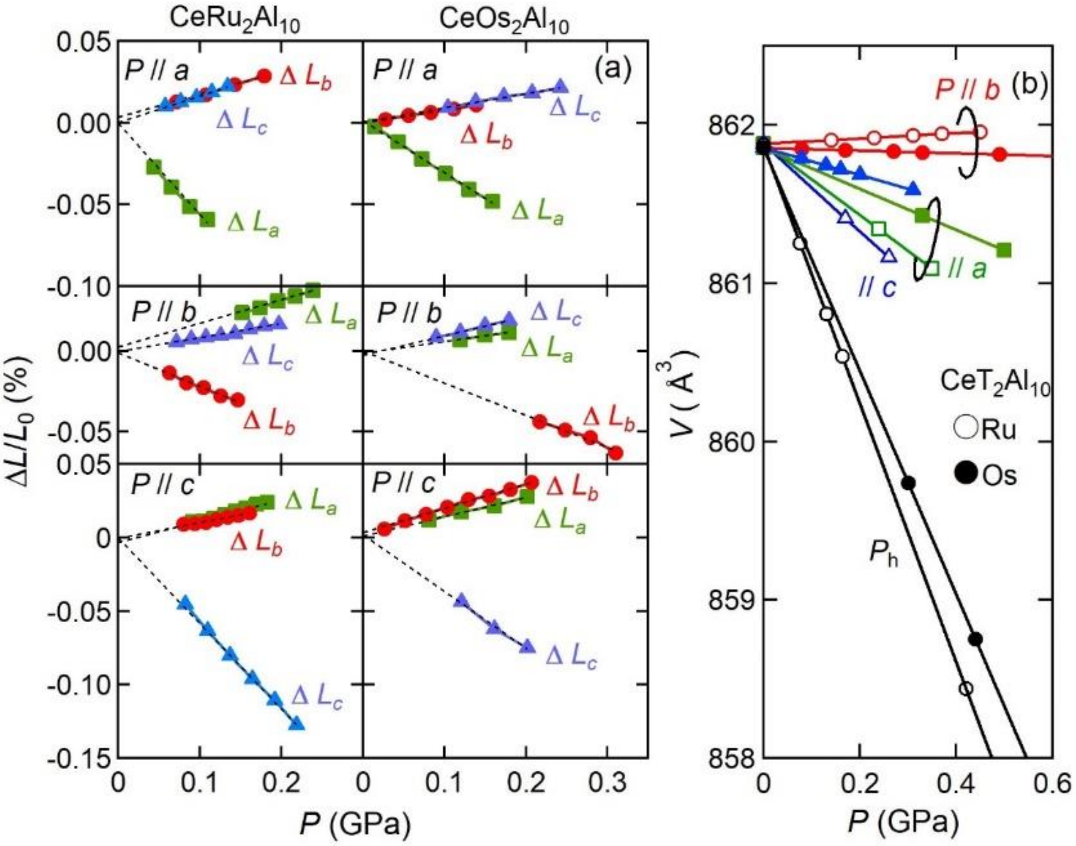

Figure 4.11: (a) Variations of the relative change in the length of single crystals of CeT_2Al$_{10}$ (T = Ru, Os) along the three principal axes as functions of uniaxial pressures at room temperature. (b) Variations of unit-cell volume under uniaxial pressures, which are compared with the data under hydrostatic pressure in Ref. [85].

Magnetic susceptibility and specific heat

Fig. 4.12 shows the temperature dependences of magnetic susceptibility $\chi(T)$ for CeT_2Al$_{10}$ (T = Ru, Os) under uniaxial pressures applied parallel and perpendicular to the external field B. There are maxima in $\chi(T)$ for $B//a$ and $B//c$ at $T_{\chi m}$ as indicated by arrows. Under $P//a$ and $P//c$, $T_{\chi m}$ shifts to high temperatures and the magnitude of $\chi(T_{\chi m})$ decreases in both compounds. On the other hand, neither $T_{\chi m}$ nor $\chi(T_{\chi m})$ changes under $P//b$, indicating very weak effect of $P//b$ on the *c*-*f* hybridization. The data of $\chi(T)$ in the range 25−35 K are replotted in Fig. 4.13 to show up the variation of T_N, which is taken as the temperature where the two lines from above and below the kink intersect. Upon application of $P//a$ up to 0.5 GPa, T_N for T = Ru increases by 1.5 K whereas T_N for T = Os decreases by 0.7 K. Under $P//c$, however, the change in T_N for the two compounds is less than 0.1 K. By contrast, application of $P//b$ enhances T_N by 1.2−1.5 K. A similar degree of increase in T_N is observed in the specific heat C divided by temperature, as shown in Fig. 4.14. Thereby, broadening of the jump in C/T may be caused by inhomogeneous pressure within the sample plate from the center to the edge. Using the data in Figs. 4.12–4.14, we have derived the pressure dependences of $T_{\chi m}$ and T_N as shown in Fig. 4.15. It is worthy to note that all data of $T_{\chi m}$ in $B//a$ and $B//c$ do not change under $P//b$ but T_N under $P//b$ increases significantly for both compounds.

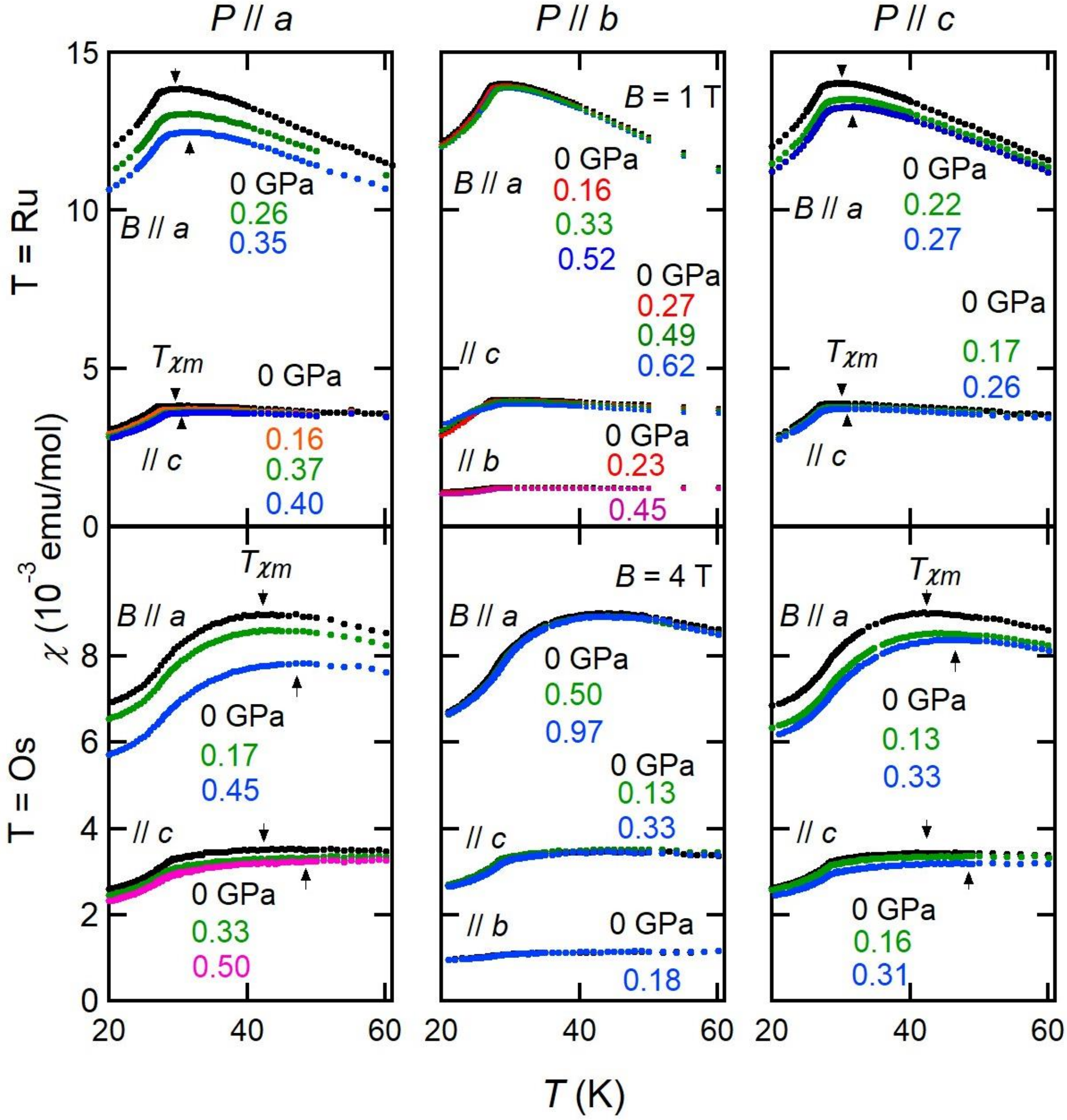

Figure 4.12: Temperature dependence of magnetic susceptibility $\chi(T)$ for CeT_2Al$_{10}$ (T = Ru, Os) measured in magnetic fields $B//a$, $B//b$, and $B//c$ under uniaxial pressures $P//a$, $P//b$, and $P//c$.

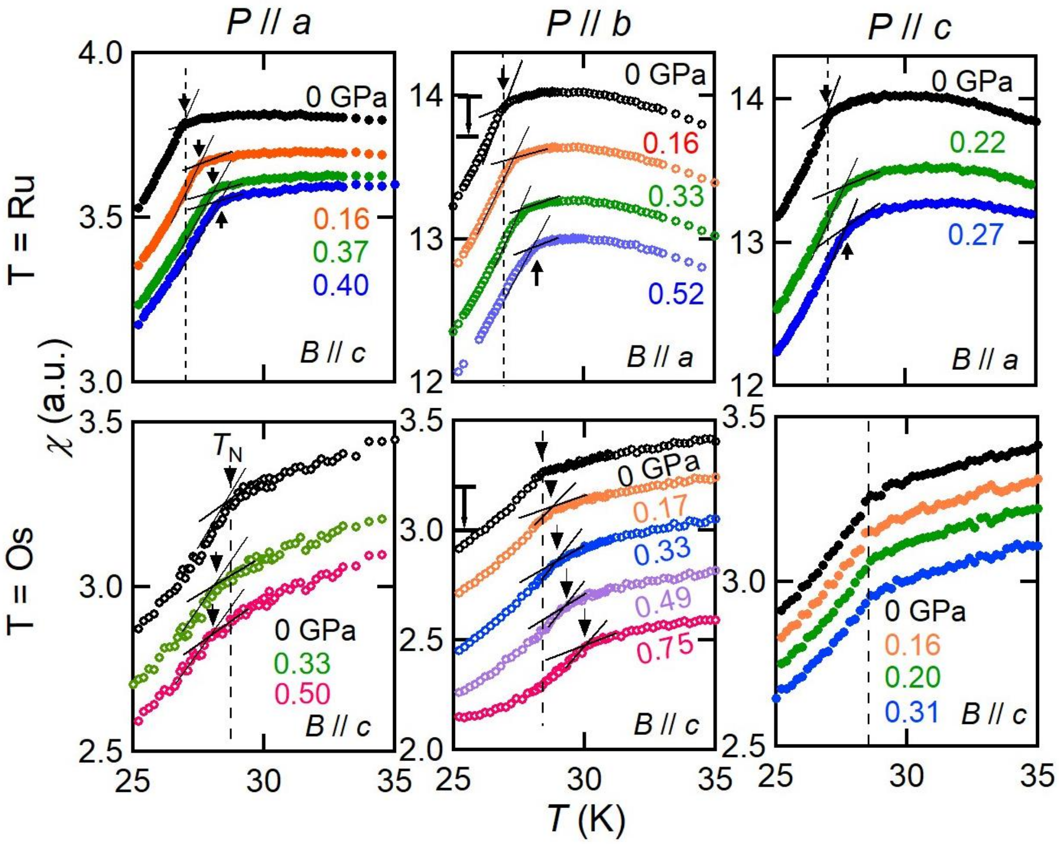

Figure 4.13: Magnetic susceptibility $\chi(T)$ for CeT_2Al$_{10}$ (T = Ru, Os) under uniaxial pressures near the antiferromagnetic transition. The ordering temperature T_N is taken as the intersection of the two lines above and below T_N. For the data only under $P//b$, a suitable offset is added for clarity.

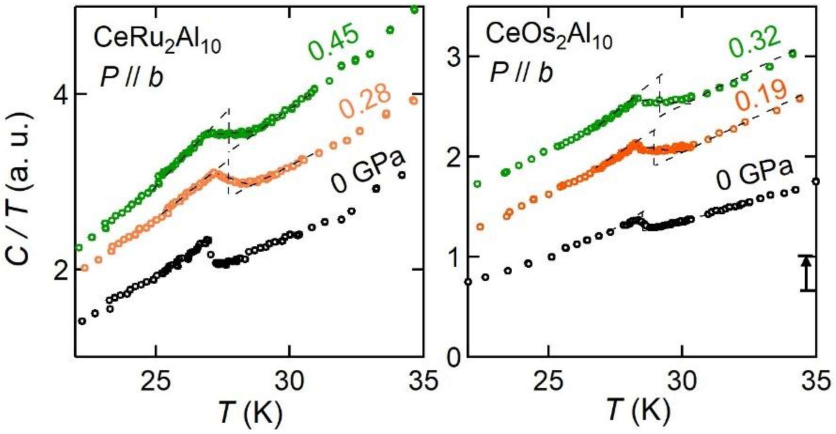

Figure 4.14: Temperature dependence of specific heat divided by temperature C/T for CeT_2Al$_{10}$ (T = Ru, Os) under uniaxial pressures applied along the b axis. The data for T = Os at $P//b$ = 0.32 GPa are offset for clarity. The midpoint of the jump in C/T is taken as T_N.

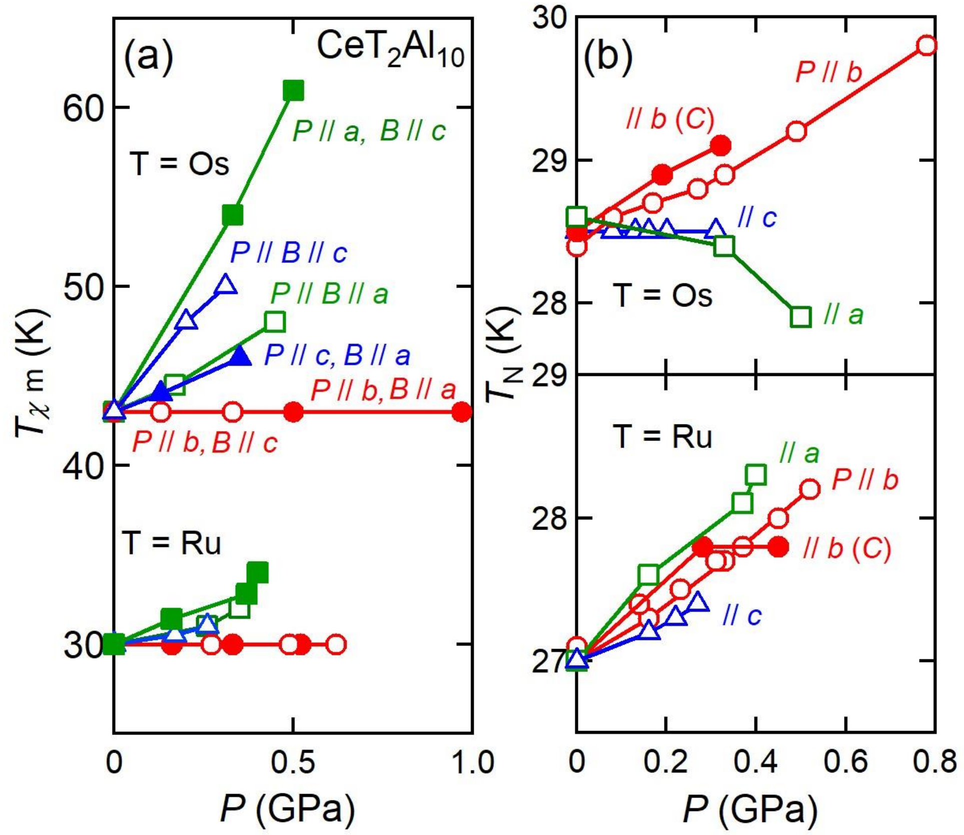

Figure 4.15: Pressure dependences of (a) the maximum temperature in the magnetic susceptibility $T\chi m$ and (b) the antiferromagnetic ordering temperature T_N for CeT_2Al$_{10}$ (T = Ru, Os). Open symbols in (b) show T_N determined by the susceptibility data $\chi(T)$ presented in Fig. 4.13, whereas the closed circles show those determined from the specific heat data C/T presented in Fig. 4.14.

Magnetization

To study the effect of uniaxial pressure on the spin reorientation, we have measured $M(B//c)$ under uniaxial pressures. The magnitude of B^* increases as $P//a$ is applied while B^* does not change for $P//c$ up to 0.27 GPa. However, B^* decreases to 2.6 T as $P//b$ is increased to 0.62 GPa. This suppression of B^* under $P//b$ suggests that the difference in the total energy between the two AFM states with $\mu_{\mathrm{AFM}}//c$ and $\mu_{\mathrm{AFM}}//b$ is diminished probably by the deformation in the rhombus shown in Fig. 4.17(b). It is expected that the rhombus changes to a square under $P//b$ by the increase in θ and changes the rhombus to a square. Here, we recall that the AFM state with $\mu_{\mathrm{AFM}}//b$ is stabilized even in zero field by the substitution of La for Ce in $\mathrm{Ce}_{1-x}\mathrm{La}_x\mathrm{Ru}_2\mathrm{Al}_{10}$ at a low concentration $x = 0.1$ [86,87]. As in the case of application of $P//b$, the angle θ is found to be increased by the La substitution. Furthermore, the direction of μ_{AFM} for $x = 0.1$ changes from $//b$ to $//c$ under a weak hydrostatic pressure of 0.3 GPa, while retaining T_{N} as high as under zero pressure [86,87]. This fact suggests that the mechanism for the high T_{N} is different from that for orienting μ_{AFM} to the c direction.

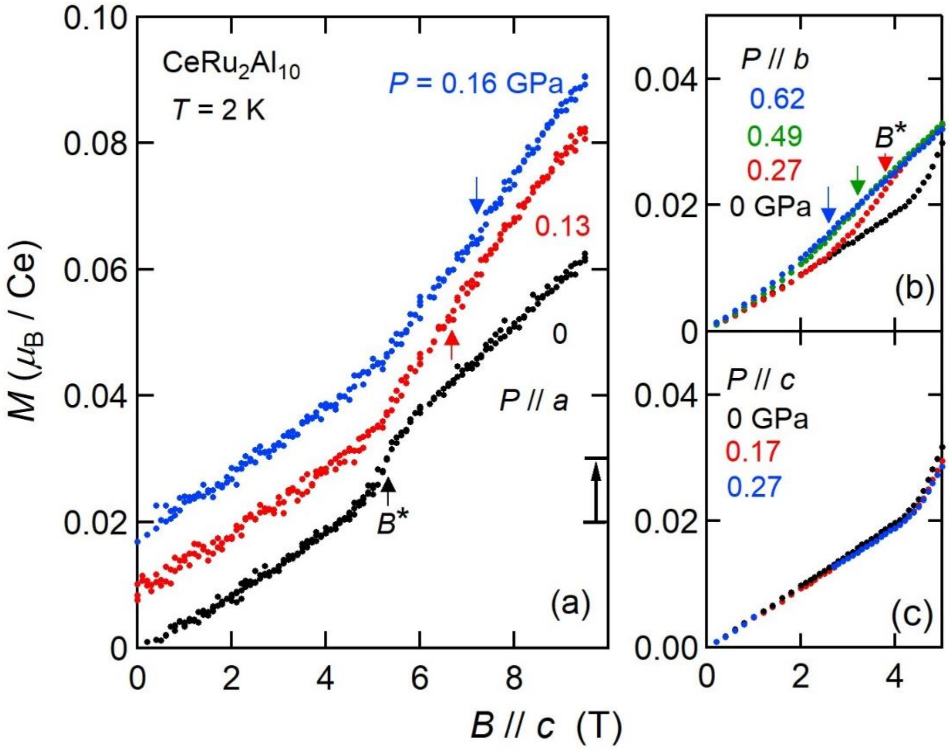

Figure 4.16. Isothermal magnetization curves $M(B//c)$ at 2 K for $CeRu_2Al_{10}$ under uniaxial pressures (a) $P//a$, (b) $P//b$, and (c) $P//c$. The data for $P//a$ are offset for clarity.

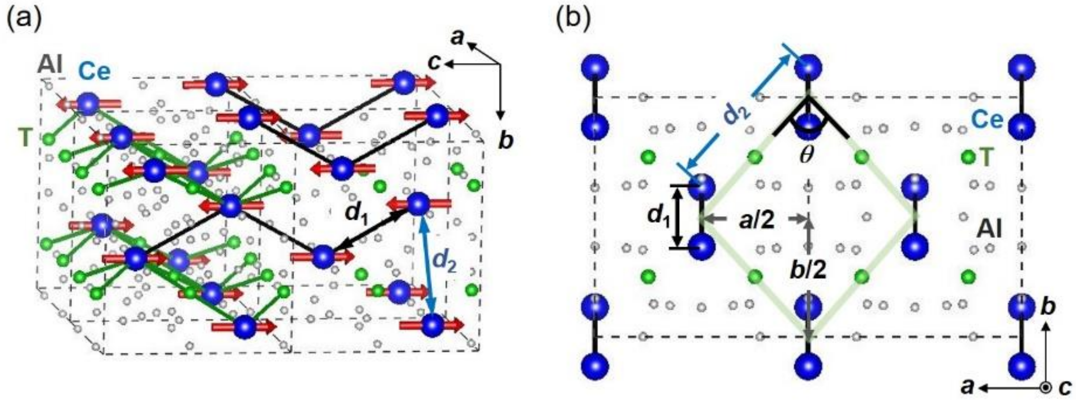

Figure 4.17: (a) Crystal structure and antiferromagnetic structure of CeT_2Al_{10} (T = Ru, Os) [43-50, 52,54,62]. The first- and second-nearest-neighbor Ce-Ce distances d_1 and d_2 are drawn by arrows. (b) The rhombic arrangement of Ce-Ce chains viewed from the c direction, in which the angle θ is 83 deg. for T = Ru and Os at room temperature and ambient pressure.

Discussion

Dependence of T_N on $T_{\chi m}$

Fig. 4.18 shows the variations of T_N for CeT_2Al$_{10}$ as a function of $T_{\chi m}$ under hydrostatic and uniaxial pressure. It should be recalled that $T_{\chi m}$ is a measure of T_K as $T_K \simeq 3T_{\chi m}$, and T_K is a function of the *c-f* hybridization strength (eq. 1.7). The data of T_N under *P*//*a* and *P*//*c* are smoothly connected for the two compounds with a broad maximum. This variation of T_N could be understood by assuming that the *c-f* hybridization governs the T_N. Under *P*//*b*, T_N of both compounds significantly increases without any change in $T_{\chi m}$. This observation is at variance with the model that *c-f* hybridization governs the T_N in these Kondo semiconductors.

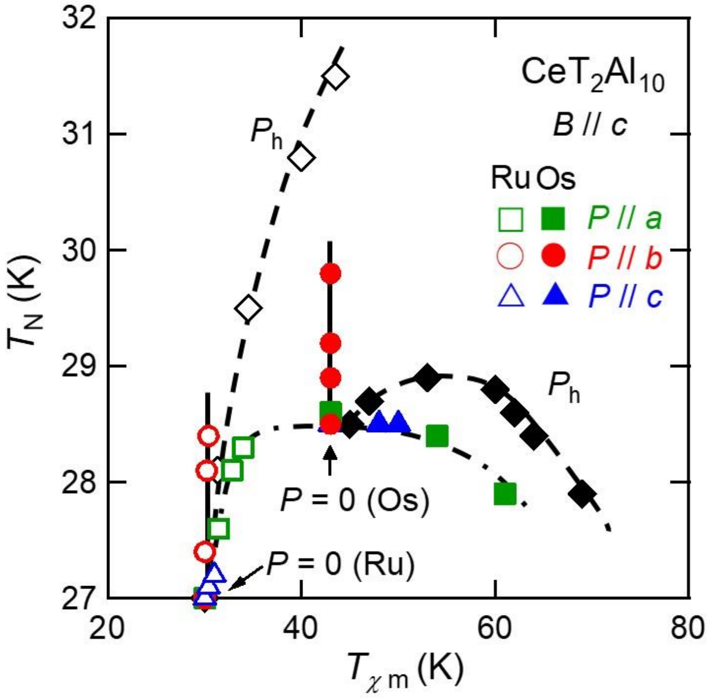

Figure 4.18: Variations of T_N for CeT_2Al$_{10}$ (T = Ru, Os) as a function of $T_{\chi m}$ under uniaxial and hydrostatic pressures.

Dependence of T_N on the lattice parameters

For understanding the unexpected dependence of T_N on $T_{\chi m}$ in Fig. 4, we plot the data of T_N as a function of the lattice parameters in Fig. 4.18. Thereby, the lattice parameters under pressures were derived from the relative change in the length along the principal axes shown in Fig. 4.11(a). It is noteworthy that the variations of T_N as functions of a and c parameters are largely different between hydrostatic pressure and uniaxial pressure. However, as a function of the b-axis parameter, the data of T_N for T = Ru are linearly increased and smoothly connected with those for T = Os. This relation holds even for both hydrostatic pressure P_h and uniaxial pressure $P//b$, although the a- and c-axis parameters decrease under P_h but increase under $P//b$. These results strongly indicate that T_N is enhanced as the b-axis parameter is decreased by a geometrical reason. Under $P//a$ and $P//c$, the b-axis parameter increases as shown in Fig. 4.11(a). Thereby, we expect a decrease in T_N but it is not the case for T = Ru under $P//a$. To understand this discrepancy, it is necessary to examine the possible shift of the atomic coordinate of the Ce atom at the 4c site (0 0.124, 1/4) [45] by x-ray diffraction measurements under uniaxial pressures.

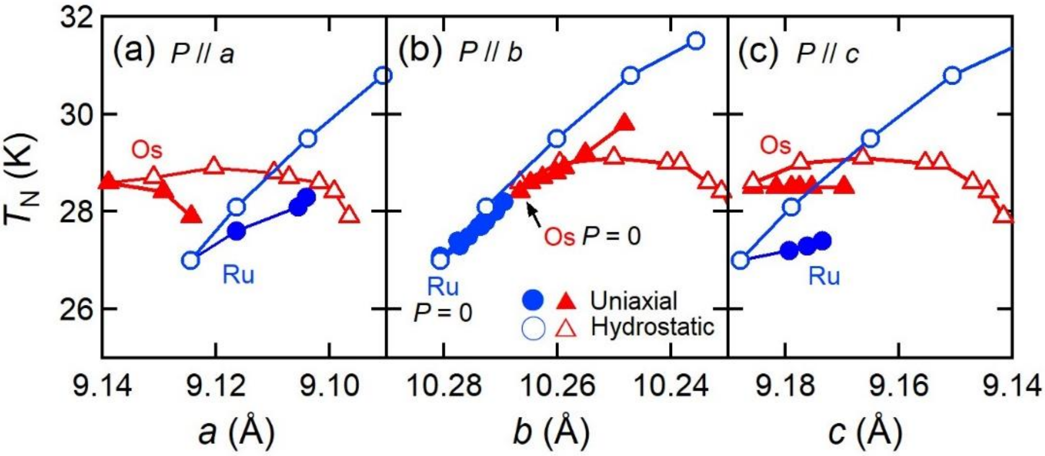

Figure 4.19: Variations of T_N for CeT_2Al$_{10}$ (T = Ru, Os) under uniaxial and hydrostatic pressures as functions of the orthorhombic lattice parameters a, b, and c.

Spin flop transitions

Pressure dependences of the spin flop field B^* for $CeRu_2Al_{10}$ are shown in Fig. 4.19(a). With applying hydrostatic pressure P_h, $B^*(P_h)$ increases linearly, whereas $B^*(P//a)$ and $B^*(P//b)$ change in opposite directions. The opposite changes suggest that B^* depends on the ratio of lattice parameters b/a. Therefore, the data of B^* are plotted as a function of b/a in Fig. 4.19 (b), where the slope of B^* vs b/a for P_h is much steeper than those for $P//a$ and $P//b$. We have searched for an additional geometrical parameter to better describe all the data of B^* including the data under P_h. As a result, we found that all data of B^* fall on a line as a function of $(1/d_2)\times(b/a)$, as shown in Fig. 4.19(c). Here, d_2 is the second-nearest-neighbor Ce-Ce distance that is the distance between the zigzag chains as marked in Figs. 4.17(a) and 4.17(b). We recall that d_2 decreases under P_h but b/a hardly changes under the condition $\Delta a/a_0 \simeq 1.2\Delta b/b_0$ [85]. When d_2 is decreased, the inter-chain interaction should be strengthened so that the AFM state with $\mu_{AFM}//c$ is more stabilized. As a result, B^* is increased under P_h. On the other hand, application of $P//b$ should transform the rhombic arrangement of the zigzag chains closer to a regular tetragonal arrangement with increasing θ from 83 deg to close to 90 deg. This transformation may destabilize the AFM state with $\mu_{AFM}//c$, leading to the decrease of B^* under $P//b$. In other words, the antiferromagnetic inter-chain interaction in the rhombic arrangement realizes the unusual AFM state with $\mu_{AFM}//c$.

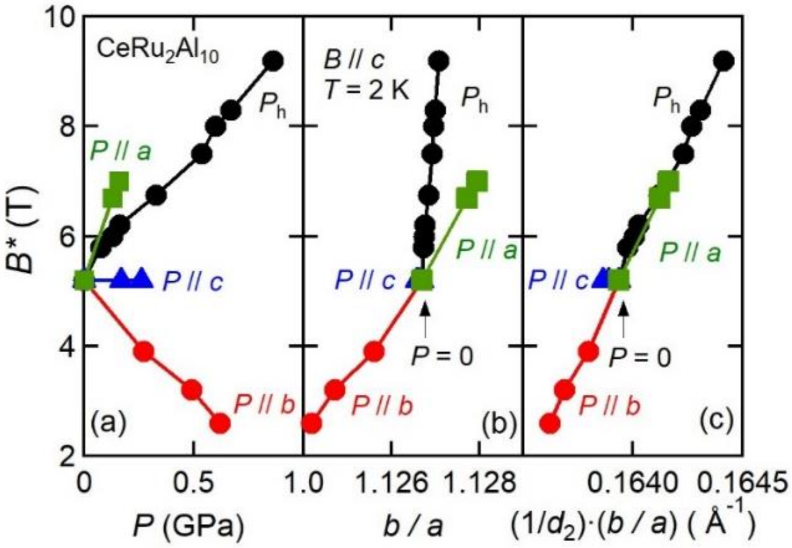

Figure 4.20: Spin flop field B^* for CeRu$_2$Al$_{10}$ under hydrostatic pressure P_h and uniaxial pressures $P//a$, $P//b$, and $P//c$ as functions of (a) applied pressure, (b) the ratio of lattice parameters b/a, and (c) $(1/d_2)\cdot(b/a)$, where d_2 is the interchain distance shown in Fig.4.17.

Chapter 5

Summary

The present study aimed to clarify the relation between the anisotropic *c*-*f* hybridization and unusual AFM order in the Kondo semiconductors CeT_2Al$_{10}$ (T = Ru and Os). First, we have investigated the effect of 3*p* electron doping on the physical properties of CeRu$_2$Al$_{10}$. On polycrystalline samples of CeRu$_2$Al$_{10-y}$Si$_y$ ($y \leq 0.38$), we have measured the magnetic susceptibility χ, electrical resistivity ρ, and specific heat C. Second, in order to control the *c*-*f* hybridization, we have applied uniaxial pressure on the single crystals of CeT_2Al$_{10}$ (T = Ru and Os). We have measured the strains at room temperature and the magnetization and specific heat at low temperatures.

In CeRu$_2$Al$_{10-y}$Si$_y$, the strong decrease in $|\theta_{\rm P}|$ with increasing y suggests the weakening of the *c*-*f* hybridization. The activation-type behavior in $\rho(T)$ at $T_{\rm N} < T$ is also suppressed with increasing y and disappears at $y \geq 0.3$. The variations of $\rho(T)$ and $C(T)$ as well as $T_{\rm N}$ for CeRu$_2$Al$_{10-y}$Si$_y$ as a function of y are quantitatively comparable with those for Ce(Ru$_{1-x}$Rh$_x$)$_2$Al$_{10}$ as a function of 2x. This fact indicates that the Al 3*p*- electrons play the same role as the Ru 4*d* electrons in the unusual magnetic order in CeRu$_2$Al$_{10}$. In other words, the hybridization of the Ce 4*f* electrons with the 4*d*-3*p* hybridized conduction band is essential in the gap formation and the unusual AFM order in CeRu$_2$Al$_{10}$.

Application of uniaxial pressure on CeT_2Al$_{10}$ has changed $T_{\rm N}$, $\chi(T)$, and spin-flop field B^* in an anisotropic way. It is found that application of $P//b$ strongly increases $T_{\rm N}$ with keeping both the magnitude and the temperature at the maximum of $\chi(T)$ unchanged. This finding indicates that the *c*-*f* hybridization is not the key parameter determining $T_{\rm N}$. Instead, the scaling of T_N by the *b*-axis parameter for the two compounds gives the evidence for the important role of the charge conduction along the *b* axis in the AFM order, that was previously suggested by the optical conduction measurements. Further, we have analyzed the pressure dependences of the spin-flop transition from $\mu_{AFM}//c$ to $\mu_{AFM}//b$ for $CeRu_2Al_{10}$. The spin-flop field B^* is found to be a linear function of $(1/d_2)\times(b/a)$, where d_2 is the distance between the Ce-Ce zigzag chains. This finding highlights the importance of the inter-chain interaction in the rhombic arrangement of zig-zag chains for stabilizing the unusual AFM state with μ_{AFM} along the *c* axis.

Acknowledgements

First, I would like to express my sincere gratitude to my supervisor Dr. K. Umeo for the providing me with this magnificent opportunity to embark on my doctoral study at the Hiroshima University of. His guidance helped me in all the time of research and writing of this thesis. I could not have imagined having a better advisor and mentor for my doctoral study. Particularly, my deepest gratitude is extended to Dr. K. Umeo for valuable suggestions, guidance, stimulating discussions, active interest, advice, throughout the period of this study. I am also sincerely grateful to the laboratory group leader, Prof. T. Takabatake. Without his persistent help, guidance, and encouragement, the thesis would not have materialized.

I would like to express my sincere gratitude to Prof. Y. Muro. During the course of my study at Toyama Prefectural University, I learned from him the importance and interests of studying novel compounds, in addition, how to grasp the essence of physics. Furthermore, I also wish to express great thanks to him for valuable advice and fruitful discussions even after I moved to Hiroshima University.

My sincere thanks goes to Profs. T. Fukuhara, T. Onimaru, K. Suekuni for valuable advices, discussions, and encouragement. This thesis could not be achieved without fruitful collaborations. Special thanks to Prof. T. Kuwai for his helping in the magnetization measurement using MPMS, and Prof. K. Motoya for his helping in the electron-probe microanalysis. The study with the collaborators, T. Takeuchi, Y. Yamada, and Dr. J. Kawabata was very pleasant because of their interesting and stimulative ideas. I appreciate their helpfulness on the large part of present study. Particularly, my sincere thanks also goes to T. Takeuchi who collaborated on the large part of the present study. Without his collaborations,

I could not get such the great results. I would like to acknowledge with thanks to those collaborators for their valuable contribution in the measurements and publications

I also acknowledge valuable discussions with Profs. H. Tanida, S. Kimura, Y. Kawamura, M. Sera and D. T. Adroja. Their experimental data led me deeper understanding of CeT_2Al$_{10}$ systems. A large part of the Introduction of this thesis is owed to their studies.

During the five years of my doctoral course, I have enjoyed my student life at Toyama Prefectural University and Hiroshima University, respectively. I would like to thank to M. Kamata, Drs. S. Kamikawa, Y. Hayashi, A. Fabiana, Profs. K. Wakiya, K. T. Matsumoto, and Y. Shimura for useful advices, discussions and encouragement. I also would like to thank to the members of Magnetism Laboratory, H. Tanaka, K. Uenishi, F. Kim, T. Yamaguchi, Y. Yamane, Y. Kosaka, D. Watanabe, Y. Okada, K. Hashikuni, G. B. Park, K. Miyoshi, T. Suenaga, M. Adachi, T. Ootaki, R. Yamada, S. Tsuda, K. Urashima, Y. Kusanose, S. Hara, R. Yamamoto, and Y. Arai. They create a harmonious and friendly atmosphere at the laboratory. Furthermore, my heartfelt appreciation goes to my friends, K. Takeda, T. Sasaki, T. Furuyama, J. Ejiri, C. Yang and J. Kawabata. I could spend interesting and valuable time with them not only inside but also outside the laboratory.

Last but not the least, I would like to thank my family for supporting me spiritually throughout writing this thesis and my life in general.

Bibliography

[1] J. Jensen and A. R. Mackintosh, *Rare Earth Magnetism Structures and Excitations* (Clarendon Press, Oxford, 1991).

[2] P. Misra, *Heavy-Fermion Systems* (Elsevier, Amsterdam, 2008).

[3] A.C. Hewson, *The Kondo Problem to Heavy Fermions* (Cambridge University Press, Cambridge, 1993).

[4] P. Coleman, *Introdution to Many-Body Physics*, (Cambridge University Press, Cambridge, 2015.)

[5] J. Kondo, Solid State Phys. **23**, 183 (1964).

[6] S. Doniach, Physica B **91**, 231 (1977).

[7] A. Sumiyama, Y. Oda, H. Nagano, Y. Onuki, and T. Komatsubara, J. Phys. Soc. Jpn. **55**, 1294 (1986).

[8] S. Hoshino and Y. Kuramoto, Phys. Rev. B **111**, 026401 (2013).

[9] H. Kitazawa, C. Schank, S. Thies, B. Seidel, C. Geibel, and F. Steglich, J. Phys. Soc. Jpn. **61**, 1461 (1992).

[10] H. Kitazawa, A. Matsushita, T. Matsumoto, and T. Suzuki, Physica B **199-200**, 28 (1994).

[11] J. Tang, A. Matsushita, H. Kitazawa, and T. Matsumoto, Physica B **217**, 97 (1996).

[12] W.A. Harrison, Phys. Rev. B **28**, 550 (1983).

[13] R. S. Kumar, A. L. Cornelius, and J. L. Sarrao, Phys. Rev. B **70**, 214526 (2004).

[14] O. M. Dix, A. G. Swartz, R. J. Zieve, J. Cooley, T. R. Sayles, and M. B. Maple, Phys. Rev. Lett. **102**, 197001 (2009).

[15] P. S. Riseborough, Adv. Phys. **49**, 257 (2000).

[16] K. Nakamura, Y. Kitaoka, K. Asayama, T. Takabatake, H. Tanaka, and H. Fujii, J. Phys. Soc. Jpn. **63**, 433 (1994).

[17] T. Takabatake, F. Teshima, H. Fujii, S. Nishigori, T. Suzuki, T. Fujita, Y. Yamaguchi, J. Sakurai, and D. Jaccard, Phys. Rev. B **41**, 9607 (1990).

[18] S. Nishigori, H. Goshima, T. Suzuki, T. Fujita, G. Nakamoto, H. Tanaka, T. Takabatake, and H. Fujii, J. Phys. Soc. Jpn. **65**, 2614 (1996).

[19] M. Kyogaku, Y. Kitaoka, H. Nakamura, K. Asayama, T. Takabatake, F. Teshima, and H. Fujii, J. Phys. Soc. Jpn. **59,** 1728 (1990).

[20] K. Izawa, T. Suzuki, M. Kitaoka, T. Fujita, T. Takabatake, G. Nakamoto, and H. Fujii, J. Phys. Soc. Jpn. **65**, 3119 (1996).

[21] M. F. Hundley, P. C. Canfield, J. D. Thompson, Z. Fisk, and J. M. Lawrence, Phys. Rev. B **42**, 6842 (1990).

[22] M. F. Hundley, P. C. Canfield, J. D. Thompson, and Z. Fisk, Phys. Rev. B **50**, 18142 (1994).

[23] I. Das and E. V. Sampathkumaran, Phys. Rev. B **46**, 4250 (1992).

[24] J. Hänel, H. Winkler, M. Ikeda, J. Larrea J, V. Martelli, A. Prokofiev, E. Bauer. and S. Paschen, J. Electron. Mater. **43**, 2440 (2014).

[25] H. Winkler, K. A. Lorenzer, A. Prokofiev, and S. Paschen, J. Phys. Conf. Ser. **391**, 012077 (2012).

[26] M. Kasaya, F. Iga, K. Negishi, S. Nakai, and K. Kasuya, J. Magn. Magn. Mater. **31-34**, 437 (1983).

[27] F. Iga, N. Shimizu, and T. Takabatake, J. Magn. Magn. Mater. **177-181**, 337 (1998).

[28] T. Takabatake, T. Yoshino, H. Tanaka. Y. Bando, H. Fujii, T. Fujita, H. Shita, and T. Suzuki, Physica B **206-207**, 804 (1995).

[29] S. Nishigori, H. Goshima, T. Suzuki, T. Fujita, G. Nakamoto, H. Tanaka, T. Takabatake, and H. Fujii, J. Phys. Soc. Jpn. **65**, 2614 (1996).

[30] A. Menth, E. Buehler, and T. H. Geballe, Phys. Rev. Lett. **22**, 295 (1969).

[31] J. C. Cooly, M. C. Aronson, Z. Fisk, and P. C. Canfield, Phys. Rev. Lett. **74**, 1629 (1995).

[32] M. Kasaya, K. Katoh, and K. Takegahara, Solid State Comm. **78**, 797 (1991).

[33] T. Sasakawa, T. Suemitsu, T. Takabatake, Y. Bando, K. Umeo, M. H. Jung, M. Sera, T. Suzuki, T. Fujita, M. Nakajima, K. Iwasa, M. Kohgi, Ch. Paul, St. Berger, and E. Bauer, Phys. Rev. B **66**, 041103(R) (2002).

[34] M. Matsumura, T. Sasakawa, T. Takabatake, S. Tsuji, H. Tou, and M. Sera, J. Phys. Soc. Jpn. **72**, 1030 (2003).

[35] E. D. Bauer, A. Slebarski, E. J. Freeman, C. Sirvent and M. B. Maple, J. Phys. Cond. Matt. **13**, 5183 (2001).

[36] T. Takabatake, F. Iga, T. Yoshino, Y. Echizen, K. Katoh, K. Kobayashi, M. Higa, N. Shimizu, Y. Bando, G. Nakamoto, H. Fujii, K. Izawa, T. Suzuki, T. Fujita, M. Sera, M. Hiroi, K. Maezawa, S. Mock, H. v. Lohneysen, A. Brückl, K. Neumaier, and K. Andres, J. Magn. Mag. Mater. **177-181**, 277 (1998).

[37] N. E. Bickers, D. L. Cox, J. W. Wilkins, Phys. Rev. Lett. **54**, 230 (1985).

[38] A. Brückl, K. Neumaier, Ch. Probst, K. Andres, S. J. Flaschin, A. Kratzer, G. M. Kalvius, and T. Takabatake, Physica B **240**, 199 (1997).

[39] S. Nishigori, H. Goshima, T. Suzuki, T. Fujita, G. Nakamoto, T. Takabatake, H. Fujii, and J. Sakurai, Physica B **186-188**, 406 (1997).

[40] T. Hiraoka, E. Kinoshita, T. Takabatake, H. Tanaka, and H. Fujii, Physica B **199 & 200**, 406 (1997).

[41] K. Umeo, T. Igaue, H. Chyono, Y. Echizen, T. Takabatake, M. Kosaka, and Y. Uwatoko, Phys. Rev. B **60**, R6957 (1999).

[42] T. Takabatake, Y. Echizen, T. Yoshino, K. Kobayashi, G. Nakamoto, H. Fujii, and M. Sera, Phys. Rev. B **59**, 13878 (1999).

[43] A. M. Strydom, Physica B **404**, 2981 (2009).

[44] V. M. T. Thiede, T. Ebel, and W. Jeitschko, J. Mater. Chem. **8**, 125 (1998).

[45] M. Sera, D. Tanaka, H. Tanida, C. Moriyoshi, M. Ogawa, Y. Kuroiwa, T. Nishioka, M. Matsumura, J. Kim, N. Tsujo, and M. Takata, J. Phys. Soc. Jpn **82**, 024603 (2013).

[46] D. T. Adroja, A. D. Hillier, Y. Muro, T. Takabatake, A. M. Strydom, A. Bhattacharyya, A. Daoud-Aladin, and J. W. Taylor, Phys. Scr. **88**, 068505 (2013).

[47] Y. Muro, K. Motoya, Y. Saiga, and T. Takabatake, J. Phys. Soc. Jpn. **78**, 083707 (2009).

[48] Y. Muro, K. Motoya, Y. Saiga, and T. Takabatake, J. Phys. Conf. Ser. **200**, 012136 (2009).

[49] T. Nishioka, Y. Kawamura, T. Takesawa, R. Kobayashi, H. Kato, M. Matsumura, K. Kodama, K. Matsubayashi, and Y. Uwatoko, J. Phys. Soc. Jpn. **78**, 123705 (2009).

[50] Y. Muro, K. Umeo, K. Nishimoto, R. Tamura, and T. Takabatake, Phys. Rev. B **81**, 214401 (2010).

[51] K. Hanzawa, J. Phys. Soc. Jpn. **79**, 043710 (2010).

[52] D. T. Adroja, A. D. Hillier, P. P. Deen, A. M. Strydom, Y. Muro, J. Kajino, W. A. Kockelmann, T. Takabatake, V. K. Anand, J. R. Stewart, and J. Taylor, Phys. Rev. B **82**, 104405 (2010).

[53] Y. Muro, K. Yutani, J. Kajino, T. Onimaru, and T. Takabatake, J. Kor. Phys. Soc. **63**, 508 (2013).

[54] D. D. Khalyavin, A. D. Hillier, D. T. Adroja, A. M. Strydom, P. Manuel, L. C. Chapon, P. Peratheepan, K. Knight, P. Deen, C. Ritter, Y. Muro, and T. Takabatake, Phys. Rev. B **82**, 100405(R) (2010).

[55] J. Kawabata, T. Takabatake, K. Umeo, and Y. Muro, Phys. Rev. B **89**, 094404 (2014).

[56] H. Miwa, Prog. Theor. Phys. **28**, 208 (1962).

[57] Y. Yamada, J. Kawabata, T. Onimaru, and T. Takabatake, J. Phys. Soc. Jpn. **84**, 084705 (2015).

[58] F. Strigari, M. Sunderman, Y. Muro, K. Yutani, T. Takabatake, K. D. Tsuei, Y. F. Liao, A. Tanaka, P. Thalmeier, M. W. Haverkort, L. H. Tjeng, and A. Severing, J. Electr. Spectr. Related Phenom. **199**, 56 (2015).

[59] Y. Zekko, Y. Yamamoto, H. Yamaoka, F. Tajima, T. Nishioka, F. Strigari, A. Severing, J. F. Lin, N. Hiraoka, H. Ishii, K. D. Tsuei, and J. Mizuki, Phys. Rev. B **89**, 125108 (2014).

[60] T. Kikuchi, S. Hoshino, and Y. Kuramoto, J. Phys. Soc. Jpn. **83**, 114706 (2014).

[61] T. Kikuchi, S. Hoshino, N. Shibata, and Y. Kuramoto, J. Phys. Soc. Jpn. **86**, 094602 (2017).

[62] H. Kato, R. Kobayashi, T. Takesaka, T. Nishioka, M. Matsumura, K. Kaneko, and N. Metoki, J. Phys. Soc. Jpn. **80**, 073701 (2011).

[63] P. Dean, Y. Muro, T. Takabatake, and P. D. Hatton, J. Phys. Soc. Jpn. **87**, 013706 (2018).

[64] Y. Muro, J. Kajino, T. Onimaru, and T. Takabatake, J. Phys. Soc. Jpn. **80**, SA021 (2011).

[65] G. Morrison, N. Haldolaarachchige, D. P Young, and J. Y Chan, J. Phys.: Condens.

Matter **24**, 356002 (2012).

[66] T. Mizushima, Y. Watanabe, J. Ejiri, T. Kuwai, and Y. Ishikawa, J. Phys. Conf. Ser. **592**, 012051 (2015).

[67] S. Kimura, T. Iizuka, H. Miyazaki, A. Irizawa, Y. Muro, and T. Takabatake, Phys. Rev. Lett. **106**, 056404 (2011).

[68] S. Kimura, T. Iizuka, H. Miyazaki, T. Hajiri, M. Matsunami, T. Mori, A. Irizawa, Y. Muro, J. Kajino, and T. Takabatake, Phys. Rev. B **84**, 165125 (2011).

[69] H. Tanida, D. Tanaka, M. Sera, C. Moriyoshi, Y. Kuroiwa, T. Takesaka, T. Nishioka, H. Kato, and M. Matsumura, J. Phys. Soc. Jpn. **79**, 083701 (2010).

[70] H. Tanida, D. Tanaka, Y. Nonaka, M. Sera, M. Matsumura, and T. Nishioka, Phys. Rev. B **84**, 233202 (2011).

[71] T. Nishioka, D. Hirai, Y. Kawamura, H. Kato, M. Matsumura, H. Tanida, M. Sera, K. Matsubayashi, Y. Uwatoko. J. Phys. Conf. Ser. **273**, 012046 (2011).

[72] D. T. Adroja, A. D. Hillier, Y. Muro, J. Kajino, T. Takabatake, P. Peratheepan, A. M. Strydom, P. P. Deen, F. Demmel, J. R. Stewart, J. W. Taylor, R. I. Smith, S. Ramos, and M. A. Adams. Phys. Rev. B **87**, 224415 (2013).

[73] K. Hayashi, Y. Muro, T. Fukuhara, T. Kuwai, J. Kawabara, T. Takabatake, M. Hagihala, and K. Motoya, Phys. Proc. **75**, 121 (2015).

[74] A. Kondo, K. Kindo, K. Kunimori, H. Nohara, H. Tanida, M. Sera, R. Kobayashi, T. Nishioka, and M. Matsumura, J. Phys. Soc. Jpn. **82**, 054709 (2013).

[75] R. Kobayashi, Y. Ogane, D. Hirai, T. Nishioka, M. Matsumura, Y. Kawamura, K. Matsubayashi, Y. Uwatoko, H. Tanida, and M. Sera, J. Phys. Soc. Jpn. **82**, 093702 (2013).

[76] J. Kawabata, K. Yutani, K. Umeo, T. Takabatake, and Y. Muro, Phys. Rev. B **89**, 094404 (2014).

[77] R. Kobayashi, K. Kaneko, K. Saito, J. M. Mignot, G. André, J. Robert, S. Wakimoto, M. Matsuda, S. Chi, Y. Haga, T. D. Matsuda, E. Yamamoto, T. Nishioka, M. Matsumura, H. Tanida, and M. Sera, J. Phys. Soc. Jpn. **83**, 104707 (2014).

[78] D. D. Khalyavin, D. T. Adroja, P. Manuel, J. Kawabata, K. Umeo, T. Takabatake, and A. M. Strydom, Phys. Rev. B **88**, 060403 (2013).

[79] Y. Muro, K. Hida, T. Fukuhara, J. Kawabata, K. Yutani, and T. Takabatake, JPS Conf. Proc. **3**, 012017 (2014).

[80] H. Tanida, H. Nohara, M. Sera, T. Nishioka, M. Matsumura, and R. Kobayashi, Phys. Rev. B. **90**, 165124 (2014).

[81] H. Tanida, Y. Nonaka, D. Tanaka, M. Sera, T. Nishioka, and M. Matsumura, Phys. Rev. B. **86**, 085144 (2012).

[82] K. Umeo, T. Ohsuka, Y. Muro, J. Kajino, and T. Takabatake, J. Phys. Soc. Jpn. **80**, 064709

(2011).

[83] H. Tanida, K. Kitagawa, N. Tateiwa, M. Sera, and T. Nishioka, Phys. Rev. B **96**, 235131 (2017).

[84] M. E. Fisher, Philos. Mag. **7,** 1731 (1962).

[85] Y. Kawamura, T. Kawaai, T. Nakayama, J. Hayashi, K. Takeda, C. Sekine, T. Nishioka, and Y. Ohishi, J. Phys. Soc. Jpn. **85**, 044601 (2016).

[86] H. Tanida, Y. Nonaka, D. Tanaka, M. Sera, T. Nishioka, and M. Matsumura, Phys. Rev. B **88**, 045135 (2013).

[87] D. T. Adroja, A. D. Hillier, C. Ritter, A. Bhattacharyya, A. M. Strydom, P. Peratheepan, M. M. Koza, J. Kawabata, Y. Yamada, Y. Okada, B. Fåk, Y. Muro, T. Takabatake, and J. W. Taylor, Phys. Rev. B **92**, 094425 (2015).

[88] F. Izumi and T. Ikeda, Mater. Sci. Forum, **321-324**, 198 (2000).

[89] S. K. Dhar and S. M. Pattalwar, J. Magn. Magn. Mater. **152**, 22 (1996).

[90] H. Flandorfer, D. Kaczorowski, J. Gröbner, P. Rogl, R. Wouters, C. Godart, and A. Kostikas, J. Solid State Chem. **137**, 191 (1998).

[91] T. F. Smith, C. W. Chu, and M. B. Maple, Cyrogenics **9**, 53 (1969).

[92] H. Kubo, K. Umeo, K. Katoh, A. Ochiai, and T. Takabatake, J. Phys. Soc. Jpn. **79**, 064715, (2010).

[93] K. Umeo, Rev. Sci. Instrum. **87**, 063901 (2016).

[94] J. D. Jennings and C. A. Swenson, Phys Rev. **112**, 31 (1958).

[95] M. H. Jung, S. H. Park, H. C. Kim, and Y. S. Kwon, J. Magn. Magn. Mater. **272-276**, E431 (2004).

[96] D. Gignoux and J. C. Gomez-Sal, Phys. Rev. B **30**, 3967 (1984).

[97] M. Samel-Czekala, E. Talik, M. Pasturel, and R. Troc, J. Alloys. Compds. **554**, 438 (2013).

公表論文

(1) Anisotropic dependence of the magnetic transition on uniaxial pressure in the Kondo semiconductors CeT_2Al$_{10}$ (T = Ru and Os)
K. Hayashi, K. Umeo, T. Takeuchi, J. Kawabata, Y. Muro, and T. Takabatake, Physical Review B **96**, 245130 /1-6 (2017).

(2) Uniaxial pressure effects on the unusual antifettomagnetic transition in the Kondo semiconductor CeOs$_2$Al$_{10}$
K. Hayashi, K. Umeo, Y. Yamada, J. Kawabata, Y. Muro, and T. Takabatake, Journal of Physics: Conference Series **607**, 022002 /1-6 (2017).

(3) Effect of Si substitution on the antiferromagnetic ordering in the Kondo semiconductor CeRu$_2$Al$_{10}$
K. Hayashi, Y. Muro, T. Fukuhara, J. Kawabata, T. Kuwai, and T. Takabatake,
Journal of the Physical Society of Japan **85**, 034714 /1-4 (2016).

(4) Anisotropic chemical pressure effect on the antiferromagnetic Kondo semiconductor Ce(Ru$_{1-x}$Fe$_x$)$_2$Al$_{10}$
K. Hayashi, Y. Muro, T. Fukuhara, T. Kuwai, J. Kawabara, T. Takabatake, M. Hagihala, and K. Motoya,
Physics Procedia **75**, 121-126 (2015).